

Pressure Anisotropy and Microinstability
of RF-Heated Plasmas in a Tandem Mirror

March 1994

Ryota Katsumata

①

Pressure Anisotropy and Microinstability of RF-Heated Plasmas in a Tandem Mirror

Abstract

Ryota Katsumata

*Institute of Applied Physics, University of Tsukuba
Tsukuba, Ibaraki 305, JAPAN*

March 1994

Abstract

The pressure anisotropy is quantitatively estimated in RF-heated plasmas which are magnetically confined in tandem mirror GAMMA 10. The pressure anisotropy is defined as ratio of pressures perpendicular to parallel to the magnetic field line (P_{\perp}/P_{\parallel}), which indicates a degree of distortion of a distribution function in a velocity space. The pressure profile of the anisotropic plasmas ($P_{\perp}/P_{\parallel} \gg 1$) is peaked at the midplane of the magnetic mirror in the direction of the magnetic field line. The pressure of the isotropic plasmas ($P_{\perp}/P_{\parallel} \sim 1$) is constant along the magnetic field line. The pressure profile is connected with P_{\perp}/P_{\parallel} in term of magnetohydrodynamic (MHD) equilibrium.

Some simple methods are developed for estimating the pressure anisotropy and compared with each others. The first is to use an array of diamagnetic loops which is arranged along the magnetic field line for measuring the axial pressure profile. The second is to use a small Faraday cup which can directly obtain a pitch angle distribution of ions at peripheral region of the plasma. The third is to use a secondary electron detector (SED) array which detect neutral particles emitted from a plasma through the charge exchange collisions. The neutral particle carries away the same momentum as an ion. Then, the

pitch angle distribution of the ions is deduced from that of the neutral particles.

Effects of the pressure anisotropy on microinstability are studied. An Alfvén Ion Cyclotron (AIC) mode is one of microinstabilities in the range of an ion cyclotron frequency, which is driven by plasma beta (ratio of plasma pressure to magnetic pressure) and the pressure anisotropy. Magnetic fluctuations which are dependent on beta and the pressure anisotropy are identified as the AIC mode. Spatial structure of the AIC mode is clarified in the axial, radial and azimuthal direction. The AIC mode propagates azimuthally in the left-handed direction with respect to the magnetic field line and has an azimuthal wave length comparable with a circumference of the plasma column. The AIC mode has a left-handed polarization at the core of the plasma column and the right-handed polarization on the periphery. These characteristics of the fluctuations agree with a theoretical prediction on the AIC mode. Measurements of axial wave numbers in the axial direction indicate that the AIC mode has a propagating region and a standing wave region. The axial extension of the standing wave region is found to depend on an AIC driving term defined by $\beta_{\perp}(P_{\perp}/P_{\parallel})^2$. Here, β_{\perp} is a perpendicular beta value along the magnetic field line. A new theoretical model on a one dimensional axially-bounded AIC mode is proposed. Fine structure of the frequency spectra of the AIC mode is compared with the dispersion relation which is derived from the newly-proposed eigenvalue equations. This model explains well the measured discrete spectra which depend on both β_{\perp} and the pressure anisotropy.

Relaxation of the pressure anisotropy associated with an onset of the AIC mode is

experimentally observed by using the diamagnetic loop array, the small Faraday cup and the SED array. The pressure anisotropy relaxation corresponds to an enhancement of the velocity space diffusion caused by the AIC mode.

Effects of the pressure anisotropy on a macroinstability are also studied. Flute-interchange mode is one of the macroinstabilities which are driven by the pressure weighted on bad curvature region of a magnetic field line. Stability limit determined by the flute-interchange mode is typically described by the beta value ratio between the central and anchor cells. This critical beta ratio has a strong dependence on the pressure anisotropy of the central cell. The stronger pressure anisotropy leads to the higher critical beta ratio.

Contents

Abstract	i
1 Introduction	1
2 Experimental Setup	8
2.1 GAMMA 10 Tandem Mirror	8
2.2 Heating and Gas Fueling System	10
2.3 Diagnostics	12
2.3.1 Measurements of Pressure Anisotropy	13
2.3.2 Fluctuation Measurements	23
3 Quantitative Estimation of Pressure Anisotropy	28
3.1 Pressure Profile Model	28
3.2 Experimental Results and Discussion	32
4 Alfvén Ion Cyclotron Instability	36
4.1 Physical Picture of AIC Mode	36

4.2	Observation and Identification of Fluctuations	39
4.3	Spatial Structure and Excitation Condition	45
4.3.1	New Theory for AIC Eigenmodes	45
4.3.2	Experimental Results and Discussion	50
4.4	Pressure Anisotropy Relaxation due to AIC Instability	52
5	Pressure Anisotropy Effects on Micro- and Macroscopic Stabilities	55
5.1	Suppression of AIC mode by Control of Pressure Anisotropy	55
5.2	Pressure Anisotropy Effect on Flute-Interchange Mode	57
5.2.1	Stability Theory of Flute-Interchange Mode	57
5.2.2	Experimental Results and Discussion	60
6	Conclusion	64
	Acknowledgements	67
A	Other Heating Systems and Diagnostics	69
B	Dispersion Relation of AIC mode	72
C	Absolute and Convective Instabilities	77
	References	82
	Figure Captions	87

Chapter 1

Introduction

It is in the decade from the early 1960s to early 1970s that microinstabilities in mirror machines are of crucial subject, because it is considered that the plasma confinement was degraded owing to the instabilities¹⁾. The microinstabilities in the mirror system is driven by a free energy owing to loss-cone character of the ion distribution function, which has a negative gradient and an anisotropy in the velocity space. Many microinstabilities are studied experimental by and theoretical by. Their physical characteristics are to be obvious and stabilizing methods are developed. The suppression of the microinstability is attained by filling the loss-cone and reducing the free energy due to the loss-cone.

The tandem mirror concept is one of the ideas which reforms the distribution function to be a stable one. In this concept the confinement system basically consists of three linked mirror cells. A large volume mirror cell is centered and two small mirror cells are placed at both ends of the central cell where a positive potential is produced and suppress

end losses along the magnetic field line. With the potential formation, the loss cone of the ion distribution function of the central-cell plasma is filled out.

Recently, in order to attain plasma parameter in the fusion reactor regime, additional plasma heating is attempted by various methods, such as high energy neutral beam injection and high power radio frequency (RF) heating. The principle of the RF heating is to convert the oscillating-field energy to a thermal energy of the plasma particles. The energy conversion from the RF wave to the plasmas takes place through collisional dissipation, such as resistivity and viscosity, as well as collisionless dissipation such as cyclotron damping, transit time magnetic pumping and Landau damping. Particles which are accelerated by the RF field yield a high energy tail in the distribution function especially in the case of the collisionless dissipation. This high energy tail deforms the distribution function into an anisotropic one. The anisotropy of the ion distribution in the velocity space is determined by the balance between production and loss of the high energy components in the velocity space and the energy relaxation from the energetic particles to the thermal component.

In the GAMMA 10 tandem mirror^{2,3)} high energy plasmas with hot ions are produced by using radio-frequency (RF) heating in the range of ion cyclotron frequency. Energy containment of the ions in the present experiments is dominated by charge-exchange loss and/or electron drag. Typical time scale of the ion-ion coulomb collision is much longer than those of these energy loss processes, and then the energy of the hot ions can not be sufficiently converted to the thermal energy. In a simulation study by using a Fokker-

Planck code, an anisotropic distribution function is demonstrated for the plasma parameters obtained in the experiments⁴⁾. Sudden saturation phenomena of the energy which is stored in the central cell has been observed in the strong heated plasmas. This saturation is not explained by the electron drag and charge-exchange loss. It is expected that the instability related to the anisotropy plays an important role in this saturation mechanism. Hence, the microinstabilities which are driven by the free energy of anisotropic, high-beta plasmas deserve to be studied with a special attention.

Alfvén ion cyclotron mode (AIC) is one of a electromagnetic instabilities which is driven by plasma pressure and pressure anisotropy. Shear Alfvén wave couples with free energy derived from the relaxation of an anisotropic population of ion energy state and becomes unstable. Here, the anisotropic population means a distribution function which has the perpendicular pressure greater than the parallel pressure.

Study of the AIC mode is advanced by many theorists^{5,6)} and experimentalists⁷⁾ from the various standpoints. In comparison with the theoretical development of the AIC mode, the experimental study in a laboratory is less advanced because of difficulties in producing a highly anisotropic plasma and then rarely observed except for a few examples as follows. In the foreshock region of the earth's bow shock, both of incident and reflected ion beams are observed. A heating source is required for the existence of the ion beams. Wave heating due to the AIC mode is simulated in the hybrid-particle code and discussed on the possibility⁸⁾. Deterioration of the plasma confinement particular in the mirror devices because fluctuating wave field associated with the AIC mode induces the diffusion

in the velocity space. Ions are scattered to the loss cone in a time scale shorter than the coulomb collision time⁹⁾. It is of crucial issue to study the AIC mode in the tandem mirror.

In TMX (Tandem Mirror Experiment) device, the AIC modes are observed in the end-cell plasma which is produced by perpendicularly-injected high energy neutral beam in order to form a plugging potential formation and the plasma confinement is degraded¹⁰⁾. It is reported that the AIC modes have small azimuthal mode number and frequencies as low as 12 % below the minimum ion cyclotron frequency in the end cell. The polarization is in the direction of the ion gyration, and the azimuthal propagation is in either the electron or the ion diamagnetic direction. Stabilization of the AIC mode is achieved by reducing the anisotropy which is controllable by adjusting the injection angle of the neutral beam. The physics of the shear Alfvén wave generated by the AIC instability is also studied by observation. The mode conversion from shear Alfvén wave to compressional Alfvén wave is theoretically predicted at the transition region of the magnetic field between the central cell and end cell¹¹⁾.

In the Tara tandem mirror, the AIC modes which are excited in the ICRF-heated and central-cell plasma are studied¹²⁾. Stability threshold of the AIC mode is discussed and is within a factor of 2 of the theoretical value. The stability threshold of the AIC mode is theoretically predicted as the boundary between absolute and convective instabilities.

The unstable region is approximately represented as follows :

$$\beta_{\perp} \left(\frac{P_{\perp}}{P_{\parallel}} \right)^2 \geq 3.5. \quad 1.1$$

In the Tara experiment the AIC modes have frequencies of $\omega/\Omega_{ci} = 0.8 - 0.9$ and have the parallel wave number of $k_{\parallel} = 2 - 6 \text{ m}^{-1}$. Here, Ω_{ci} is the cyclotron frequency corresponding to the minimum magnetic field strength of the central cell.

In the central cell of the GAMMA 10 tandem mirror, the peak ion temperature of 5 keV is attained with the pressure anisotropy P_{\perp}/P_{\parallel} is above 10. Magnetic fluctuations is observed depending on the beta value β_{\perp} and the pressure anisotropy¹³⁾. From detailed measurements, we have identified the mode as an AIC mode. In order to specify the mode structure, we need spatial measurements of these fluctuations¹⁴⁾. In this paper, we mainly report the identification of the fluctuations and specification of the mode structure in an inhomogeneous and bounded plasma column. Detailed measurements of the spatial structure reveal that the AIC mode is excited as an eigenmode constrained by an axial boundary condition. The AIC-mode stability threshold in GAMMA 10 is experimentally obtained and represented approximately as follows :

$$\beta_{\perp} \left(\frac{P_{\perp}}{P_{\parallel}} \right)^2 \geq 0.3. \quad 1.2$$

In the region of $\beta_{\perp}(P_{\perp}/P_{\parallel})^2 < 3.5$, the conventional theory for an infinite and uniform

plasma predicts that the AIC mode will be released out of the plasma region before growing up to a observable fluctuation level. The unstable parameter regime should be modified by the finite-length effect in the real experiments. A new model which includes the effect of the axial boundary condition is developed in this paper. Theoretically it is usually considered that the finite-length effect stabilizes the AIC mode¹⁵⁾. In the present new theory, the AIC mode is destabilized by wave reflection which is caused at an axial boundary layer. Recently, it is reported that the AIC mode is observed by a using nonperturbing reflectometry system in the GAMMA 10 experiments^{16,17)}.

For another example on the interaction between the anisotropic distribution and shear Alfvén waves, toroidal Alfvén eigenmodes (TAE) are observed in large-tokamak current-drive experiments by use of deuterium neutral-beam injection^{18,19)}. Because the velocity of the high energy neutral beam is comparable with the Alfvén velocity, the neutral beam interacts strongly with the shear Alfvén waves which are driven unstable. The resulting fluctuations cause diffusion of fast particles produced by the neutral beam injection and reduction of the current-drive efficiency. In this case, the anisotropic population is composed by a distribution function with the parallel pressure greater than the perpendicular pressure. In the fusion reactor regime, it is expected that the 3.5 MeV alpha particles from D-T reaction are born and from the high energy anisotropic population. It is possible that the highly energetic alpha particles drive the TAE mode and degrade the confinement. From the sense of the physics of the shear Alfvén wave, the AIC modes have some characteristics similar to the TAE modes on wave propagation, excitation condition and

effects on the plasma parameters. Thereby, the study of the interaction between the shear Alfvén wave and the anisotropic distribution is a common problem in various magnetic confinement devices.

The plan of this paper is as follows : experimental setup is described in chapter 2, the quantitative analyses on the pressure anisotropy by using diamagnetic loops in chapter 3, the identification, spatial structures and the new model of the AIC mode and an effect on the plasma parameter due to the AIC mode which is experimentally observed in chapter 4, possibility of controlling the pressure anisotropy by using two-frequency RF heating and suppression of the AIC mode, for another example on the stability which is related to the pressure anisotropy, stability study on flute-interchange mode in chapter 5, and finally conclusion in chapter 6.

Chapter 2

Experimental Setup

2.1 GAMMA 10 Tandem Mirror

GAMMA 10 is an axisymmetrized tandem mirror with a thermal barrier which is schematically drawn in Fig.2.1. The tandem mirror is designed to improve the plasma confinement by the combination of a magnetic mirror and positive electrostatic potential hill's which is produced at both ends of the mirror for reducing axial endloss ions. The thermal barrier helps an efficient formation of the plug potential for the ion confinement. GAMMA 10 consists of five mirror cells, which are a central cell, minimum-B anchor cells and end plug/barrier cells at both ends. Total length of GAMMA 10 is 27 m and total volume of stainless-steel vessel is 150 m^3 . The length of the central cell between the mirror throats is 5.8 m and the diameter of the vacuum vessel is 1 m. Magnetic field strength at the midplane of the central cell is 0.405 T in a standard mode of the operation and the mirror

ratio is 5. A limiter of which diameter is 0.36 m is set near the midplane. The anchor cells are located at the both ends of the central cell and consists of a minimum-B mirror field which is produced by a baseball seam coil. The anchor cell is named after the role that the anchor plasmas fastens the central plasma which is, otherwise MHD unstable. The magnetic field strength is 0.610 T at the midplane of the anchor cell and the mirror ratio is 3. The plug/barrier cells are located at the both ends of GAMMA 10, where the thermal barrier and plug potential are produced. The base pressure is less than 5×10^{-8} torr; it is maintained by turbomolecular pumps (three pumps with $2.5 \text{ m}^3\text{s}^{-1}$ and three pumps with $1.5 \text{ m}^3\text{s}^{-1}$), cryopumps (two pumps with $10 \text{ m}^3\text{s}^{-1}$ and $18 \text{ m}^3\text{s}^{-1}$ in the central cell, two pumps with $18 \text{ m}^3\text{s}^{-1}$ in the plug/barrier cells and two pumps with $18 \text{ m}^3\text{s}^{-1}$ in the end mirror tanks) and cryopanel (two panels for the anchor cell with $400 \text{ m}^3\text{s}^{-1}$ and two panels for the end-mirror tanks with $900 \text{ m}^3\text{s}^{-1}$). At each end of GAMMA 10, radially and azimuthally-segmented end plates are installed and are grounded with resistors of $1 \text{ M}\Omega$ to ground. Typical plasma parameters are as follows : the density $n = 3.0 \times 10^{18} \text{ m}^{-3}$ on axis, the averaged ion temperature $T_{i\perp} = 3.6 \text{ keV}$, the electron temperature $T_e = 100 \text{ eV}$ and the averaged plasma beta perpendicular to the magnetic field line $\beta_{\perp} = 2.3 \%$. Because the electron temperature is much lower than the ion temperature and is expected to be uniform along the field line, the ion diamagnetic current is dominated by the ion pressure.

2.2 Heating and Gas Fueling System

ICRF System

Figure 2.2 shows schematics of power supplies, antennas and transmitter lines for the ICRF heating. Two kinds of antennas are installed near the mirror throats at the central cell. One is so-called NAGOYA TYPE-III antennas which are installed at the locations of $z = \pm 2.2$ m, where $R = 1.6$ ^{20,21,22}. The other is conventional double-half-turn antennas which are installed at the location of $z = \pm 1.7$ m, where $R = 1.1$. These antennas are driven by two different frequencies of 9.6 MHz and 6.2 MHz. The frequency of 9.6 MHz which corresponds to the ion cyclotron frequency near the midplane of the anchor cell is required for producing and sustaining plasmas. Two oscillator systems are constructed, which are named as RF1 and RF2 systems. The performance of each system is as follows : the frequency ranges from 6.2 MHz to 30 MHz for RF1 system and from 4.6 MHz to 9.9 MHz for RF2 system, the maximum output power is 1 MW and the maximum pulse duration of 100 ms for two system.

Each RF system has two final amplifiers in order to drive each antenna independently. RF1 and RF2 have almost same composition. The RF source signal is generated by a signal generator (SG) MG439B (ANRITSU Elec. Corp.) and divided into two branches. The outputs of the wide-band amplifier are connected to intermediate power amplifiers (IPA) and finally connected to the power amplifiers (PA). One is connected to a wide-band amplifier and another is also connected to the wide-band amplifier via phase shifter.

Between antennas and power amplifiers, there are matching boxes which have roles of tuning and impedance matching. One branch of RF1 system has an additional exciter amplifier (EX) which is used for getting a sufficient drive power for IPA2. Phase shifters installed between the signal generators and wide band amplifiers controls the phase difference between two outputs. The RF current of RF2 system is divided into two lines in the matching box and connected to each half-turn antenna with same phase. The RF current of RF1 system is divided into two lines and connected two matching boxes. Each matching box is connected to the set of top and bottom antenna elements or to the set of north and south antenna elements of NAGOYA TYPE-III antenna. The top and bottom elements or north and south elements are driven out of phase. The phase between the set of top/bottom and north/south is controlled by changing the cable length between the matching box and divider. A compressional Alfvén wave which is launched from the NAGOYA TYPE-III antenna propagates through a flux tube with an elliptical cross section between the anchor and central cells and converted to a shear Alfvén wave²³⁾. The converted share Alfvén wave is damped at the ion cyclotron resonance layer in the anchor cell. Therefore, a high-beta plasma is maintained in the anchor cell and provides on the MHD stability of the GAMMA 10 tandem mirror²⁴⁾. The frequency of 6.2 MHz which corresponds to the ion cyclotron frequency at the midplane of the central cell is required for the central-cell ion heating.

The plasma is started up by injecting a short pulse (1ms) gun-produced plasma from each end and is sustained by applying only ICRF power in combination with a hydrogen

gas puffing in the central cell. The radiated power of ICRF antennas is typically 200 kW in total with the duration of 50 ms.

Gas Puffing System

Four kinds of piezoelectric gas puffed are equipped in the GAMMA 10 as shown in Fig.2.3. Some of these are combined to start up (#1b and #2b) and sustain a plasma (#1a,#2a,#3a and #4a) in a pre-programmed manner and the others are auxiliary used for a special physical purpose such as a short-pulse additional gas puffing for studying plasma responses by increasing of the charge exchange loss and of wall reflux (#3b and #4b). In the transient phase of the plasma startup, a puffer (#1b and #2b) with a fast response of 1-2 ms is combined with a puffer (#1a and #2a and/or #3a and #4a) with a slow response and a good axisymmetry for gas injection. In the quasi-steady phase, only the latter puffer is used at a reduced gas flow rate. Gas flow rate of each puffer is controlled by the reservoir pressure because of the better reproducibility compared with the voltage control of the flow rate.

2.3 Diagnostics

Figure 2.4 shows the axial profile of the magnetic field strength in the central and the anchor cell and locations where the diagnostic and the heating systems are arranged.

2.3.1 Measurements of Pressure Anisotropy

Diamagnetic Loop

Three diamagnetic loops are installed at the locations of $z=-0.33$ m, $z=-1.5$ m and $z=1.95$ m in order from the central-cell midplane. Mirror ratios at the location of the each diamagnetic loop are 1.008, 1.077 and 1.264, respectively. Each diamagnetic loop is named as the midplane loop W_1 , the second loop W_2 and the third loop W_3 . The inner diameter of the diamagnetic loop is large enough compared with the limiter diameter of 0.36 m. Two diamagnetic loops are installed at the midplane in each anchor cell, which are named as W_{EA} and W_{WA} . The sum of the W_{EA} and W_{WA} are represented as W_A . The inner diameters of W_1 , W_2 , W_3 , W_{EA} and W_{WA} are 0.55 m, 0.55 m, 0.40 m, 0.50 m and 0.50 m. From the diamagnetism measured by loops installed at the locations of $z=\pm 1.5$ m, it is confirmed that the axial pressure profile is symmetric with respect to the central-cell midplane.

A simplified method employed to determine plasma pressure from the observed diamagnetic loop signals is described as follows : The signal-to-noise ratio is improved by using a novel cancellation technique with a concentric pair of diamagnetic loops. The plasma pressure equilibrium is described by the ideal MHD equation.

$$\rho \frac{\partial \mathbf{v}}{\partial t} = \mathbf{j} \times \mathbf{B} - \nabla P, \quad 2.1$$

where

$$\begin{aligned}\rho &= n_i m_i + n_e m_e \sim n(m_i + m_e) \\ \mathbf{v} &= \frac{n_i m_i \mathbf{v}_i + n_e m_e \mathbf{v}_e}{\rho} \\ \mathbf{j} &= e(n_i \mathbf{v}_i - n_e \mathbf{v}_e) = en(\mathbf{v}_i - \mathbf{v}_e).\end{aligned}$$

P is plasma pressure, n_i, n_e and n are ion, electron and plasma densities, respectively, $\mathbf{v}_i, \mathbf{v}_e$ are velocity vector of ions and electrons, respectively. In a steady state ($\partial/\partial t = 0$)

$$\nabla P = \mathbf{j} \times \mathbf{B}. \quad 2.2$$

From the Maxwell's equation in a steady state $\nabla \times \mathbf{B} = \mu_0 \mathbf{j}$, where μ_0 is the magnetic permeability of vacuum, Eq.2.2 is represented as follows :

$$\nabla P = \left(\frac{1}{\mu_0} \nabla \times \mathbf{B} \right) \times \mathbf{B}. \quad 2.3$$

The right-hand side in Eq.2.3 tells that

$$\left(\frac{1}{\mu_0} \nabla \times \mathbf{B} \right) \times \mathbf{B} = \frac{1}{\mu_0} ((-\nabla(\mathbf{B} \cdot \mathbf{B}) + 2(\mathbf{B} \cdot \nabla) \mathbf{B} + \mathbf{B} \times (\nabla \times \mathbf{B})), \quad 2.4$$

where

$$(\nabla \times \mathbf{B}) \times \mathbf{B} = (\mathbf{B} \cdot \nabla) \mathbf{B} - \frac{\nabla B^2}{2}. \quad 2.5$$

Substituting Eq.2.5 in Eq.2.4,

$$\nabla \left(P + \frac{B^2}{2\mu_0} \right) = \frac{1}{\mu_0} (\mathbf{B} \cdot \nabla) \mathbf{B}. \quad 2.6$$

Because the right-hand side of Eq.2.6 is neglected in a nearly uniform magnetic field, the pressure equilibrium is represented as follows :

$$P + \frac{B^2}{2\mu_0} = \text{constant}. \quad 2.7$$

Then, the pressure in a straight cylindrical plasma is obtained as

$$P = \frac{1}{2\mu_0} (B_0^2 - B^2), \quad 2.8$$

where B_0 and B are the magnetic field strength outside and inside of the plasma, respectively. If the plasma pressure is small, the plasma pressure in a uniform magnetic field is represented as follows :

$$P = \frac{B_0 \cdot \Delta B}{\mu_0}, \quad 2.9$$

where B_0 is considered to be uniform in the radial direction at least within the outer coil radius as in the GAMMA 10 central cell. ΔB is defined as $\Delta B = B_0 - B$. Magnetic flux

Φ_1 and Φ_2 through the inner and outer coils are simply written as follows :

$$\begin{aligned}\Phi_1 &= \pi r_p^2 B + \pi(r_1^2 - r_p^2)B_0 \\ \Phi_2 &= \pi r_p^2 B + \pi(r_2^2 - r_p^2)B_0,\end{aligned}\tag{2.10}$$

where r_p, r_1 and r_2 are the plasma radius, the inner and outer coil radii, respectively. The electromotive force generated on the coils (V_1 and V_2) is

$$\begin{aligned}V_1 &= -N \frac{d\Phi_1}{dt} = N\pi r_p^2 \frac{d}{dt}(\Delta B) - N\pi r_1^2 \frac{d}{dt}(B_0) \\ V_2 &= -N \frac{d\Phi_2}{dt} = N\pi r_p^2 \frac{d}{dt}(\Delta B) - N\pi r_2^2 \frac{d}{dt}(B_0),\end{aligned}\tag{2.11}$$

where N is the number of turns of each coil. In Eq.2.11, the first term is the diamagnetic signal and the second term is noise caused by the field ripples. The concentric diamagnetic loop is used to cancel the ripple as follows :

$$V_0 \equiv N\pi r_p^2 \frac{d}{dt}(\Delta B) = V_1 - \frac{r_1^2}{r_2^2 - r_1^2} (V_2 - V_1),\tag{2.12}$$

where V_0 is the ripple-canceled loop signal. From the time-integration of Eq.2.12 the diamagnetic loop signal W (in unit Wb) is obtained as follows :

$$W = \pi r_p^2 \Delta B = \frac{1}{N} \int V_0 dt.\tag{2.13}$$

The substitution of Eq.2.13 into Eq.2.9 yield

$$P = \frac{B_0}{N\pi\mu_0 r_p^2} \int V_0 dt = \frac{B_0}{\mu_0\pi r_p^2} W. \quad 2.14$$

In this section, the simplified relation between the plasma pressure and the diamagnetic loop signal is represented. The more realistic calculation including the effects of finite length of plasmas is discussed in chapter 3.

Small Faraday Cup

A small Faraday cup is a multi-grid-type electrostatic energy analyzer, which is installed at the midplane of the central cell and can rotate around the x-axis of GAMMA 10²⁵). A schematic of the small Faraday cup is shown in Fig.2.5. The small Faraday cup is used for measurements of the pitch-angle distribution of ions. The first grid is floated for minimizing a disturbance to the plasma. The second and third grids are negatively biased to retard electrons. The fourth and fifth grids are used for suppressing secondary electrons which are emitted from the collector and the third grid. By tracing the ion orbits in the energy range from 1 eV to 5 keV by use of a computer, ion energy dependence of the detector efficiency is estimated for the angle θ , where θ is defined as the angle between the axis of the small Faraday cup and the magnetic field line. No energy dependence for a fixed angle θ is confirmed by the computer simulation above 100 eV. When the magnetic field strength is 4 T, the minimum detectable energy is 100 eV. By tracing the

ion orbit with the energy from 1 eV to 5 keV with pitch angles different from θ , the pitch angle resolution of the Faraday cup can be evaluated. Figure 2.6a shows the pitch angle dependence with the Faraday cup set at $\theta = 70^\circ$ under the magnetic field strength of 0.4 T. The pitch angle resolution is determined to be about $\pm 5^\circ$ from the FWHM of the pitch angle profile. The detector efficiency depends on the pitch angle. Figure 2.6b shows efficiencies normalized by the efficiency for the case of $\theta = 27^\circ$, which corresponds to the loss cone angle in the present experiments. The signals detected by the small Faraday cup are integrated flux of ions which have their pitch angles between $\theta + \Delta\theta/2$ and $\theta - \Delta\theta/2$. The detected flux Γ_θ is represented as follows :

$$\Gamma_\theta \propto \int_{v_{min}}^{\infty} \int_{\theta - \Delta\theta/2}^{\theta + \Delta\theta/2} v_\theta f dv_\theta v_\theta d\theta, \quad 2.15$$

where v_{min} is the minimum detectable velocity, f is the velocity distribution function and v_θ is the velocity of ions which have the pitch angle of θ . By changing θ , the pitch angle distribution of the total ion current can be measured under a fixed plasma operation condition. In the case of strongly RF-heated plasmas the distribution function of ions can be approximately described by a bi-Maxwell distribution. The distribution function is written as follows :

$$f = n^{3/2} k^{3/2} \left(\frac{m}{2\pi P_\perp} \right) \left(\frac{m}{2\pi P_\parallel} \right)^{1/2} \exp \left[-\frac{mv_\theta^2}{2} \left(\frac{nk \sin^2 \theta}{P_\perp} + \frac{nk \cos^2 \theta}{P_\parallel} \right) \right] \quad 2.16$$

By using Eqs.2.15 and 2.16, we can calculate the total ion flux which is collected by Faraday cup. The total ion flux in the θ direction becomes

$$\Gamma_{\theta} \propto e\Delta\theta \frac{1}{4\pi} \left(\frac{P_{\perp}}{P_{\parallel}}\right)^{1/2} \left(\sin^2\theta + \frac{P_{\perp}}{P_{\parallel}} \cos^2\theta\right)^{-3/2} \quad 2.17$$

The signal ratio in the case of θ_1 to θ_2 is evaluated from Eq.2.17 and given by

$$R_{12} = \frac{(\sin^2\theta_1 + A \cos^2\theta_1)^{3/2}}{(\sin^2\theta_2 + A \cos^2\theta_2)^{3/2}} \quad \text{where} \quad A = \frac{P_{\perp}}{P_{\parallel}} \quad 2.18$$

A represents the pressure anisotropy. In Fig.2.7, the calculated pitch angle distribution which is normalized by the value of $\theta = 90^\circ$ is shown as a function of A . Experimentally obtained pitch angle distribution is also shown in Fig.2.7.

Charge-Exchange Neutral Particle Analyzer

Time-of-Flight Type Energy Analyzer

A time-of-flight type neutral-particle energy analyzer (TOF) placed at $z = 1.8$ m with the mirror ratio of $R = 1.16$ is schematically shown in Fig.2.8. The TOF is used for measurements of ion temperature in a relatively low energy range and for the estimation of radiation loss energy in the central cell²⁶⁾. Turning point of the ions with the pitch angle 70° is located in front of the TOF, then the TOF system dominantly measures the pitch angle of 70° in the ion distribution function of central cell midplane. The TOF mainly

consists of a chopper, a 3.5 m -long flight tube and Daly type detector. The chopper is beryllium-copper disc with 24 slits of 0.2 mm in width and rotates at about 40,000 r.p.m.. Charge-exchange neutral particle flux escaping from a plasma strikes a copper target after being chopped by the rotating disc. The target emits secondary electrons, and then the electrons are collected by the detector. Ion temperature is estimated from the spectrum of the secondary electron current as a function of the delay time after chopping.

TOF can discriminate between particle loss and radiation loss from plasmas by use of the difference between their flight times. The signals of TOF caused by the particle and photon are separately described as follows. The signal $S_{pa}^{\Theta}(E_j)$ for the particle loss with the pitch angle Θ in the energy range from $E_j - \Delta E/2$ to $E_j + \Delta E/2$ is

$$S_{pa}^{\Theta_{TOF}}(E_j) = C\eta(E_j)N_{pa}^{TOF}(E_j, \theta)|_{\theta=\Theta_{TOF}} \quad (\Theta_{TOF} = 70^\circ)$$

$$N_{pa}^{TOF}(E_j, \theta) = \Delta\tau \int_{-a}^a \int_{E_j-\Delta E/2}^{E_j+\Delta E/2} n_0(r)n_i(r) \langle \sigma_{cx}v \rangle f(E, \theta) \frac{\Omega}{4\pi} \Delta S \, drdE, \quad 2.19$$

where C is the efficiency of the detector which is geometrically determined. $\eta(E_j)$ is the secondary electron emission coefficient of copper for energy E_j and n_i is the ion density, n_0 is the neutral particle density, σ_{cx} is the charge-exchange cross section, $f(E, \theta)$ is the distribution function of ions, $\Delta\Omega$ is the solid angle subtended by the slit on the chopper disc at the center, ΔS the viewing area of the detector system and $\Delta\tau$ the gate time. Secondary electron emission coefficient $\eta(E)$ used here has been reported with uncertainly less than 25 %²⁷⁾. The uncertainly comes from mostly the technical error of measuring

$\eta(E)$ rather than from the surface conditions to the emitter material. The detected signal for photons in the j th energy range $S_{ph}^{\Theta TOF}(E_j)$ with photon energy from $E_j - \Delta E/2$ to $E_j + \Delta E/2$ is

$$S_{ph}^{\Theta TOF}(E_j) = C\bar{\gamma}_j \int_{E_j - \Delta E/2}^{E_j + \Delta E/2} I(E)dE = C\bar{\gamma}_j N_{ph}(E_j), \quad 2.20$$

where $\bar{\gamma}_i$ is the total efficiency averaged over the above energy range, $I(E)$ is the intensity of photons at energy E , $N_{ph}(E_j)$ is the total number of photons in the energy range ΔE_j . Typical time evolution of TOF signal is shown in Fig.2.9a. The first peak of the signal is caused by the photon and the following peaks are caused by the neutral particles. In Figures 2.9b and c, it is shown that the signal ratio of the photon to the neutral particle depends on both time and radial position. The ratio R_{ph} is defined as follows :

$$R_{ph} = \frac{\sum_{E_j} S_{ph}^{\Theta TOF}(E_j)}{\sum_{E_j} (S_{ph}^{\Theta TOF}(E_j) + S_{pa}^{\Theta TOF}(E_j))} \quad 2.21$$

The photon signal area is integrated over the time from the rising to the fall off of the first peak. The neutral particle signal area is integrated around the second peak which is concern with the particle energy spectrum. R_{ph} is represented by using the ratio of signal areas due to photons and particles. As described in the next paragraph, it is needed for the elimination of the photon signal from SED to obtain informations of the pitch angle distribution.

Pitch Angle Distribution Analyzer (Secondary Electron Detector)

Figure 2.10 shows schematically a secondary electron detector (SED) system. SED detects the secondary electrons emitted from the copper target on which and the neutral particle and photons impinge. The neutral particles which have informations on pitch angle and energy of ions are emitted from the plasma by the charge exchange process. Three SEDs are installed near the midplane with the angles of 45, 60 and 90 degrees with respect to the magnetic field line. The signal of SED should be described by integrating Eqs.2.19 and 2.20 of the TOF signals. The SED signal $I_{SED}(\Theta)$ with an angle Θ is represented by the sum of signals contributed for both neutral particles and photons.

$$I_{SED}(\Theta) = \sum_{E_j} \left(S_{pa}^{\Theta}(E_j) + S_{ph}^{\Theta}(E_j) \right) = \sum_{E_j} S_{pa}^{\Theta}(E_j) + \frac{R_{ph}}{1 - R_{ph}} \sum_{E_j} S_{pa}^{70}(E_j). \quad 2.22$$

$S_{pa}^{\Theta}(E_j)$ is the signal from the neutral particles from $E_j - \Delta E$ to $E_j + \Delta E$ detected by a SED with the angle Θ . $S_{ph}^{\Theta}(E_j)$ is the signal from the photon. $S_{pa}^{\Theta}(E_j)$ can be estimated by using the distribution function of Eq.2.16. The pressure anisotropy dependence of the signal ratios of 60° to 90° SED and 45° to 90° SED is estimated as a function of the photon ratio R_{ph} under the fixed energy distribution at the pitch angle of 70° which is shown in Fig.2.11.

2.3.2 Fluctuation Measurements

Magnetic Probe

Magnetic probe consists of a small pick up coil with 4 mm in radius and a stainless steel cover for shielding the coil from the charge-exchange fast neutral particles. Figure 2.12 shows schematically the measurement system of the magnetic probe. Small coils are made by a coated wire of 0.05 mm in diameter and are wound around a Teflon tube of 1.5 mm in diameter with 10 turns for r-component and 5 turn for θ -component. The signal of the magnetic probe is digitized in 8-bit by a digital oscilloscope DL2120b (Yokogawa Elec. Corp.) which has two channels of fast A/D converter with the maximum sampling of 200 MHz and a large memory of 128 kword/ch. The digital data is transferred to a personal computer PC-386 (Epson corp.) and stored in a digital audio tape (DAT) system (1 Gbyte/tape). By using the conventional fast fourier transform (FFT) methods, the signals are converted to the frequency spectrum. The cross correlation between two probe signals are analyzed. A hybrid combiner as shown in Fig.2.13 is used to discriminate between the electric and the magnetic component. The hybrid combiner consists of three identical coils, each with about 5 turns, trifilar-wound on a small toroidal ferrite core. Owing to the hybrid combiner, electrostatic noise is suppressed to a lower level. Relationships between the voltage are derived as follows :

$$v_1 = v = -v_3 \quad v_2 = -v = -v_3$$

$$\text{as a result} \quad v_1 - v_2 = 2v_3. \quad 2.23$$

Here, v is the voltage drop across each of the three transformer windings. $v_1 - v_2$ is the voltage induced by the pick up coil.

The magnetic probes are installed at $z = -1.28$ m, -1.12 m, 0.3 m, 0.9 m and 2.8 m, which are used for measuring parallel wave number, azimuthal mode number and radial profile of magnetic fluctuations. The magnetic probes at $z = -1.28$ m, -1.12 m and 2.8 m are radially movable to pick up the magnetic signal at any radial position. Probe measurements of magnetic fluctuations are attempted in the peripheral plasmas, because we must avoid the impurity contamination from the magnetic probes. Once the contamination reduces the plasma pressure, the AIC modes are not excited. The radial profile is measured near the mirror throat of the central cell, where the magnetic probe effect on the core plasma is minimized compare with those near the midplane.

The magnetic probe is calibrated by RF magnetic field which is induced by a Helmholtz coil. The calibrating system is shown in Fig.2.13. Figure 2.14 shows the example of the magnetic probe signal with a frequency $f = 3.84$ MHz which is obtained by using the calibration system. The difference between probe signals with and without a stainless steel cover in Fig.2.14. The field is uniform in the central region and is given by²⁸⁾

$$B = \frac{\mu_0 I}{a(1.25)^{1.5}} = 0.7155 \left(\frac{\mu_0 I}{a} \right). \quad 2.24$$

The radius and current of the Helmholtz coil are $a = 2.5 \times 10^{-2}$ m and $I = 0.2$ A·turn, respectively. Then the oscillating magnetic field strength of $B = 7.2 \times 10^{-6}$ T is produced with frequency $f = 3.84$ MHz. From Faraday's law $V = -d\Phi/dt = -SdB/dt = -2\pi SfB$, the effective area for picking up the oscillating magnetic field is obtained as follows :

$$S_{eff} = \frac{V}{2\pi fB} \times 2 = \frac{V}{174} \times 2 \text{ (m}^2\text{)}, \quad 2.25$$

here, the multiplier 2 is the effect of the hybrid combiner from Eq.2.23. The effective area S_{eff} in unit m^2 of each magnetic probe is shown as follows :

component	z=-1.29m	z=-1.14m	z=2.8m
r	20.0×10^{-6}	23.0×10^{-6}	23.0×10^{-6}
θ	46.0×10^{-6}	36.0×10^{-6}	23.0×10^{-6}

The coil areas of the magnetic probes with a stainless steel cover are as follows :

component	z=-1.29m	z=-1.14m	z=2.8m
r	17.2×10^{-6}	17.2×10^{-6}	8.6×10^{-6}
θ	17.2×10^{-6}	14.4×10^{-6}	12.0×10^{-6}

The cross section of r-component of the magnetic probe is about $S = \pi \times (0.75 \times 10^{-3})^2 \times 10 \sim 18 \times 10^{-6} \text{ m}^2$. In order to adjust a θ -component sensitivitie to r-component, the cross section of θ -component is twice of that of r-component because the stainless cover mainly decrease the sensitivity of θ -component. The calculated area S of the cross section

of the coil is within the error of less than 30 % as large as the effective area S_{eff} . We can obtain a level of the magnetic fluctuation by using the following relation

$$B = \frac{V}{2\pi f S_{eff}} \quad 2.26$$

The stainless steel cover reduces the probe sensitivity of the θ -component by about 30 % compared with that without the cover. It is confirmed that the probe system shows no resonance which is caused by a stray capacitance and inductance because the magnetic probe signal increases proportionally with the frequency up to 20 MHz.

Electrostatic Probes

Electrostatic probes are installed at $z = -0.6$ m, $z = 0.3$ m and $z = 5.0$ m. The electrostatic probes are biased at -200 V in order to measure density fluctuations from the ion saturation currents. The voltage is sufficiently biased to saturate the ion current on the characteristic curve of the electrostatic probes. The curves show that the floating potential lies at about several hundred volts about the grounded potential. At $z = 0.3$ m, the electrostatic probes are azimuthally arrayed with the angle of 45 degree, which measure the azimuthal mode number. The electrostatic probes at $z = -0.6$ and 5.0 m measure the wave number along the magnetic field line by analyzing the cross correlation between the two probe signals. At the inner transition region $z = -3.7$ m and the outer transition region $z = 6.7$ m, radially scannable electrostatic probes are installed to

measure the radial profiles of the ion saturation current and the floating potential. The ion current of the electrostatic probe is picked up by a resistor of 1Ω , amplified by an isolation amplifiers P-64 and P62A (NF Elec. Inst.), AD-converted to 12-bit digital data by a digital oscilloscope DL1200E (Yokogawa Elec. Corp.), transferred to a personal computer and stored in the DAT storage system.

Quantitative Estimation of Pressure Anisotropy

3.1 Pressure Profile Model

Proceeding to quantitatively estimating the pressure anisotropy by using the three-dimensional magnetic loop is described in this section. In an infinite and homogeneous plasma column, the diamagnetic loop signal is proportional to the local plasma pressure. The finite length and finite coil which induces magnetic field is proportional to the current density in the plasma column. If the coil has a square shape in the axial direction and a length $2a$ in the radial direction, the induced magnetic field is still proportional to the local plasma pressure owing to the negligible coil effect. The diamagnetic loop signal is estimated by integrating the total magnetic field over the length of the coil.

Chapter 3

Quantitative Estimation of Pressure Anisotropy

3.1 Pressure Profile Model

Procedure for quantitatively estimating the pressure anisotropy by using the three diamagnetic loops is described in this section²⁹⁾. In an infinite and homogeneous plasma column, the diamagnetic loop signal is proportional to the local plasma pressure. An infinite-length solenoidal coil which induces magnetic flux proportional to the current density is the closest analogy. If the coil has a varying radius in the axial direction and a finite axial length, however, the induced magnetic flux is not proportional to the local current density owing to the fringing field effect. The diamagnetic loop signal is affected by an axial profile of the plasma pressure and must be evaluated by integrating the local

current density³⁰).

First, we assume a perpendicular pressure profile as follows :

$$P_{\perp}(\Phi, z) = P_0 [1 - H(\Phi - \Phi_0)] \xi(z) \quad 3.1$$

$$\Phi_0 = \frac{r_0^2 B(z=0)}{2} \quad 3.2$$

Here, Φ is the magnetic flux, Φ_0 is the magnetic flux at $z = 0$ m, $H(\Phi)$ is Heaviside's step function, r_0 is the plasma radius, P_0 is the perpendicular pressure at $z = 0$ m and B is the externally applied magnetic field. In Eq.3.1 P_{\perp} is homogeneous in the radial direction and the axial profile is represented by $\xi(z)$. We select four types of $\xi(z)$ as follows :

$$\text{Type A} \quad \xi(z) = \max\left[1 - \frac{z^2}{L^2}, 0\right] \quad 3.3$$

$$\text{Type B} \quad \xi(z) = \exp\left(-\frac{z^2}{L^2}\right) \quad 3.4$$

$$\text{Type C} \quad \xi(z) = \max\left[\frac{B_L^2 - B^2}{B_L^2 - B_0^2}, 0\right] \quad 3.5$$

$$\text{Type D} \quad \xi(z) = \left(\frac{B}{B_0}\right)^2 \left(\frac{B_T - B}{B_T - B_0}\right)^{n-1} \quad 3.6$$

Here, L is a scale length, B_L , B_0 and B_T are the magnetic field strengths at $z = L$, $z = 0$ and at the mirror throat located at $z = 2.8$ m, respectively, and n is a free

parameter. Figure 3.1 shows P_{\perp} and P_{\parallel} profiles corresponding to the four types of $\xi(z)$ with $L = 2$ m and $n = 50$. Type A is a parabolic profile and Type B is a Gaussian profile, both of which depend on the z -position. Type C is an ideal distribution conventionally used in the calculation of the ballooning mode³¹⁾. Type D is a pressure profile obtained when the ion distribution function is assumed as $f(\epsilon, \mu) = (\mu - \epsilon)^{n-\frac{3}{2}}g(\mu)$, where ϵ is the total energy, μ is the magnetic moment of ions and $g(\mu)$ is an arbitrary function³²⁾. The function $g(\mu)$ does not appear distinctly in the pressure distribution of Type D, because it is contained in the constant P_0 , which is evaluated in the process of integrating the distribution function. This distribution function proposed by Taylor satisfies the MHD equilibrium condition³³⁾. By use of the conventional two-component pressure tensor of the collisionless guiding-center fluid theory, the MHD equilibrium condition is given as follows³⁴⁾:

$$\frac{\partial}{\partial B} \left(\frac{P_{\parallel}}{B} \right) = -\frac{P_{\perp}}{B^2}. \quad 3.7$$

B is the externally applied magnetic field. This equation gives the relationship between the perpendicular and the parallel pressures. When the axial profile of the perpendicular pressure is obtained, the profile of the parallel pressure is evaluated numerically from Eq.3.7. In the cases of Type B and Type D, the boundary condition is $P_{\parallel} = 0$ at the mirror throat. In the cases of Type A and Type C, the boundary condition is $P_{\parallel} = 0$ at $z = \pm L$ m.

The diamagnetic currents in a plasma with a finite axial extent are determined from the balance between the Lorentz force and the pressure gradient force. The signals picked up by each diamagnetic loop can be estimated as an integrated magnetic flux induced by the axially distributed diamagnetic current. As a result, from the pressure profile represented with an arbitrary scale length, the signal ratios of the third loop to the midplane loop and the second loop to the midplane loop are evaluated. Figure 3.2a shows the relationship between the ratio of the second loop signal to the midplane loop signal and the scale length L and n . Figure 3.2b shows the calculated relationships of the diamagnetic loop signal at the locations of the second loop and the third loop which are normalized to the diamagnetic loop signal at the location of the midplane loop for the four types of pressure profiles defined above. In Fig.3.2c, the calculated anisotropy at the midplane is shown as a function of the normalized diamagnetic loop signal of the second loop. It can be clearly seen that there remains ambiguity in determining the anisotropy in Fig.3.2 when only two diamagnetic loops are used. The anisotropy can be determined from comparing the experimentally obtained ratios between the diamagnetic loops with those of the calculated ratio, as shown in Fig.3.2b and Fig.3.2c. When data point is not located on the assumed distribution, the anisotropy can be represented by a linear combination of the two neighboring distributions in Fig.3.2b and Fig.3.2c.

3.2 Experimental Results and Discussion

As shown in Fig.3.2c, a temporal evolution of the diamagnetic signals indicates the pressure anisotropy. The signals of the second and the third loops normalized by the midplane loop are plotted in Fig.3.2b. The experimentally obtained ratio of the diamagnetic fluxes at $t = 56$ ms lies exactly on the curve of Type C with the scale length of $L = 1.9$ m. On the other hand, the ratio of the diamagnetic loop signal at $t = 60$ ms corresponds to the distribution of Type A. It is clearly seen that the axial pressure profile varies temporally and cannot be described by only one of the pressure distributions assumed in the previous section.

Effect of an isotropic cold ion component on the diamagnetic loop signals has been estimated. The hot ion temperature is by more than five as high as the cold ion temperature, which is evaluated by a small Faraday cup installed in the transition region between the central and anchor cells, as shown in Fig.2.4. Because the distribution of the cold ions is more isotropic than that of the hot ions, the ions in the losscone of the central cell will be dominated by such cold ions. The number of cold ions is determined from measurement by a microwave interferometer installed at the central-cell mirror throat, where the isotropic component should be dominant. The line density of the mirror throat is less than one-half of the line density of the central cell. As a result, contribution of the cold ions to the total plasma pressure is less than ten percent of that of the hot ions.

In order to estimate effect of the radial pressure profile, the relationship between

the anisotropy and the ratio of the second loop signal to the midplane loop signal is calculated in the case of two different plasma radii of 0.9 m and 0.18 m. It is shown from the calculation that Figs.3.2b and 3.2c are hardly modified by the difference in the plasma radius. The assumption of the homogeneous pressure profile in the radial direction will be adequate, because an inhomogeneous pressure profile by the superposition of homogeneous pressure profiles which different radii.

Extended Model of Pressure Profile

When a data point satisfies the calculated relations in the previous section, the anisotropy is only approximately estimated in Fig.3.2. When the data point lies in the outer region which is not covered by the model, the anisotropy can not be estimated. Axial pressure profiles in the anchor, transition and plug/barrier cell is required for an analysis of flute-interchange instability. In order to improve this problem, a new model of the pressure profile is developed. The new model is more flexible because of the adoption of two free parameters and includes the pressure profiles in the anchor, transition and plug/barrier cells. The profile is shown as follows :

$$P_{total} = P_{\perp}^h + P_{\parallel}^h + P_{\perp}^c + P_{\parallel}^c = \text{hot} + \text{cold} \quad 3.8$$

•hot component

$$P_{\perp}^h(z) = \begin{cases} (1 - B/B_{L_C})^{n_C} & \text{for } 0 < z < 2.8\text{m} \\ (1 - B/B_{L_A})^{n_A} & \text{for } 4.5 < z < 6.0\text{m} \\ 0 & \text{for else} \end{cases}$$

$$P_{\parallel}^h(z) \quad \text{from MHD equilibrium (see Eq.3.7)}$$

•cold component

$$P_{\perp}^c(z) = P_{\parallel}^c(z) = P_c = \text{constant.}$$

where B is the magnetic field strength, L_C and L_A the scale lengths, n_C and n_A the shaping factors for the hot component pressure in the central and anchor cells, suffixes h and c for the hot and cold components, \perp and \parallel the directions perpendicular and parallel to the magnetic field line, respectively. It is considered that the cold components P_c does not depend on the axial position z because the cold plasma component is thermalized owing to the short collision time. By using the new pressure model in the computer code described in the section 3.1 estimated the ratio of the diamagnetic loop signals. Because of the isotropic cold plasma, the assumption of $P_{\perp}^c = P_{\parallel}^c$ is valid. Figure 3.3a shows the relationship between the ratio of the second loop signal to the midplane loop signal and the scale length L_C and n_C . Figure 3.3b shows the calculated relationships of the diamagnetic loop signals of the second loop and the third loop which are normalized by the diamagnetic loop signal at the midplane for the pressure profiles defined above. In this calculation, the cold pressure component is included with a fraction of 10 % of the hot

pressure at the midplane of the central cell $z = 0$ m. In Fig.3.4, the calculated anisotropy at the midplane is shown as a function of the scale length L_C in various cases of n_C . The new model of the pressure profile extends the covered parameter region in comparison with the model described in the section 3.1.

Chapter 4

Alfvén Ion Cyclotron Instability

4.1 Physical Picture of AIC Mode

In this subsection, we present the physical picture of the AIC mode by using a combination of a single-particle model and a fluid approximation. We consider a plasma state which is uniform along the magnetic field line with the left-hand-side magnetic configuration. The equilibrium field is represented as follows

$$\mathbf{E} = -\nabla\phi, \quad \mathbf{B} = B_0 \hat{z} + \nabla\psi \times \hat{z},$$

Chapter 4

Alfvén Ion Cyclotron Instability

4.1 Physical Picture of AIC Mode

In this subsection, we present the physical picture of the AIC mode by using a combination of a single particle motion and a fluid approximation³⁵⁾. We consider a plane wave which propagates along the magnetic field line with the left-handed circular polarization. The wave electric field is represented as follows :

$$\mathbf{E}_\perp = \mathbf{e}_x |\mathbf{E}_\perp| \cos(kz - \omega_0 t) + \mathbf{e}_y |\mathbf{E}_\perp| \sin(kz - \omega_0 t). \quad 4.1$$

Here, the wave number is k , the angular frequency ω_0 and the wave electric field \mathbf{E}_\perp . The velocity of ion in a gyration motion is given as

$$\mathbf{v}_{\perp 0} = \mathbf{e}_x v_\perp \cos(\Omega_{ci}t - \phi_i) - \mathbf{e}_y v_\perp \sin(\Omega_{ci}t - \phi_i). \quad 4.2$$

The unit vectors in the direction of the x- and y-axes are \mathbf{e}_x and \mathbf{e}_y , The ion cyclotron angular frequency Ω_{ci} and the initial phase of the i th particle is ϕ_i . The substitution of Ampere's law into the equation of motion in the parallel direction yields

$$\frac{d\mathbf{v}_\parallel}{dt} = \frac{q}{m} \mathbf{v}_{\perp 0} \times \mathbf{b}_\perp = \frac{q}{\omega_0 m} \mathbf{v}_{\perp 0} \times (\mathbf{k} \times \mathbf{E}_\perp). \quad 4.3$$

By solving Eq.4.3, we obtain the parallel velocity as follows :

$$v_\parallel = \frac{qE_\perp v_\perp k}{m \omega_0 \Omega_{ci} - \omega_0} \sin [kz - \phi_i + (\Omega_{ci} - \omega_0)t]. \quad 4.4$$

We define the pressure tensor \mathbf{P}

$$\mathbf{P} = \begin{pmatrix} P_{xx} & P_{xy} & P_{xz} \\ P_{yx} & P_{yy} & P_{yz} \\ P_{zx} & P_{zy} & P_{zz} \end{pmatrix} \quad 4.5$$

P_{zx} and P_{zy} components of the pressure tensor are evaluated using Eqs.4.2 and 4.4 as follows :

$$\begin{aligned} P_{zx} &= \langle v_{\parallel} v_{\perp 0x} \rangle = \frac{qE_{\perp} k v_{\perp}^2}{2m\omega_0(\Omega_{ci} - \omega_0)} \sin(kz - \omega_0 t) \\ P_{zy} &= \langle v_{\parallel} v_{\perp 0y} \rangle = \frac{qE_{\perp} k v_{\perp}^2}{2m\omega_0(\Omega_{ci} - \omega_0)} \cos(kz - \omega_0 t). \end{aligned} \quad 4.6$$

The fluid equation for ions in the perpendicular direction is

$$\frac{d\mathbf{v}_{\perp}}{dt} = \frac{q}{m} \mathbf{E}_{\perp} + \frac{q}{m} \mathbf{v}_{\perp} \times \mathbf{B}_0 - \frac{1}{nm} \left(\frac{\partial P_{zx}}{\partial z} \mathbf{e}_x - \frac{\partial P_{zy}}{\partial z} \mathbf{e}_y \right) \quad 4.7$$

The velocity displacement due to the stress of the pressure tensor is evaluated from Eq.4.7 as follows :

$$\delta \mathbf{v}_{\perp} = \frac{q|\mathbf{E}_{\perp}|}{m(\Omega_{ci} - \omega_0)} \left[1 - \frac{1}{2} \frac{k^2 |\mathbf{v}_{\perp}|^2}{\omega_0(\Omega_{ci} - \omega_0)} \right] [\mathbf{e}_x \sin(kz - \omega_0 t) - \mathbf{e}_y \cos(kz - \omega_0 t)]. \quad 4.8$$

The net current which is induced by the pressure tensor is given by

$$\mathbf{j} = nq\delta \mathbf{v}_{\perp}. \quad 4.9$$

The current which is represented as Eq.4.9 is fed back to the perturbed magnetic field and amplify the fluctuation. Figure 4.1 shows the schematic of the ion motions which are derived from Eqs.4.2 and 4.3. Tilting discs correspond to the trajectory of gyrating

ions with the perpendicular velocity of $v_{\perp} = v_{\perp 0}$. Because we consider the anisotropic ion distribution, the discs are fixed at an initial fixed point along the magnetic field line. Figure 4.1a shows a gyration motion of a single ion. When the magnetic field fluctuation b_{\perp} is directed upward and the phase of the gyration motion varies uniformly from 0 to 180 degree, the velocity vector of the ion inclines to the positive direction of the z-axis. When the gyration phase is from -180 to 0 degree, the velocity vector tilts in the negative z-direction. If the magnetic fluctuations with left-handed polarization are spontaneously excited, the ion begins the tilting motion. The net current due to the tilting motion is in the perpendicular direction to the z-axis and 90 degree out of phase against the magnetic fluctuation. As a result, the net current is fed back to the magnetic fluctuation as shown at $t = 2\pi/\omega_0$ in Fig.4.1 and the fluctuation can grow up.

4.2 Observation and Identification of Fluctuations

Figures 4.2a and 4.2b show a temporal evolution of (a) the line-integrated electron density using a millimeter wave interferometer at $z = -0.6$ m and (b) diamagnetic loop signals which are measured with three diamagnetic loops. The discharge starts at 50 ms when initial gun-produced plasmas are injected. The on-axis plasma density is $3 \times 10^{18} \text{ m}^{-3}$, the averaged β_{\perp} is 1 % and the averaged perpendicular temperature is 3.6 keV at 60 ms. Figure 4.3 shows the RF power dependence of the beta value and the pressure anisotropy in the central cell. The beta value is defined as a product of the density at the center and

the radially averaged temperature. The density profile is assumed to be parabolic profile in the radial direction. The pressure anisotropy is evaluated using the diamagnetic loop array which is described in chapter 3. The evaluated pressure profile well fitted to the Type D in Eq.3.6. The beta value of the central cell increases with the increase in RF power. The pressure anisotropy becomes strong and reaches 12.5 at 100 kW of the RF power and saturates suddenly.

As shown in Fig.4.3, the evaluated anisotropy should be large enough to induce the microscopic instabilities which are driven by the pressure anisotropy and the plasma β_{\perp} value. In GAMMA 10, magnetic field fluctuations near the ion cyclotron frequency measured with small magnetic probes are studied as a function of the pressure anisotropy and the plasma β_{\perp} value. Figure 4.4 shows a typical frequency spectrum of the magnetic fluctuation obtained from the conventional FFT (fast Fourier transform) analyses. Fluctuation measurements with the magnetic probes are performed in the peripheral region in order to minimize the disturbance to the core plasmas. The peaks at 6.3 MHz and 9.9 MHz in the figure correspond to the frequencies externally applied by the RF antennas. The peaks from 5.6 MHz to 5.9 MHz are the spontaneously excited fluctuations. These fluctuations are observed, only when both the anisotropy and the plasma β_{\perp} are relatively high. The frequencies of the fluctuation are below the ion cyclotron frequency at the midplane. There are some discrete peaks. The frequency differences between the adjacent two spectral peaks side by side becomes narrower with higher frequency peaks than with lower frequency peaks.

Figure 4.5a shows a parameter space of β_{\perp} vs $(P_{\perp}/P_{\parallel})^2$ obtained experimentally. The solid circles show the data in the parameter range where the fluctuations are observed and the open circles the data without fluctuations. The criterion of the excitation of the fluctuations is defined as the minimum amplitude of the fluctuation of 1×10^{-7} T which is determined by the sensitivity of the magnetic probes and the precision of the FFT method. The amplitude of the wave magnetic field excited by the ICRF antenna is typically about 1×10^{-4} T.

Figure 4.5b shows the dependence of the fluctuation amplitude on an AIC driving term. Here, the AIC driving term is defined as $\beta_{\perp}(P_{\perp}/P_{\parallel})^2$ which is a product of the two parameters on the vertical and transverse axes in Fig.4.5a. The fluctuations are observed in the parameter region of the AIC driving term beyond 0.3. The fluctuation amplitude increases with increase of the AIC driving term. The fluctuation amplitude measured by the magnetic probe at the $z = -1.12$ m have the maximum amplitude at the AIC driving term of 1.2. On the other hand, the fluctuations at the $z = -1.28$ m have the maximum at the AIC driving term of 1.5.

Dispersion relation of the AIC mode is as follows³⁶⁾:

$$D(k, \omega) = k^2 c^2 - \omega^2 + \sum_{j=e,i} \Omega_{pj}^2 \chi_j(k, \omega) = 0, \quad 4.10$$

where Ω_{pi} is the plasma frequency, Ω_{ci} is the ion cyclotron frequency, k is the axial wave number, ω is the frequency of the AIC mode and χ is the plasma susceptibility (see

Appendix B Eqs.B.13 and B.16). Figure 4.6 shows a typical dispersion relation of the AIC mode which is derived by solving Eq.4.10 with respect to the real wave number k_r . Here, the pressure anisotropy and β_{\perp} of 12.5 and 0.007 are used, respectively. The maximum growth rate $[\omega_i/\Omega_{ci}]_{MAX}$ is defined as a peak value of the imaginary frequency which is shown by a dotted-broken line in Fig.4.6. The solid lines in the Figure 4.5a indicate contour of maximum growth rate, $[\omega_i/\Omega_{ci}]_{MAX}$ of 10^{-5} and 10^{-2} which are calculated from Eq.4.10. The dotted line shows a boundary between the absolutely and convectively unstable regions of the AIC mode¹²⁾.

In Fig.4.7 it is shown that the frequency of the fluctuations depends on the strength of the externally applied magnetic field in the range from 0.3 to 0.6T. Using an appropriate frequency of the RF2 system for the ion heating in the central cell, the resonance layer is fixed near the midplane of the central cell. Thereby, the heating geometry is not modified even in the various strengths of the magnetic field, where the pressure profiles are also peaked at the midplane in the central cell. A solid line shows the ion cyclotron frequency of the minimum strength of the magnetic field in the central cell. Broken, dotted-broken and dotted lines correspond to frequency of $0.9\Omega_{ci}$, $0.85\Omega_{ci}$ and $0.8\Omega_{ci}$, respectively. Here, Ω_{ci} is the ion cyclotron frequency at $z = 0$ m. The frequencies of the fluctuations are slightly below the ion cyclotron frequency. This dependence agrees well with the prediction from the dispersion relation of the AIC mode.

Figure 4.8 shows the wave structure in the azimuthal direction. The azimuthal mode number m is measured by magnetic probes which pick up the radial component b_r of the

fluctuations and are azimuthally arrayed at $z = 0.3$ m. Four magnetic probes are set on the angles of 0, 22.5, 45 and 90 degrees with the x-axis. The magnetic fluctuations have azimuthal mode number of $m = -1$ or -2 . This means that the fluctuations propagate in the ion diamagnetic direction and have the wavelength equals to the circumference of the plasma column. As mentioned above in Fig.4.4, several spectra peaks are observed. These peaks have the same azimuthal structure.

Figures 4.9 show radial profiles of each peak which are measured at the mirror throat of the central cell. Ions are accelerated up to a high energy of several keV and trapped near the midplane of the central cell. Therefore, most of the high energy ions cannot reach the mirror throat. Then the contamination due to impurities from the probe surface which are bombarded by the high energy ions would be reduced. The frequencies of each peak are (a) $f \approx 5.50$ MHz, (b) $f \approx 5.55$ MHz, (c) $f \approx 5.65$ MHz and (d) $f \approx 5.75$ MHz. The amplitude profiles of the radial component b_r as well as the azimuthal component b_θ are plotted for each spectrum peak in Fig.4.4. The fluctuation amplitudes are larger in the core region than in the edge region. This means that the observed modes have a property of body waves not of surface wave. Profile of the phase difference between the b_r and b_θ components at the frequency shown in Fig.4.9 is shown in Fig.4.10. The polarization in this figure is defined as follows :

$$P_L = \frac{b_L^2}{b_L^2 + b_R^2} \quad P_R = \frac{b_R^2}{b_L^2 + b_R^2} \quad 4.11$$

$$b_L = \frac{b_r + ib_\theta}{2} \quad b_R = \frac{b_r - ib_\theta}{2} \quad 4.12$$

P_L shows ratio of the square of the magnetic fluctuation strength with left-handed polarization to that to the total fluctuation strength. Figure 4.10 shows that the left-handed polarization dominates in the center region of plasmas, while the right-handed polarization in the outer region for all spectral peaks. This result is consistent with the experimental observation that the AIC mode are shear Alfvén waves excited by the free energy of the anisotropic distribution function.

It is concluded that the magnetic fluctuations are identified as the AIC mode from the experimental results on the frequency dependence on the magnetic field strength, the excitation condition depending on the pressure anisotropy and β_{\perp} and the consistency with the shear Alfvén wave properties with respect to the radial and azimuthal wave propagation^{37,38}).

Figure 4.11 shows that axial wave numbers of the AIC mode depend on the AIC driving term. The wave number is evaluated from the phase difference between the fluctuation signals which are detected using two magnetic probes along the magnetic field line. It is shown that the wave numbers converge to zero with the increasing AIC driving term. This behaviour on the wave number also depends on the position of the magnetic probe along the magnetic field line. When the magnetic probes at $z = 0.3$ and 0.9 m are used, the zero wave number is observed at lower driving term than that at $z = -1.12$ and -1.28 m. The measured wave number of $k = 0$ could be attributed to the standing wave. As a result, it is indicated that the AIC mode has two regions along the magnetic field line; one is a central region with a standing wave near the midplane and the other is a propagating

wave region at both sides of the standing wave region. This type of Alfvén wave structure has been observed in single mirror experiments on ballooning instabilities³⁹⁾.

The expansion of the standing wave region corresponds to the axial expansion of the AIC driving term. The axial structure of the AIC mode is schematically drawn in Fig.4.12. The axial AIC-driving-term profile determined by using the diamagnetic loop array is represented by a solid line in Fig.4.12.

4.3 Spatial Structure and Excitation Condition

4.3.1 New Theory for AIC Eigenmodes

It is predicted theoretically that the AIC mode is to be unstable in the region of $\beta_{\perp}(P_{\perp}/P_{\parallel})^2 > 3.5$ which corresponds to the absolutely unstable region in the case of infinite and homogeneous plasmas. If an initial perturbation is excited with a thermal noise level in a finite-length system, the maximum growth level is restricted by the system length in the case of the convectively unstable. The initial perturbation can grow up from an excitation point to an observation point. The group velocity v_g of the AIC mode with the maximum growth rate $[\omega_i/\Omega_{ci}]_{MAX}$ is evaluated from Fig.4.6 as follows :

$$v_g = \frac{d\omega}{dk} = \frac{\Delta\omega}{\Delta k} = \frac{\Delta\omega/\Omega_{ci}}{\Delta kc/\Omega_{pi}} \times \frac{\Omega_{ci}}{\Omega_{pi}/c} = 0.473 \times \frac{\Omega_{ci}c}{\Omega_{pi}} \quad 4.13$$

The propagation time Δt for a typical length $\ell = 5$ m from the generated point to the observation point is

$$\Delta t = \frac{\ell}{v_g} = \frac{\Omega_{pi} \ell}{0.473 \Omega_{ci} c} = \frac{30}{0.473} \frac{1}{\Omega_{ci}} = \frac{63.4}{\Omega_{ci}}. \quad 4.14$$

The AIC mode grows during Δt as follows :

$$\exp([\omega_i]_{MAX} \Delta t) = \exp\left(\left[\frac{\omega_i}{\Omega_{ci}}\right]_{MAX} \times 63.4\right) = \exp(0.005 \times 63.4) = 1.4. \quad 4.15$$

This estimation indicates that the amplitude of the fluctuation becomes large enough for the detection when it is excited with a thermal-noise level and propagates to the observation point.

In GAMMA 10, the AIC mode is observed in the region of the $\beta_{\perp}(P_{\perp}/P_{\parallel})^2 > 0.3$. This observation indicates that the AIC mode is sufficiently growing for the detection in the convectively-unstable parameter region and needs for an analysis including finite length effects, which is described in the following part.

We consider the boundary problem which is drawn schematically in Fig.4.13⁴⁰⁾. Two reflection points are assumed to be at $z = \pm \frac{L}{2}$ and an initial perturbation is excited at $z = 0$. The wave number k and the frequency ω are defined as complex numbers $k_r + ik_i$ and $\omega_r + i\omega_i$. The wave propagation in the positive z -direction has a wave number k_+ and the other wave propagation in the negative z -direction has a wave number k_- . We denote

k_+ and k_- as poles of Green's function derived from the wave equations which yield the dispersion relation of Eq.4.10. As $\omega_i \rightarrow [\omega_i]_{MAX}$, k_+ and k_- are in the upper and lower half-plane of complex k-plane⁴¹⁾, respectively. Asymptotic expressions far from $z = 0$ for the waves which propagate from the midplane in the positive and negative z-directions is

$$\phi_+ = a \exp [i (k_+ z - \omega t)] \quad 4.16$$

$$\phi_- = a \exp [i (k_- z - \omega t)]. \quad 4.17$$

After a reflection from the right-hand boundary at $z = \frac{L}{2}$, ϕ'_+ propagates to the left, and at sufficiently long distance from the boundary takes an asymptotic form as follows :

$$\phi'_+ = aR \exp \left(\frac{ik_+ L}{2} \right) \exp \left\{ i \left[k_- \left(z - \frac{L}{2} \right) - \omega t \right] \right\}. \quad 4.18$$

ϕ_- is also reflected and has the asymptotic form,

$$\phi'_- = aR \exp \left(\frac{-ik_- L}{2} \right) \exp \left\{ i \left[k_+ \left(z + \frac{L}{2} \right) - \omega t \right] \right\}. \quad 4.19$$

The ϕ'_+ is reflected again at $z = -\frac{L}{2}$ and reflected wave ϕ''_+ has the asymptotic form,

$$\phi''_+ = aR^2 \exp \left(\frac{ik_+ L}{2} \right) \exp (-ik_- L) \exp \left\{ i \left[k_+ \left(z + \frac{L}{2} \right) - \omega t \right] \right\}. \quad 4.20$$

The condition for the standing wave formation is given by

$$\phi_+ = \phi_+'' + \phi_-'. \quad 4.21$$

The substitutions of Eqs.4.16,4.19 and 4.20 into Eq.4.21 yield

$$\begin{aligned} X^2 + X - 1 &= 0 \\ X &= R \exp \left[\frac{i(k_+ - k_-)L}{2} \right] \end{aligned} \quad 4.22$$

Then, the eigen value equation is written in term of k_+ and k_- as follows :

$$\begin{aligned} k_{+r} - k_{-r} &= \frac{4n\pi}{L} \\ k_{+i} - k_{-i} &= \frac{1}{L} \left[2 \ln R + \ln \left(\frac{3 + \sqrt{5}}{2} \right) \right] \end{aligned} \quad 4.23$$

Here, n is an axial mode number and R a reflection coefficient. k_+ and k_- are given by the dispersion relation $D(k, \omega) = 0$ of Eq.4.10. The equations are solved by using the simplex method⁴²⁾. Figure 4.14 shows the eigenmode in term of k_+ which is evaluated from Eq.4.23. The boundary length $L\Omega_{pi}/c$, reciprocal of pressure anisotropy τ , beta value β_1 and reflection coefficient are given as 20, 0.08, 0.007 and $\sqrt{0.5}$. The real and imaginary parts of the frequency and the imaginary part of the wave number are derived as a function of the real part of the wave number. The unstable eigen modes have the negative imaginary part of the wave number and the positive imaginary part of the frequency. In

the case of Fig.4.14a, unstable waves have the mode numbers of $n = 8, 9, 10$ between the boundary length L . This theoretical model can explain the discrete spectrum and the frequency difference between spectrum peaks which becomes narrower at the higher frequency side than at the lower frequency side. Figure 4.14b shows a contour map of the amplitude of the AIC mode which shows the axial profile and time development of the AIC mode corresponding to the dispersion relation of Fig.4.14a. The axial mode number n is 8. Both z - and t -axis are non-dimensional parameter which are normalized by a product between the inversed plasma oscillation frequency and the light speed and the ion inversed gyration frequency, respectively. At the inner region between the reflection points of $z = \pm L/2$, the AIC mode forms the standing wave structure. At the outer regions, the AIC mode propagates in the outer direction.

The eigenmodes depend on the parameters of L , R , β_{\perp} and τ defined above. Figures 4.15a and 4.15b shows the drive term dependence of the AIC-mode frequency. The AIC driving term is a product between the beta and the square of the pressure anisotropy. In Fig.4.15a, the AIC driving term increases with the increasing β_{\perp} under the fixed pressure anisotropy. On the contrary, the AIC driving term increase with decrease of τ in Fig.4.15b under the fixed β_{\perp} . When the β_{\perp} increases, the new eigenmodes appear from the low frequency side as shown in Fig.4.15a. As the free energy originated from the pressure anisotropy is increasing, the new unstable eigenmodes appear from the high frequency side as shown in Fig.4.15b. In both Figs.4.15a and 4.15b, the frequency of the eigenmode increases and the frequency interval between each mode and are contracted with increase

of the AIC driving term. When the length L is varied, the mode are drastically changed as shown in Fig.4.15c. A new mode appears from the higher frequency side. Its frequency decreases and disappears at the lower frequency side with increase in the boundary length L .

4.3.2 Experimental Results and Discussion

In this section, the experimentally obtained spectra of the AIC mode is compared with the spectra which are derived from the new theory in the previous section. In the initial startup phase, the temperature, density and anisotropy increase temporally. It is shown in the measurement of the diamagnetic loop array that the axial length of the hot plasma region is extended in this phase. The frequency of the AIC mode move to higher frequency side and the frequency difference between spectrum peaks get narrower as shown in Fig.4.16. It is rather difficult to control precisely plasma parameters such as P_{\perp}/P_{\parallel} and β_{\perp} in the plasma startup phase because of the lack in the reproducibility of plasmas. Hence, the comparison between the experiment and theory is very difficult in the start up phase.

In order to obtain a reproducible plasma parameters, the AIC driving term is controlled by the pulse modulation of the RF2 power for the ion heating of the central cell. The time evolution of the line density, diamagnetic signal and RF input power including the power loss of the circuit are shown in Figs.4.17a,b,c. The input power of the RF2 is modulated down from 75 ms to 85 ms. The line density slightly decreases and the diamagnetic loop

signal drastically decreases mainly due to the reduction of the ion temperature.

Figure 4.18 describes the AIC driving term dependence of the frequency of the spectrum peaks which are normalized by the ion cyclotron frequency $\Omega_{ci}/2\pi = 6.335$ MHz at the position of the magnetic probe. The frequencies of the spectrum peak increase with an increase in the AIC driving term. The frequency difference between the peaks becomes narrower and the number of the eigenmode increases. Solid lines are the frequencies of the unstable mode of the AIC instability evaluated theoretically and agree well with the experimentally-obtained data. The parameters of τ , R^2 and $L\Omega_{pi}/c$ are fixed at 0.08, 0.5 and 20, respectively. The boundary length L is 3.2 m which is corresponding to the density of $2 \times 10^{18} \text{ m}^{-3}$. It is confirmed that the reflection coefficient R does not influence on the frequency spectrum but on the growth rate of the AIC mode.

Figure 4.19a shows the AIC driving term dependence of the reciprocal of the pressure anisotropy τ and β_{\perp} . Because the pressure anisotropy is almost constant $\tau = 0.08$ above $\beta_{\perp}(P_{\perp}/P_{\parallel})^2 \sim 0.8$, the increase in the AIC driving term in the region above $\beta_{\perp}(P_{\perp}/P_{\parallel})^2 \sim 0.8$ is originated from the increase in β_{\perp} . Figure 4.19b shows the axial profiles of the AIC driving term which are drawn by four vertical lines (I),(II),(III) and (IV) in Fig.4.19a. Each line corresponds to a particular condition which is as follows. The boundary length L depends on the extension of the hot ion distribution. When the axial profiles of the AIC driving term are (I) and (II), the boundary crosses over in front of the magnetic probes which are installed at $z = 1.28$ m and $z = 0.90$ m in Fig.4.11. Hence, the boundary length L is determined as 2.6 m and 1.8 m with respect to (I) and (II) profiles. From the

theoretical calculation of the frequency spectrum, the boundary length L is given as 3.2 m in Fig.4.18, which is represented by the profile of (III) in Fig.4.19b. The case of the maximum AIC driving term in Fig.4.19a is described by the profile of (IV) in Fig.4.19b. The critical values of the AIC driving term at the reflection point of the AIC mode are experimentally obtained as 4.6 and 5.4 corresponding to (I) and (II) of Fig.4.19b. The averaged critical value of the AIC driving term is 5.0. As a result, the boundary length of the profile (III) is determined as 3 m which is a good agreement with the theoretical value within the ambiguity of the estimation. In Fig.4.19b, the boundary length are little expanded in profile (IV) when the AIC driving term increases at the midplane. Hence, the fixed boundary length of $L = 3.2$ m is valid in the profile (III) and (IV).

From the above reasons, the AIC mode is expected to be excited as the eigen mode determined by the axial boundary. The boundary length of the AIC mode depends on the axial extension of the hot ions. The reflection will be caused by the mismatching of the wave number which are caused by the spatial variation of the AIC driving term.

4.4 Pressure Anisotropy Relaxation due to AIC Instability

Relaxation of the pressure anisotropy is predicted by the quasi-linear theory⁶⁾, computer simulation⁹⁾ and so on. The first experimental observation of the pressure anisotropy relaxation due to the AIC instability is presented in this section⁴³⁾. Figure 4.20 shows

the time evolution of the observed signals which indicate the relaxation of the pressure anisotropy; (a) the diamagnetic signals of the midplane loop and the second loop (b) the signals of the SEDs in the direction of pitch angles of 90 and 45 degrees at the midplane. (c) the signal of 5.1 keV ion flux escaping from the mirror end, and (d) the amplitude of the AIC mode. During the relaxation period, the density measured by the radially-scannable microwave interferometer is almost $2 \times 10^{18} \text{ m}^{-3}$. The ion temperature obtained from the midplane diamagnetic signal is above 1 keV and is increasing. Relaxation due to Coulomb collisions cannot be expected because the ion-ion collision time is of the order of 10 msec and becomes longer as the ion temperature becomes higher. The SED signal due to photons in this period is relatively small based on the measurements of the TOF analyzer. The increasing rate of the signal SED(90) for charge-exchange neutral with the pitch angle of 90 degrees decreases due to the onset of the mode, while the signal SED(45) for neutrals with the pitch angle of 45 degrees increases continuously. In this period the increasing rate of the diamagnetic signal near the midplane becomes slightly smaller and the diamagnetic signal off midplane maintains its increasing rate. These two phenomena suggest the relaxation of the pressure anisotropy. The ratio of the signal SED(45) to the signal SED(90) is also shown in Fig.4.20b. The time evolution of the amplitude of the AIC mode is shown in Fig.4.20d which is obtained by using the several plasma discharges. Figure 4.20c is the time evolution in the end-loss ions with the pitch angle near the loss cone boundary. The time evolution of the end-loss ion flux resembles that of the excited mode. The increase of the end-loss ion flux corresponds to the reduction of SED(90),

which is clearly related to the onset of the AIC mode.

A small Faraday cup (FC) is used to investigate effect of the AIC mode during the relaxation period. The FC is inserted in the peripheral region of the midplane to measure the flux of ions with the same pitch angle as the angle between the magnetic field line and the FC orientation. Figure 4.21a shows the ratio of the ion flux at the end to the beginning points the relaxation period as a function of the pitch angle. The ratio decreases toward 90 degrees and becomes less than unity at 70 degrees. Figure 4.21b shows the pitch angle dependence of the ion flux normalized to the ion flux with pitch angle of 90 degrees, where solid and open circles represent the data at the beginning point and the end of the relaxation period, respectively. The beginning point means the point at which the increasing rate of the signal begins to decrease and the end point means the point at which the decrease stops. This confirms the relaxation of the pressure anisotropy suggested by the SED measurement.

Chapter 5

Pressure Anisotropy Effects on Micro- and Macroscopic Stabilities

5.1 Suppression of AIC mode

by Control of Pressure Anisotropy

The double-half turn antennas which are installed in the central cell are usually driven by a frequency of 6.2 MHz in the standard operation. As described in the previous chapter, the AIC mode excited in the central cell of the tandem mirror causes a pitch angle scattering of the mirror trapped ions into the loss-cone region. The dispersion relation of the AIC-

mode with a confinement potential is theoretically solved³⁶⁾. In the velocity space, ions confined by the potential contribute to the relaxation of the pressure anisotropy and the AIC mode will be suppressed. Recently, experiments in a plasma with a higher density and higher temperature have been initiated. The suppression experiments of the AIC mode by the formation of the confining potential will be performed in near future. In the present heating experiment, the reduction of the pressure anisotropy with second ICRF pulse has been tested in order to suppress the AIC-mode⁴⁴⁾. Another resonance layer is located off-midplane in addition to the midplane resonance layer. Because the magnetic field profile of the GAMMA 10 is nearly flat near the midplane, the location of the resonance layer for the second ICRF pulse of which frequency is slightly higher than that of the midplane resonance frequency is apart about 1 m from the midplane. Figure 5.1a shows the pressure anisotropy of the central cell determined with the diamagnetic loop. It is clearly shown that the pressure anisotropy in the case of two frequencies is relaxed in comparison with the case of only the midplane resonance. The integrated intensity of the AIC mode is suppressed in the case of two frequencies as shown in Fig.5.1b. This suggests the possibility of suppressing the AIC mode even in the future cases where the fluctuation level becomes high enough to affect the plasma confinement.

5.2 Pressure Anisotropy Effect on of Flute-Interchange Mode

5.2.1 Stability Theory of Flute-Interchange Mode

A flute-interchange mode is driven by the plasma pressure weighting on the bad curvature region. The stability is determined by integrating the product of the total pressure and the normal curvature along the magnetic field line divided by the magnetic field strength as follows :

$$\Gamma = \int \frac{(P_{\perp} + P_{\parallel}) \kappa_{\varphi}}{B} dl \geq 0. \quad 5.1$$

Equation 5.1 is estimated by substituting the pressure profile which is estimated as described in the section 3.2 for $P_{\perp} + P_{\parallel}$. Solid line shows a typical pressure profile a dotted line the magnetic field strength, a thin solid line the normal curvature κ_{φ} and a thin dotted line the integrand in Eq.5.1. When the pressure anisotropy is strong, the pressure profile is more peaked near the midplane of the central cell. It is expected that the flute-interchange stability is influenced by the decrease in the pressure weighting on the bad curvature region. It is obvious that the pressure of the cold component dominates the integration of Eq.5.1 at the transition regions from the central cell to the anchor cells because of the presence of large bad curvature. Estimation of Γ is made as follows ; The pressure profile is given by Eq.3.9 and the integration of Eq.5.1 is the summing up to the

pressure weighting of the hot component in the central and anchor cell as well as the cold component which consists of potentially trapped ions in the whole flux tube. By using relation $P_{\perp} + P_{\parallel} = P_{\perp}(1 + P_{\parallel}/P_{\perp})$, Eq.5.1 reduces to

$$\Gamma = \Gamma_C P_{\perp C}^h + \Gamma_A P_{\perp A}^h + \Gamma_{Cold} P_{\perp}^c. \quad 5.2$$

where Γ_C, Γ_A and Γ_{Cold} are components of the hot ions in the central cell, in the anchor cell, and the cold ions respectively. Γ_C and Γ_A are functions of each pressure anisotropy in the central and anchor cells in Figs.5.3a and 5.3b. Figure 5.3c shows that Γ_{Cold} is determined locally as a function of the plasma length along the magnetic field line. $P_{\perp C}^h$ is a pressure of the hot ions at the midplane of the central cell, $P_{\perp A}^h$ at the midplane of the anchor-cell and P_{\perp}^c the pressure of the cold component. It is useful to rearrange Eq.5.1 with respect to the perpendicular pressure components, because we measure the perpendicular pressure profile by use of the diamagnetic loop array. We set $\Gamma = 0$ in order to obtain the stability threshold as a function of ratios of the central beta to anchor beta and the pressure anisotropy. We obtain the following equations by rearranging Eq.5.2 and $\Gamma = 0$

$$\frac{\beta_{\perp C}}{\beta_{\perp A}} = \frac{\beta_{\perp C}^h + \beta_{\perp C}^c}{\beta_{\perp A}^h + \beta_{\perp A}^c} = \zeta \times \frac{1}{\Gamma_C} + \xi \quad 5.3$$

$$\zeta = (\Gamma_A - \Gamma_{Cold}) \alpha B_R - \Gamma_A B_R \quad 5.4$$

$$\xi = \alpha B_R = \frac{\beta_{\perp C}^c}{\beta_{\perp A}^c} \quad 5.5$$

$$\left(\alpha = \frac{\beta_{\perp A}^c}{\beta_{\perp A}} \quad B_R = \frac{B_A^2}{B_C^2} = 2.27 \right) \quad \text{in standard operation.}$$

Reciprocal of the integration Γ_C is approximately described as a linear function of the pressure anisotropy of the central cell as follows :

$$\frac{1}{\Gamma_C} = -0.148 \times \frac{P_{\perp C}^h}{P_{\parallel C}^h} \quad 5.6$$

From Eqs.5.3 and 5.6, we obtain the following relation

$$\frac{\beta_{\perp C}}{\beta_{\perp A}} = -0.148 \times \zeta \times \frac{P_{\perp C}^h}{P_{\parallel C}^h} + \xi. \quad 5.7$$

Eq.5.7 shows the pressure anisotropy dependence of the critical beta ratio. It is necessary to obtain parameters of the pressure anisotropy and the ratio of the cold component to the hot component in the anchor cell in Eq.5.7. Here, we assume reasonably that the pressure anisotropy of the anchor cell lies within $P_{\perp A}/P_{\parallel A} = 5 \sim 10$, then the minimum of Γ_A is 6 in Fig.5.3b. Figure 5.4 shows the theoretically-predicted critical beta ratio with a parameter of α which indicates contribution of the cold component. The anisotropy dependence of the critical beta ratio strong function of the parameter α .

5.2.2 Experimental Results and Discussion

The stability boundary of GAMMA 10 for the flute interchange modes is experimentally obtained. Additional gas puffing into the anchor cell enhances the charge-exchange loss and reduces the anchor beta. Modulation of the ICRF heating power is successfully used to vary the beta values at anchor (β_{LA}) and central cells (β_{LC}) in a wide range. When the ratio of the central beta to the anchor beta reaches a critical value, the central beta abruptly dump and the plasma is terminated associated with violent density fluctuations. In Fig.5.5 the experimentally obtained data are plotted on β_{LC} - β_{LA} diagram. The central-cell plasmas can not be maintained stably in the region of the low anchor beta. The stability boundary corresponds to agree well with the threshold predicted by the flute-interchange instability theory including the effect of the pressure anisotropy of the central-cell plasma.

Figure 5.6 shows a temporal evolution of the central- and anchor-cell pressure. When the additional gas is puffed into the anchor cell, the anchor-cell pressure decreases because of an increase of the charge exchange energy loss. When the beta ratio reaches a critical value, the central-cell pressure abruptly dumps. It is found that the MHD stability is determined by the ratio of the central-cell beta value β_{LC} to the anchor-cell beta value β_{LA} .

Low-frequency fluctuations on ion saturation currents are detected as shown in Fig.5.7 by 8 electrostatic probes which are arrayed on the central-cell limiter and flush with the

limiter edge. As seen in Fig.5.7, the fluctuations have an azimuthal mode number of $m = -1$; propagation in the direction of the ion diamagnetic drift with the phase velocity nearly equal to $E \times B$ rotation velocity. Moreover, the phase difference between a central- and anchor-cell probe signals which are arranged along the field line is quite small. This indicates that an axial wavelength is much longer than the distance of 5.8m between the two probes, that is, parallel wave number $k \sim 0$. These results indicate that the observed low-frequency instability is caused by a flute interchange mode.

In Fig.5.8, the critical beta ratios β_{1C}/β_{1A} are plotted against the pressure anisotropy in the central cell. The solid line is theoretically obtained dependence of the critical beta ratio on the anisotropy of the central cell. The stability boundary of the flute-interchange mode is influenced by the pressure of the cold component which is weighted on the transition region from the central cell to the anchor cell shown in Fig.5.4. Figure 5.9 shows the RF2 net power dependence of (a) the diamagnetism in the central and anchor cells, (b) the pressure anisotropy of the central cell, and (c) the density of $r = 0$ m at the midplane and mirror throat in the central cell. When the radiated power from the RF2 antenna increases the stored energy in the central cell increases and decreases oppositely in the anchor cell. Ions are heated by the wave field which is excited by the RF2 antenna and trapped in the mirror field of the central cell, then, the passing ions to the anchor cell decreases. The density of the central cell is estimated from the radial profile of the line-integrated density, by the Abel inversion. The density of the mirror throat is estimated from the on-axis line density and the profile of the ion saturation current.

The absolute value of the density is evaluated from comparing between the line density and the profile of the ion saturation current. In Fig.5.10, the radial profiles of density are shown at the central cell, inner and outer transition region and mirror throat of the central cell. The pressure in the transition region is estimated from the measurements of the ion saturation current and the small Faraday cup which are installed at the transition region. The density of the inner transition region is three times higher than in the outer transition region at $r = 0$ m. The axial profile of the pressure of the cold component is assumed to be constant in the region between both anchor midplanes. The pressure in the outer region from the anchor midplane is assumed to be $1/3$ times lower than that of the inner region from the measurement of the ion saturation current. The pressures of the anchor and central cells is estimated from the diamagnetic loop signal. We assume that the density profile $n(r)$ is parabolic and the temperature profile $T(r)$ is radially constant. The pressure is defined as the product of $n(0)$ and $T(r) = \bar{T}$. The assumption of the axial profile of the pressure is reasonable by taking into account the measurement shown in Fig.5.10.

The anisotropy dependence of the pressures in the central, anchor and transition regions is shown in Fig.5.11a. From the experimentally-obtained parameters as shown in Fig.5.9, the parameter α is obtained and is shown in Fig.5.11b. The α has only a weak dependence on the pressure anisotropy of the central- cell plasma. The minimum α becomes about 0.1 as seen in Fig.5.11b. By using $\alpha = 0.1$, the theoretical curve of the critical beta ratio is obtained as a function of the pressure anisotropy and corresponds to

the solid line of the critical beta ratio shown in Fig.5.8.

Pressure Anisotropy Effect to AIC and Flute-Interchange Instability

The stability regimes for both the AIC and the flute-interchange modes are shown on $\beta_{\perp C}-P_{\perp}/P_{\parallel}$ diagram as seen in Fig.5.12. Solid lines show the theoretical contour of the constant growth rate of the AIC mode. Dotted lines are the flute stability boundary which is calculated from Eq.5.1. The solid circles indicate the case in which the AIC mode is observed and the open circles no AIC mode. When the amplitude of the AIC mode increase, relaxation of the pressure anisotropy has been observed. In the parameter region including the solid and open circles the plasma is macroscopically stable, which is good agreement with the predicted stable region.

With the increasing beta value, the pressure anisotropy is enhanced, and the increase of the amplitude of the AIC mode suppress the pressure anisotropy. When the beta value is more increasing, the plasma is terminated owing to the limit of the flute-interchange instability. In a future 10 experiments in GAMMA 10, the auxiliary heating to the anchor cell, for example as a neutral beam injection, may be needed for the avoidance of the flute-interchange limit assisted by the AIC mode.

Chapter 6

Conclusion

1. The pressure anisotropy is quantitatively obtained by using the diamagnetic loop array, the secondary electron detector and the small Faraday cup.
2. The fluctuations which depends on both the ion pressure and the pressure anisotropy are identified as an Alfvén ion cyclotron (AIC) mode.
 - (a) The fluctuations have discrete frequency spectra in the range slightly below the ion cyclotron frequency at the midplane of the central cell.
 - (b) The azimuthal mode number of the fluctuations is low m number of -1 or -2 which propagate to the direction of ion diamagnetic drift.
 - (c) The radial profile of the fluctuation amplitude is peaked at the core region of the plasma.
 - (d) The left-handed circular polarization is dominant in the core region, while, the

right-handed circular polarization is dominant at the edge region.

- (e) The fluctuations take the standing wave structure in the axial finite extension and propagate in the outer region. The standing wave region is expanded depending on the AIC driving term.

Because the characteristics of the fluctuations agree well with the theoretical prediction of the AIC mode, we identify the fluctuations as the AIC mode.

3. A new theory of the AIC mode is developed including effect of the of the axial finite extension and compared with the experimental results. The theory predicts well the observed fine structure of the frequency spectra of the AIC mode; the frequency gets higher and the difference between the frequency spectral peaks become narrower with the increase of the AIC driving term. The absolutely unstable region is enhanced by the finite length effects.
4. The relaxation of the pressure anisotropy is experimentally observed by using the diamagnetic loop array, the small Faraday cup and the SED array.
5. The pressure anisotropy is controlled by the supplement of the additional RF-heating power which is absorbed at the off-midplane resonance layer. It is demonstrated experimentally that the suppression of the AIC mode is possible by the control of the pressure anisotropy.
6. The stability boundary for the flute-interchange mode are experimentally obtained

and is in good agreement with the theoretical prediction. The ratio of the central cell β_{LC} to the anchor cell β_{LA} determines the MHD stability. By the decrement in the pressure weighting on the bad curvature region, the stable region greatly expands on β_{LC} and β_{LA} diagram.

Acknowledgements

The author acknowledges all members of GSI/ASMA II group for carrying out the experiments and for helpful suggestions. He acknowledges Prof. T. Ishihara and Prof. T. A. of the Institute of Applied Physics, Univ. of Tsukuba and Prof. T. Demery, director of the Plasma Physics Center for their continuous encouragement. He is very grateful to Assoc. Prof. M. Hoshino and Dr. H. Ishizawa for significant discussions and suggestions on experiments and computer. He wishes to thank Assoc. Prof. A. Miki and Y. Yamamoto for discussion on experimental results. He is also much grateful to Prof. K. Yano and Assoc. Prof. T. Hasegawa and Kubota for their suggestions. He also acknowledges Dr. Chikazumi for allowing the author to use his computational code. He acknowledges Assoc. Prof. T. Watanabe of the National Institute for Fusion Science for useful discussions about the numerical results of the AIC mode.

The calculations of the magnetic flux and the diagnostic relation of the AIC mode were performed by using the computer system of the Computer Center of the National Institute for Fusion Science.

This work was partly supported by Grants-in-Aid for Scientific Research from the Min.

Acknowledgements

The author acknowledges all members of GAMMA 10 group of carrying out the experiments and for helpful suggestions. He acknowledges Prof. T.Ishihara and Prof. T.Arai of the Institute of Applied Physics, Univ. of Tsukuba and Prof. T.Tamano, director of the Plasma Research Center for their continuous encouragement. He is very grateful to Assoc. Prof. M.Inutake and Dr. M.Ichimura for significant discussions and suggestions on experiments and diagnostics. He wishes to thank Assoc. Profs. A.Mase and Y.Kiwamoto for discussion on experimental results. He is also much grateful to Prof. K.Yatsu and Assoc. Profs. H.Hojo and K.Ishii for their suggestions. He also acknowledges Dr. I.Katanuma for allowing the author to use his computational code. He acknowledges Assoc. Prof. T.Watanabe of the National Institute for Fusion Science for useful discussion about the theoretical model of the AIC mode.

The computations of the diamagnetic flux and the dispersion relation of the AIC mode were performed by using the computer system at the Computer Center of the National Institute for Fusion Science.

This work was partly supported by Grant-in-aid for Scientific Research from the Min-

istry of Education, Science and Culture.

Appendix A

Other Heating Systems and

Diagnostics

Other Heating System

The heating system consists of a gas burner (NPO) and a heat exchanger (HE) as shown in Fig. A.1. The burner, which is made of stainless steel, has the outer diameter of 70 mm and the inner diameter of 20 mm. The catalyst, which is made of alumina, has the outer diameter of 18 mm. There are two kinds of insulation, which are made of silica wool (SW) and glass wool (GW), between the burner and the catalyst. A pilot burner, which is made of stainless steel and has the outer diameter of 20 mm, is added between the burner and the HE exchanger for obtaining a reliable detection of a leak of gas flow rate without requiring any special technique. Maximum flow rate

Appendix A

Other Heating Systems and Diagnostics

Other Heating System

Magneto-plasma-dynamic (MPD) guns are installed at both ends of GAMMA 10. The gun has a coaxial electrode as shown in Fig.A.1. The anode, which is made of molybdenum, has the outer diameter of 70 mm and the inner diameter of 30 mm. The cathode, which is made of tungsten, has the outer diameter of 10 mm. There are two kinds of insulators, which are made of boron nitride (BN) and glass ceramic (MACOR), between the anode and the cathode. A pilot anode, which is made of molybdenum and has the inner diameter of 20 mm, is added between the anode and the BN insulator for obtaining a reliable discharge at a reduced gas flow rate without employing any trigger electrode. Maximum charging

voltage on the pulse forming network (PFN) is 1 kV. Typical discharge voltage and current are about 200 V and 10 kA, respectively. Hydrogen gas is injected quasisteadily during the discharge by use of a fast-acting electromagnetic valve (FAV) in order to minimize excessive gas before and after the discharge. The gas pulse-width is adjustable by changing the spring strength in this valve. In the present experiments the pulse width of 1 ms in a steady gas flow rate is selected. The gas flow rate at the reservoir pressure of 1 atm hydrogen is 150 torr·ℓ/s. Short-pulse (1 ms) gun-produced plasmas are injected into the central cell along the magnetic field line. The gun-produced plasma is very effective for building up the plasma in combination with ICRF power and a small quantity of central-cell gas puffing.

The electron cyclotron resonance heating (ECRH) system consists of four gyrotrons with the frequency of 28 GHz and the maximum output power of 160 kW. At the plug/barrier cells, the fundamental ECRH ($\omega = \Omega_{ce}$) is carried out to form the ion confining potential by producing warm electrons, and the second harmonic ECRH ($\omega = 2\Omega_{ce}$) is carried out to deep the thermal barrier potential by producing mirror-trapped hot electron.

Neutral Beam Injection (NBI) system is installed in the plug/barrier cells. Neutral beams of 23 kV acceleration voltage and 60 A drain current are injected near the midplane of the plug/barrier cell at the angle of 40° in order to produce sloshing ions for the effective ion confining potential.

Other Diagnostics

The electron line densities are measured by six microwave interferometers (wave length = 4 mm) at central cell, west anchor, east/west barrier, east plug cells and the central transition in one shot. Scanning microwave interferometers are employed for the measurements of the radial density profile at the central cell and the barrier cell.

The radial profile of the end loss ions are measured by a movable end loss analyzer (mov. ELA). The ELA is a multi-grid type electrostatic energy analyzer. It is scannable in the x-direction and is installed between the outer mirror throat of the end mirror cell and the end plate. Fixed ELA's with the same structure as the mov. ELA are located behind the end plate.

The plasma potentials at the midplane of the east barrier cell and the central cell are diagnosed by neutral Au-beam probes. An energy resolution is no more than 50 V and a time resolution is 200 μ sec.

Appendix B

Dispersion Relation of AIC mode

We start the Maxwell and collisionless Boltzmann equations.

$$\frac{\partial f_j}{\partial t} + \mathbf{v} \cdot \frac{\partial f_j}{\partial \mathbf{r}} + \frac{q_j}{m_j} [\mathbf{E} + \mathbf{v} \times \mathbf{B}] \cdot \frac{\partial f_j}{\partial \mathbf{v}} = 0 \quad \text{B.1}$$

$$\nabla \cdot \mathbf{E} = \sum_{j=e,i} q_j n_j \quad \text{B.2}$$

$$\nabla \times \mathbf{E} = -\frac{\partial \mathbf{B}}{\partial t} \quad \text{B.3}$$

$$\nabla \cdot \mathbf{B} = 0 \quad \text{B.4}$$

$$\nabla \times \mathbf{B} = \mu_0 \frac{\partial \mathbf{D}}{\partial t} \quad \text{B.5}$$

$$\mathbf{D} = \epsilon_0 \mathbf{K} \cdot \mathbf{E} \quad \text{B.6}$$

$$\mathbf{j} = \sigma \cdot \mathbf{E} \quad \text{B.7}$$

Here, the j -particle charge is q_j , the mass m_j , the density n_j , the distribution function f_j , the electric field \mathbf{E} , the magnetic flux \mathbf{B} , the electric displacement vector \mathbf{D} , the current density \mathbf{j} , the conductivity σ , the dielectric tensor \mathbf{K} and the effective dielectric permittivity tensor ϵ . ϵ_0 and μ_0 are the permittivity and the permeability of free space, respectively. Owing to linearizing the Eqs.B.1-B.7, the wave equations for the AIC modes can be obtained in the form

$$\mathbf{k} \times (\mathbf{k} \times \tilde{\mathbf{E}}) = -\frac{\omega^2}{c^2} \mathbf{K} \cdot \tilde{\mathbf{E}}. \quad \text{B.8}$$

Here, \mathbf{k} is a wave number, a one-ordered perturbation of the electric field $\tilde{\mathbf{E}}$, an angular frequency ω and the light speed c . \mathbf{K} is a dielectric tensor for the hot plasma as follows :

$$\begin{aligned} K_{xx} &= 1 - \sum_{j=e,i} \frac{\Omega_{pj}^2}{2} (\chi_{j+} + \chi_{j-}) \\ K_{xy} &= - \sum_{j=e,i} \frac{i\Omega_{pj}^2}{2} (\chi_{j+} - \chi_{j-}) \\ K_{yx} &= - \sum_{j=e,i} \frac{i\Omega_{pj}^2}{2} (\chi_{j+} + \chi_{j-}) \\ K_{yy} &= 1 - \sum_{j=e,i} \frac{\Omega_{pj}^2}{2} (\chi_{j+} + \chi_{j-}) \\ K_{zz} &= 1 + \sum_{j=e,i} \int_{-\infty}^{\infty} dv_{\parallel} \int_0^{\infty} dv_{\perp} \frac{2\pi\Omega_{pj}^2}{\omega} \frac{df}{dv_{\parallel}} v_{\parallel} v_{\perp} \\ K_{xz} &= K_{yz} = K_{zx} = K_{zy} = 0 \end{aligned}$$

$$\text{where } \mathbf{K} = \begin{pmatrix} K_{xx} & K_{xy} & K_{xz} \\ K_{yx} & K_{yy} & K_{yz} \\ K_{zx} & K_{zy} & K_{zz} \end{pmatrix} \quad \text{B.9}$$

Ω_{pj} and Ω_{cj} are the plasma frequency and the cyclotron frequency, respectively. When the parallel propagation is assumed for the AIC mode, susceptibility χ_{j+} and χ_{j-} is evaluated from the moment integration of the distribution function of the ion and the electron.

$$\chi_{j\pm} = \int_{-\infty}^{\infty} dv_{\parallel} \int_0^{\infty} dv_{\perp} \frac{\pi v_{\perp}^2 \left[(kv_{\parallel} - \omega) \frac{df}{dv_{\perp}} - kv_{\perp} \frac{df}{dv_{\parallel}} \right]}{\omega - kv_{\parallel} \mp \delta_j \Omega_{pj}} \quad \text{B.10}$$

When the condition of $\det\left[\frac{k^2 c^2}{\omega^2}(\mathbf{I} - \mathbf{e}_z \mathbf{e}_z) - \mathbf{K}\right] = 0$ is satisfied, the wave equations have a nontrivial solution. The explicit expression is given by

$$\begin{aligned} & \left(1 - \frac{k^2 c^2}{\omega^2} - \sum_{j=e,i} \frac{\Omega_{pj}^2}{\omega^2} \chi_{j+}\right) \left(1 - \frac{k^2 c^2}{\omega^2} - \sum_{j=e,i} \frac{\Omega_{pj}^2}{\omega^2} \chi_{j-}\right) \\ & \times \left(1 + \sum_{j=e,i} \int_{-\infty}^{\infty} dv_{\parallel} \int_0^{\infty} dv_{\perp} \frac{2\pi \Omega_{pj}^2}{\omega} \frac{\frac{df}{dv_{\parallel}}}{\omega - kv_{\parallel}} v_{\parallel} v_{\perp}\right) = 0. \quad \text{B.11} \end{aligned}$$

The AIC mode is excited due to the ion anisotropic distribution, and hence, the dispersion relation of the AIC mode is given by

$$\omega^2 - k^2 c^2 - \sum_{j=e,i} \Omega_{pj}^2 \chi_{j+} = 0. \quad \text{B.12}$$

Hereafter, the subscript of $+$ is omitted. Under the condition of $T_e \approx 0$ the electron term is

$$\chi_e = \frac{\omega}{\Omega_{ce} - \omega} \approx \frac{\omega}{\Omega_{ce}}. \quad \text{B.13}$$

The distribution function of ions is assumed as the anisotropic distribution function described as follows :

$$f(v_{\perp}, v_{\parallel}) = CH(w)w \exp(-\alpha v_{\perp}^2 - \alpha_{\parallel} v_{\parallel}^2). \quad \text{B.14}$$

Then ion term is as follows :

$$\chi_i = \chi_{i0} + \Delta\chi_i \quad \text{B.15}$$

$$\begin{aligned} \chi_{i0} &= \frac{\omega}{\omega - \Omega_{ci}} - A \frac{1}{R-1} Z_3(\xi) \\ &\quad - A \left[\frac{\Omega_{ci}}{\omega - \Omega_{ci}} + \frac{2}{\tau} + \frac{1}{R-1} - \frac{\varphi}{R-1} \left(1 + \frac{\tau}{R-1} \right) \right] Z_1(\xi) \\ \Delta\chi_i &= \pi \int_{-v_0}^{v_0} dv_{\parallel} \frac{C}{\alpha^2} e^{-\alpha_{\parallel} v_{\parallel}^2} \left\{ \frac{\frac{k^2}{\alpha}}{(\omega - \Omega_{ci} - kv_{\parallel})^2} \left[1 - e^{-\alpha\sigma} - \frac{\alpha\sigma}{2} (1 + e^{-\alpha\sigma}) \right] \right. \\ &\quad \left. + \frac{\Omega_{ci}}{\omega - \Omega_{ci}} \frac{kv_{\parallel}}{\omega - \Omega_{ci} - kv_{\parallel}} (1 - e^{-\alpha\sigma} - \alpha\sigma) \right\} \quad \left(\sigma \equiv \frac{v_{\parallel}^2 - v_0^2}{R-1} \right) \end{aligned}$$

C is a normalized constant $C = \alpha_p^{1/2} \alpha^{m+1} e^{\alpha v_h^2} / \pi^{2m+3}$. φ defines the plasma potential $\varphi = \alpha_{\parallel} v_0^2$. τ defines the pressure anisotropy $\tau = \alpha / \alpha_{\parallel}$. A is a constant $A = \sqrt{\pi \alpha_{\parallel} / \alpha_p} / (2I_1)$.

The perpendicular velocity v_{\perp} is transformed to w which is defined as $w = v_{\perp}^2 - (v_{\parallel}^2 - v_0^2)/(R-1)$. The loss boundary is defined as $v_{\parallel}^2 = (R-1)v_{\perp}^2 + v_0^2$. α is defined as $\alpha_p = \alpha_{\parallel} + \alpha/(R-1) = M/(2T_{\parallel})$. Z is the plasma dispersion function. The argument of the plasma dispersion function is defined as $\xi = ((\omega - \Omega_{ci}) \alpha_p^{1/2})/k$ and $\xi_1 = \xi / (\sqrt{1 + \tau/(R-1)})$. $H(w)$ is the Heaviside's step function. The notation "I" indicates the integration defined as follows :

$$I_1(\varphi, \tau, R) = \int_0^{\sqrt{\varphi}} dt e^{-t^2} (1 - \rho) + \int_{\sqrt{\varphi}}^{\infty} dt e^{-t^2 - \rho} \quad \text{B.16}$$

$$I_2(\varphi, \tau, R) = \int_0^{\sqrt{\varphi}} dt e^{-t^2} \left(1 - \frac{\rho}{2}\right) + \int_{\sqrt{\varphi}}^{\infty} dt e^{-t^2 - \rho} \left(1 + \frac{\rho}{2}\right) \quad \text{B.17}$$

$$I_3(\varphi, \tau, R) = \int_0^{\sqrt{\varphi}} dt t^2 e^{-t^2} (1 - \rho) + \int_{\sqrt{\varphi}}^{\infty} dt t^2 e^{-t^2 - \rho} \quad \text{B.18}$$

$$\left(\rho \equiv \tau \frac{t^2 - \varphi}{R - 1}\right)$$

The pressure anisotropy is determined as follows :

$$\frac{P_{\perp}}{P_{\parallel}} = \frac{1}{\tau} \frac{I_2}{I_3} \quad \text{B.19}$$

Appendix C

Absolute and Convective

Instabilities

In order to determine the stability of a system, we consider a point source with respect to the coordinate z , which starts at $t = 0$. The stability of the system can be obtained from studying the responses to the point source^{40,41}. The source function is given as follows :

$$g(z, t) = \begin{cases} 0 & \text{for } t < 0 \\ \text{constant} \times \delta(z) e^{-i\omega_0 t} & \text{for } t > 0 \end{cases} \quad \text{C.1}$$

Here, δ is the Dirac delta function. The system response is defined as ψ

$$\psi_{k\omega} = \frac{g_{k\omega}}{D(k, \omega)} \quad \text{C.2}$$

We execute the Fourier transform for the source function of Eq.C.1 so that

$$g_{k\omega} = \frac{\text{constant}}{i(\omega - \omega_0)}. \quad \text{C.3}$$

The response function $\psi(z, t)$ is then found from the inversion formula

$$\psi = \text{constant} \times \int_{-\infty+i\sigma}^{\infty+i\sigma} \Phi(z, \omega) \frac{e^{-i\omega t}}{i(\omega - \omega_0)} \frac{d\omega}{2\pi} \quad \text{C.4}$$

$$\Phi(z, \omega) = \int_{-\infty}^{\infty} \frac{e^{ikz}}{D(k, \omega)} dk \quad \text{C.5}$$

This expression necessarily satisfies the equations $\psi(z, t) = 0$ for $t < 0$ in accordance with the condition of the problem: the perturbation occurs only after the source comes in at $t = 0$. In order to find the asymptotic expression for $\psi(z, t)$ far from the source $|z| \rightarrow \infty$ in a steady condition, the source begins to operate $t \rightarrow \infty$. To find the required asymptotic form, we note, first of all, that the asymptotic limit $t \rightarrow \infty$ must be taken before $|z| \rightarrow \infty$. Since the perturbation cannot propagate to infinity in a finite time, $\psi \rightarrow 0$ as $|z| \rightarrow \infty$ for a finite t .

We move the contour of integration with respect to ω in Eq.C.4 downwards in order to get the asymptotic expression as $t \rightarrow \infty$. Since the system is convectively unstable, $\Phi(z, \omega)$ has no singularity in the upper half-plane of ω , and the highest singularity of the integrand in Eq.C.4 is the pole $\omega = \omega_0$ on the real axis. It is discussed in the later paragraph for the case of $\Phi(z, \omega)$ which has a singularity in the upper half-plane of ω .

Hence, the asymptotic form as $t \rightarrow \infty$ for the convectively unstable case is

$$\psi(z, t) \propto e^{-i\omega_0 t} \Phi(z, \omega_0). \quad \text{C.6}$$

To find an asymptotic form of $\Phi(z, \omega_0)$ as $|z| \rightarrow \infty$, we must now move the path of integration with respect to k upwards for $z > 0$ or downwards for $z < 0$, until it catches the pole of the integrand in Eq.C.5, i.e. the root of the equation $D(k, \omega_0) = 0$.

$k_+(\omega)$ and $k_-(\omega)$ are defined as the poles which are respectively in the upper and lower half-planes of k as $\omega_i \rightarrow \infty$. As ω_i decreases, the pole move, and for a real $\omega = \omega_0$ they may either remain in their original half-plane or enter the other half-plane. In the first case, the contour of integration in $\Phi(z, \omega_0)$ remains on the real axis as in Fig.C.1a; in the second case, it is deformed as shown in Fig.C.1b, so as to embrace the pole $k_+(\omega_0)$ and $k_-(\omega_0)$ (point A and C) that have escaped into the other half-plane. In the either case, when the contour is moved up or down, it catches on the pole k_+ and k_- , respectively. The asymptotic form of $\psi(z, t)$ as $z \rightarrow +\infty$ is determined by the contribution from the lowest pole $k_+(\omega_0)$; that is determined by the highest pole $k_-(\omega_0)$ as $z \rightarrow -\infty$. The pole concerned is thus the closest to the real axis, or the farthest from the real axis among those which have moved into the other half-plane. With these values of k_+ and k_- , we

have

$$\psi(z, t) \propto \begin{cases} \exp[i(k_+(\omega_0)z - \omega_0 t)] & \text{for } z > 0 \\ \exp[i(k_-(\omega_0)z - \omega_0 t)] & \text{for } z < 0. \end{cases} \quad \text{C.7}$$

For a stable system, all poles remain in their original half-plane when $\omega = \omega_0$, since the absence of oscillation branches with $\omega_i(k) > 0$ (for real k) means that a pole $k(\omega)$ can cross the real axis only with $\omega_i < 0$. Hence, in Eq.C.7 $k_{+i}(\omega_0) > 0$, $k_{-i}(\omega_0) < 0$ so that the waves dump in both directions from the source.

In the case of the convective instability, the poles $k(\omega)$ reach the real axis with $\omega_i > 0$. There are therefore certainly poles k_+ and k_- which have entered the other half-plane for $\omega = \omega_0$, i.e. which have $k_{+i}(\omega_0) < 0$ or $k_{-i}(\omega_0) > 0$. The presence of such a pole $k_+(\omega_0)$ or $k_-(\omega_0)$ amplified the wave to the right or left of the source, respectively.

In the case of the absolute instability, the integration of Eq.C.4 is modified owing to the singularity of $\Phi(z, \omega_c)$ for $\omega = \omega_c$. The asymptotic value of the integral is determined by the neighbourhood of that point, so that

$$\psi(z, t) \propto \exp(-i\omega_c t) = \exp(-i\omega_{cr} t + \omega_{ci} t). \quad \text{C.8}$$

If $\omega_{ci} > 0$, the perturbation increases at any fixed point z ; i.e. the instability is absolute, but if $\omega_{ci} < 0$ the perturbation tends to zero at a fixed point, i.e. the instability is convective.

In Fig.C.2, the contour plot of $D(k, \omega)$ in the complex k plane for the AIC mode is drawn in the case of (a) the absolute and (b) convective instability. The trajectory of the roots of the dispersion relation is described as the white lines for the ω_0 of 0.76, 0.80, 0.84 and 0.88. The imaginary part of ω is moved from 0 to $[\omega_i/\Omega_{ci}]_{MAX}$ which is defined in Fig.4.6. The singularity of $\Phi(z, \omega_0)$ is caused by the double root of the dispersion relation $D(k, \omega) = 0$, which is shown as a saddle point in Fig.C.2a. in the velocity space due to the electric or magnetic fluctuations.

References

- 1) R.F.Post : Nucl. Fusion **27** (1987) 1579.
- 2) M.Inutake, T.Tamano, T.Cho, M.Hirata, H.Hojo, M.Ichimura, K.Ishii, A.Itakura, I.Katanuma, Y.Kiwamoto, A.Mase, S.Miyoshi, Y.Nagayama, Y.Nakashima, T.Saito, Y.Tatematsu, N.Yamaguchi, and K.Yatsu :
14th Int. Conf. on Plasma Phys. and Controlled Nucl. Fusion Research
1992 (Würzburg,1992) IAEA-CN-56/C-4-7.
- 3) M.Inutake, T.Cho, M.Ichimura, K.Ishii, A.Itakura, I.Katanuma, Y.Kiwamoto, Y.Kusama, A.Mase, S.Miyoshi, Y.Nakashima, T.Saito, A.Sakasai, K.Sawada, I.Wakaida, N.Yamaguchi, and K.Yatsu : Phys. Rev. Lett. **55** (1985) 939.
- 4) S.Adachi Ph.D. Thesis Tsukuba Univ. (1989).
- 5) G.R.Smith : Phys. Fluids **27** (1984) 1499.
- 6) R.C.Davidson, Joan M. Ogden : Phys. Fluids **18** (1975) 1045.
- 7) A.Iiyoshi, H.Yamamoto, and S.Yoshikawa : Phys. Fluids **10** (1967) 749.

- 8) M.Tanaka : J. Geophys. Res. **90** (1985) 6459.
- 9) T.Tajima and J.M.Dawson : Nucl. Fusion **20** (1980) 1129.
- 10) T.A.Casper and G.R.Smith : Phys. Rev. Lett. **48** (1982) 1015.
- 11) G.R.Smith, T.A.Casper, and M.J.Gerver : Nucl. Fusion **23** (1983) 1381.
- 12) S.N.Golovato, K.Brau, J.Casey, M.J.Gerver, S.Horne, J.Irby, J.Kesner, B.Lane, J.Machuzak, R.Myer, R.S.Post, E.Sevillano, and L.Wang :
Phys. Fluids B **1** (1989) 851.
- 13) R.Katsumata, M.Inutake, M.Ichimura, A.Ishihara, A.Mase, Y.Nakashima, K.Ishii, H.Hojo, I.Katanuma, and T.Tamano : 20th EPS Conf. on Controlled Fusion and Plasma Phys. Lisboa 26-30 July 1993 Vol.2 545.
- 14) R.Katsumata et al. to be submitted.
- 15) G.R.Smith, William McCay Nevins, and William M. Sharp :
Phys. Fluids **27** (1984) 2120.
- 16) A.Mase, M.Ichimura, H.Satake, R.Katsumata, T.Tokuzawa, Y.Ito, H.Hojo, E.J.Doyle, A.Itakura, M.Inutake, and T.Tamano : Phys. Fluids B **5** (1993) 1677.
- 17) H.Hojo, A.Mase, R.Katsumata, M.Inutake, A.Itakura, and M.Ichimura : Jpn. J. Appl. Phys. **32** (1993) 3287.

- 18) K.L.Wong, R.J.Fonck, S.F.Paul, D.R.Roberts, E.D.Fredrickson, R.Nasikian, H.K.Park, M.Bell, N.L.Bretz, R.Budny, S.Cohen, G.W.Hammett, F.C.Jobes, D.M.Meade, S.S.Medley, D.Mueller, Y.Nagayama, D.K.Owens, and E.J.Synakiwski : Phys. Rev. Lett. **66** (1992) 1874.
- 19) M.N.Rosenbluth and P.H.Rutherford : Phys. Rev. Lett. **34** (1975) 1428.
- 20) T.Watari, T.Hatori, R.Kumazawa, S.Hidekuma, T.Aoki, T.Kawamoto, M.Inutake, S.Hiroe, A.Nishizawa, K.Adati, T.Sato, T.Watanabe, H.Obayashi, and K.Takayama : Phys. Fluids **21** (1978) 2076.
- 21) Y.Ohsawa, M.Inutake, T.Tajima, T.Hatori, and T.Kamimura : Phys. Rev. Lett. **43** (1979) 1246.
- 22) T.Watari, K.Adati, T.Aoki, S.Hidekuma, K.Hattori, S.Hiroe, M.Ichimura, T.Kawamoto, R.Kumazawa, Y.Okubo, S.Okamura and T.Sato : Nucl. Fusion **22** (1982) 1359.
- 23) M.Inutake, M.Ichimura, H.Hojo, Y.Kimura, R.Katsumata, S.Adachi, Y.Nakashima, A.Itakura, A.Mase, and S.Miyoshi : Phys. Rev. Lett. **65** (1990) 3397.
- 24) M.Ichimura, M.Inutake, S.Adachi, D.Sato, F.Tsuboi, Y.Nakashima, I.Katanuma, A.Itakura, A.Mase and S.Miyoshi : Nucl. Fusion **28** (1988) 799.
- 25) M.Ichimura, M.Inutake, E.Asari, S.Adachi, R.Katsumata, Y.Kimura and S.Miyoshi : Jpn. J. Appl. Phys. **30** (1991) 854.

- 26) F.Tsuboi, M.Ichimura, N.Yamaguchi, M.Inutake, S.Adachi, K.Hattori, A.Mase, Y.Nakashima, S.Miyoshi : Rev. Sci. Instrum. **60** (1989) 2868.
- 27) A.I.Kislyakov, J.Stöckel, and K.Jakubka, Sov.Phys.Tech. **20**, (1975) 986.
- 28) R.C.Cross, Introduction to Alfvén Waves : Adam Hilger (1988).
- 29) R.Katsumata, M.Inutake, M.Ichimura, N.Hino, H.Onda, I.Katanuma, H.Hojo, A.Mase and S.Miyoshi : Jpn. J. Appl. Phys. **31** (1992) 2249.
- 30) I.Katanuma, Y.Kiwamoto, T.Saito, N.Yamaguchi and S.Miyoshi : Jpn. J. Appl. Phys. **27** (1988) 159.
- 31) Laurence S.Hall, E.B.Hooper Jr. and W.A.Newcomb : Nucl. Fusion **15** (1975) 875.
- 32) J.Kesner : Nucl. Fusion **25** (1985) 275.
- 33) J.B.Taylor : Phys. Fluids **6** (1963) 1529.
- 34) W.A.Newcomb : J. Plasma Phys. **26** (1981) 529.
- 35) T.Tajima, K.Mima, and J.M.Dawson : Phys. Rev. Lett. **25** (1977) 201.
- 36) H.Hojo, R.Katsumata, M.Ichimura and M.Inutake : J.Phys.Soc.Jpn. (1993) **62**, 3797.
- 37) K.T.Tsang and G.R.Smith : Phys. Fluids **30** (1987) 1362.
- 38) S.K.Ho, William McCay Nevins, Gary R. Smith, and G.H.Miley : Phys. Fluids **31** (1988) 1656.

- 39) R.Hatakeyama, N.Sato, M.Inutake : Nucl. Fusion **23** (1983) 1467.
- 40) E.M.Lifshitz and L.P.Pitaevskii, Physical Kinetics (Pergamon Press, New York, 1981)
p.282.
- 41) R.J.Briggs, Electron-Stream Interaction with plasmas (MIT Press, Cambridge, MA,
1964), Chap.2.
- 42) Karl Heinz, The simplex method ; A probabilistic analysis (Springer-Verlag, Berlin,
1987)
- 43) M.Ichimura, M.Inutake, R.Katsumata, N.Hino, H.Hojo, K.Ishii, T.Tamano
and S.Miyoshi : Phys. Rev. Lett. **70** (1993) 2734.
- 44) M.Ichimura, M.Inutake, R.Katsumata, N.Hino, K.Ishii, T.Cho, M.Hirata,
A.Itakura, I.Katanuma, Y.Kiwamoto, A.Mase, S.Miyoshi, Y.Nakashima, T.Saito,
T.Tamano, N.Yamaguchi and K.Yatsu :
Plasma Phys. and Controlled Nucl. Fusion, **34** (1992) 1889.

Figure Captions

- Fig.2.1 Schematic of GAMMA 10 tandem mirror and axial profile of magnetic field strength.
- Fig.2.2 RF heating systems.
- Fig.2.3 Gas puffing systems.
- Fig.2.4 Diagnostics and axial profile of magnetic field strength.
- Fig.2.5 Schematics of small Faraday cup.
- Fig.2.6 (a) Pitch-angle resolution and (b) pitch angle dependence of ion-collecting efficiency of small Faraday cup are computed.
- Fig.2.7 Anisotropy measurement by using small Faraday cup.
- Fig.2.8 Time-of-Flight-Type (TOF) charge-exchange neutral-particle energy analyzer
- Fig.2.9 (a) Typical law data and energy spectrum of TOF analyzer, (b) temporal evolution of ratio of signal due to photon to charge-exchange neutral particle, (c)

profile of ratio of photon to neutral particle signal is peaked at the center of plasma column. Because the peak value is under 30 %, charge-exchange neutral particle dominates over TOF signal.

Fig.2.10 (a) Schematic of Secondary electron detector (SED) system and (b) measurement of pitch-angle distribution by using SED.

Fig.2.11 Relation between SED signal and pressure anisotropy

Fig.2.12 Design of magnetic probe with protection from fast charge-exchange neutral particles due to SUS cover.

Fig.2.13 Calibration of magnetic probe by use of well-known RF-magnetic field induced by a Helmholtz coil.

Fig.2.14 Typical signal of magnetic probe in calibration. Spatial resolution and sensitivity to oscillating magnetic field are tested. SUS-cover reduce sensitivity of magnetic probe to under 30 %.

Fig.3.1 Schematic of pressure distribution. Pressure distributions perpendicular and parallel to the magnetic field line are indicated by solid and dotted lines for the four types of distribution, respectively. Scale length of L are 2 m, 1.6 m, 1.8 m and the index of n is 50. Broken line is the magnetic field profile of the GAMMA 10 central cell.

Fig.3.2 (a) Relationship between ratio of second loop signal to midplane-loop signal and scale length L and n ; dotted line for pressure distribution of Type A, dashed line for Type B, chain line for Type C and solid line for Type D. (b) Diagram of diamagnetic loop signal ratios for various pressure profiles: dotted line is calculated by computer code for pressure distribution of Type A, dashed line for Type B, chain line for Type C and solid line for Type D.

Diamagnetic fluxes at the midplane, second and third loops are represented by W_1, W_2, W_3 respectively. Closed circles show experimental data, which correspond to data at 55 ms, 56 ms, 60 ms and 61 ms. Error bars for the data are smaller than closed circle radii. Time evolution is expressed by the arrow. From this diagram, time variation of the axial pressure profile can be estimated. (c) Pressure anisotropy versus diamagnetic loop signal ratio. Each line corresponds to the lines in Fig.3.2b. Solid circles are experimental results. From this figure, pressure anisotropy is estimated once after the pressure profile is determined from Fig.3.2b.

Fig.3.3 diamagnetic loop signal ratio of second loop to midplane loop and ratio of third loop to midplane loop is a function of (a) n_C and (b) L_C . A new model of the pressure profile extends the parameter region of ratio of diamagnetic loop signal comparing with Fig.3.2.

Fig.3.4 Anisotropy P_{\perp}/P_{\parallel} is described as a function of L_C and n_C . From Figs.3.3a

and 3.3b, parameters L_C and n_C are evaluated by using experimentally-obtained ratios of diamagnetic loop signal.

Fig.4.1 Physical picture of AIC mode is drawn. Figure 4.1a shows Lorentz force due to magnetic fluctuation for gyrating ion. Arranged discs corresponds with trajectory of ions with velocity of $v_{\perp 0}$. Initial perturbation is growing due to net current induced by tilting motion of ions.

Fig.4.2 Typical time evolution of electron line density (a) and diamagnetic loop signal (b) in the central cell. Midplane loop signal is represented by (○), the second loop signal (×) and the third loop signal (△).

Fig.4.3 RF power dependence of beta value and pressure anisotropy are evaluated by using diamagnetic loop array.

Fig.4.4 Typical frequency spectrum of the magnetic probe signal.

Fig.4.5 (a) Diagram of P_{\perp}/P_{\parallel} versus beta value. Solid circles represent the parameters in which the fluctuations are observed and open circles show no fluctuations. Solid lines are maximum growth rate, $[\omega_i/\Omega_{ci}]_{MAX}$ of 10^{-5} and 10^{-2} . Dotted line is a theoretically-calculated boundary between convective and absolute instability. (b) Fluctuation amplitude depend on AIC driving term which is defined as product between beta and pressure anisotropy.

Fig.4.6 Dispersion relation are derived from Eq.4.10. Maximum growth rate are shown

by a vertical dotted-broken line.

Fig.4.7 Frequency of AIC mode increased with increasing magnetic field strength, and is slightly below ion cyclotron frequency defined at minimum magnetic field strength of central cell.

Fig.4.8 Phase variation at dominant oscillation frequency versus angles between magnetic probes. Observed oscillation has azimuthal mode number of $m = -1$ which propagates in ion diamagnetic drift direction.

Fig.4.9 Amplitudes of fourier spectrum are plotted as a function of radial position. Peaks of spectrum consist of narrow bands of frequency centers are (a) 5.50 MHz, (b) 5.55 MHz, (c) 5.65 MHz and (d) 5.75 MHz. Closed and open circles show radial and azimuthal components of magnetic fluctuations. Fluctuation amplitude is larger in core center region than that in edge region.

Fig.4.10 Axial variation of polarization of fluctuation wave for each peaks of Fourier spectrum. Here, $b_R = (b_r - ib_\theta)/2$ and $b_L = (b_r + ib_\theta)/2$. Polarization fraction is defined by $P_R = b_R^2/(b_L^2 + b_R^2)$ and $P_L = b_L^2/(b_L^2 + b_R^2)$. Component with left-handed polarization is dominant at center region.

Fig.4.11 Wave numbers are determined from phase difference of two magnetic probes at $z = -1.12$ m and -1.28 m and at $z = 0.3$ m and 0.9 m. Wave numbers between $z = -1.12$ m and -1.28 m are shown by closed square. Wave numbers between

$z = 0.3$ m and 0.9 m are shown by opened square. Wave numbers converge to zero with increase of AIC driving term. In region with zero wave number, AIC mode is standing wave. In outer region, AIC mode propagate to both anchor cells. Region of standing wave is expanded with the increase of AIC driving term.

Fig.4.12 Schematic of axial structure of perpendicular and parallel pressure in direction of magnetic field line AIC mode has axial reflection points. At inner region of reflection points, AIC mode is standing wave. At outer region of reflection points, AIC mode propagates toward both anchor cells.

Fig.4.13 Boundary condition for eigen value equation on AIC mode. Initial perturbation excited at $z = 0$ propagates toward positive ϕ_+ and negative ϕ_- direction along the z -axis and reflected at $z = \pm L/2$ with reflection coefficient R as ϕ_+'' , ϕ_-'' . Wave component ϕ_+' reflected at $z = L/2$ is again reflected at $z = -L/2$ with reflection coefficient R as ϕ_+'' . As a result, unstable wave should satisfy the condition of $\phi_+ = \phi_+'' + \phi_-'$.

Fig.4.14 (a) Eigenmodes about k_+ are evaluated from Eq.4.23. Boundary length $L\Omega_{pi}/c$, reciprocal of pressure anisotropy τ , beta value β_{\perp} and reflection coefficient R are given as 20, 0.08, 0.007 and $\sqrt{5}$, respectively. Real and imaginary parts of frequency and imaginary part of wave number are derived as a function with respect to real part of wave number. (b) Propagation of mode number of $n = 8$ is shown by contour of amplitude. Standing wave is excited between boundary

$L\Omega_{pi}/c = 20$ and leaks out as propagating wave to anchor cells.

- Fig.4.15 (a) Parameter dependence of frequency spectrum which are theoretically obtained. n is axial mode number. AIC driving term ($\beta_{\perp}(P_{\perp}/P_{\parallel})^2$) dependence of frequency spectrum of AIC mode. Fixed parameters are $\tau = 0.08$, $R^2 = 0.5$ and $L\Omega_{pi}/c = 20$. A variety of AIC driving term is originated from beta value.
- (b) AIC driving term ($\beta_{\perp}(P_{\perp}/P_{\parallel})^2$) dependence of frequency spectrum of AIC mode. Fixed parameter is $\beta_{\perp} = 0.007$, $R^2 = 0.5$ and $L\Omega_{pi}/c = 20$. Variety of AIC driving term is originated from reciprocal of pressure anisotropy (τ).
- (c) Boundary length ($L\Omega_{pi}/c$) dependence of frequency spectrum of AIC mode. Fixed parameter are $\beta_{\perp} = 0.007$, $R^2 = 0.5$ and $\tau = 0.08$.

Fig.4.16 Experimentally-obtained frequency spectra which vary temporally with the increase of diamagnetism, density and temperature.

Fig.4.17 Typical time evolution of (a) electron line density, (b) diamagnetic loop signal in the central cell. Midplane loop signal is represented by W_1 , the second loop signal W_2 and the third loop signal W_3 and power supplied by RF1 and RF2. Input power of RF2 for heating ions in central cell is modulated from 75 ms to 85 ms.

Fig.4.18 AIC driving term dependence of frequency spectrum. Pressure and pressure anisotropy are controlled by using RF modulation method. Solid, dotted, dashed and dotted-dashed lines are correspond with axial mode numbers of $n = 7, 8, 9, 10$,

respectively, which are theoretically obtained with $\tau = 0.08$, $R^2 = 0.5$, $L\Omega_{pi}/c = 20$ and varying β_{\perp} .

Fig.4.19 (a) Relations between AIC driving term, beta value and reciprocal of pressure anisotropy. At parameter of (I) and (II), the boundary for eigenmode of AIC mode is cross over magnetic probes at $z = 30$ and 90 cm and at $z = -112$ and -128 cm. Parameter of (III) is used for theoretical evaluation of frequency spectrum. Maximum driving term is obtained at parameter of (IV). (b) Axial profile of AIC driving term are evaluated for parameter of (I),(II),(III) and (IV). Dotted line is magnetic field strength. Broken-dotted line is AIC driving term of 0.5, which correspond with parameters of reflection point of AIC mode.

Fig.4.20 Time evolutions of experimental data: (a) diamagnetic loop signals at midplane W_1 and off-midplane W_2 , (b) SED signals which are set in direction of pitch angles of 90 deg. SED(90), and 45 deg. SED(45), and signal ratio of SED(45) to SED(90), (c) end-loss ions which are near loss-cone boundary of central cell, with energy of 5.1 keV, (d) amplitude of AIC mode.

Fig.4.21 (a) Ratio of small Faraday cup signal at end to that at beginning of the period as a function of pitch angle, (b) pitch angle distribution at beginning (●) and end point (○) of period.

Fig.5.1 (a) Anisotropy vs. midplane diamagnetic signal, (b) amplitude of AIC mode vs. midplane diamagnetic signal on both cases with (●) and without off-midplane

resonance (\bigcirc).

Fig.5.2 (a) Solid and dotted lines are axial profile of pressure and magnetic field strength, respectively, (b) solid and dotted lines are axial profile of κ_ϕ and $P\kappa_\phi/B$, respectively.

Fig.5.3 Pressure anisotropy dependence of Γ due to hot pressure component in (a) central and (b) anchor cell. (c) Integration of cold component from $z = 0$ to z .

Fig.5.4 Dependence of critical beta ratio of β_C to β_A on pressure anisotropy ($P_{\perp C}^h/P_{\parallel C}^h$) of central cell. α is ratio of cold pressure component to hot pressure in anchor cell.

Fig.5.5 Experimentally-obtained flute-interchange stability boundary of GAMMA10 on $\beta_{\perp C}$ vs. $\beta_{\perp A}$ diagram. Solid line is theoretical stability limit for a plasma with pressure anisotropy in central cell and dotted line is stability limit for an isotropic plasma.

Fig.5.6 Temporal variation of anchor and central cell diamagnetism with additional gas puffing in anchor cell.

Fig.5.7 Identification of a flute interchange mode by use of edge probe array. Density fluctuation rotates in order 135, 90, 45 and 0 deg. Density fluctuation are axially in phase at $z = -0.6$ and 5.0 m.

Fig.5.8 Beta ratios β_{LC}/β_{LA} plotted against pressure anisotropy. Critical beta ratio strongly depends on pressure anisotropy. Stronger anisotropy leads to larger critical beta ratio. Solid line show theoretically derived relation between critical beta ratio and pressure anisotropy.

Fig.5.9 RF2 power dependence of (a) diamagnetic signal of W_1 and W_A , (b) pressure anisotropy of central cell and (c) density at midplane and mirror throat of central cell.

Fig.5.10 Radial profile of density at midplane (dashed line) and mirror throat (\times), inner transition of magnetic field from central cell to anchor cell (\bullet) and outer transition (\circ).

Fig.5.11 Pressure anisotropy dependence of pressures at central, anchor and mirror throat. Ratio of cold pressure component to hot component is represented by α .

Fig.5.12 Stability diagram of pressure anisotropy vs. β_{LC} .

Fig.A.1 Structure of MPD plasma gun. Plasma gun has coaxial electrode and pilot anode instead of trigger electrode. Typical discharge voltage, current and duration are about 200 V, 10 kA and 1 ms, respectively.

Fig.C.1 Pole trajectory in complex wave number plane are schematically drawn for (a) no unstable mode and (b) amplifying mode cases.

Fig.C.2 Contour mapping of roots which are evaluated from dispersion relation of

$D(k, \omega) = 0$ are drawn for (a) absolutely and (b) convectively unstable case.

When imaginary component of frequency are moved from 0 to 0.05, trajectories of roots are drawn as white lines. Saddle point is marked in absolute unstable mapping of (a).



Fig. 2.1

Tandem Mirror GAMMA10

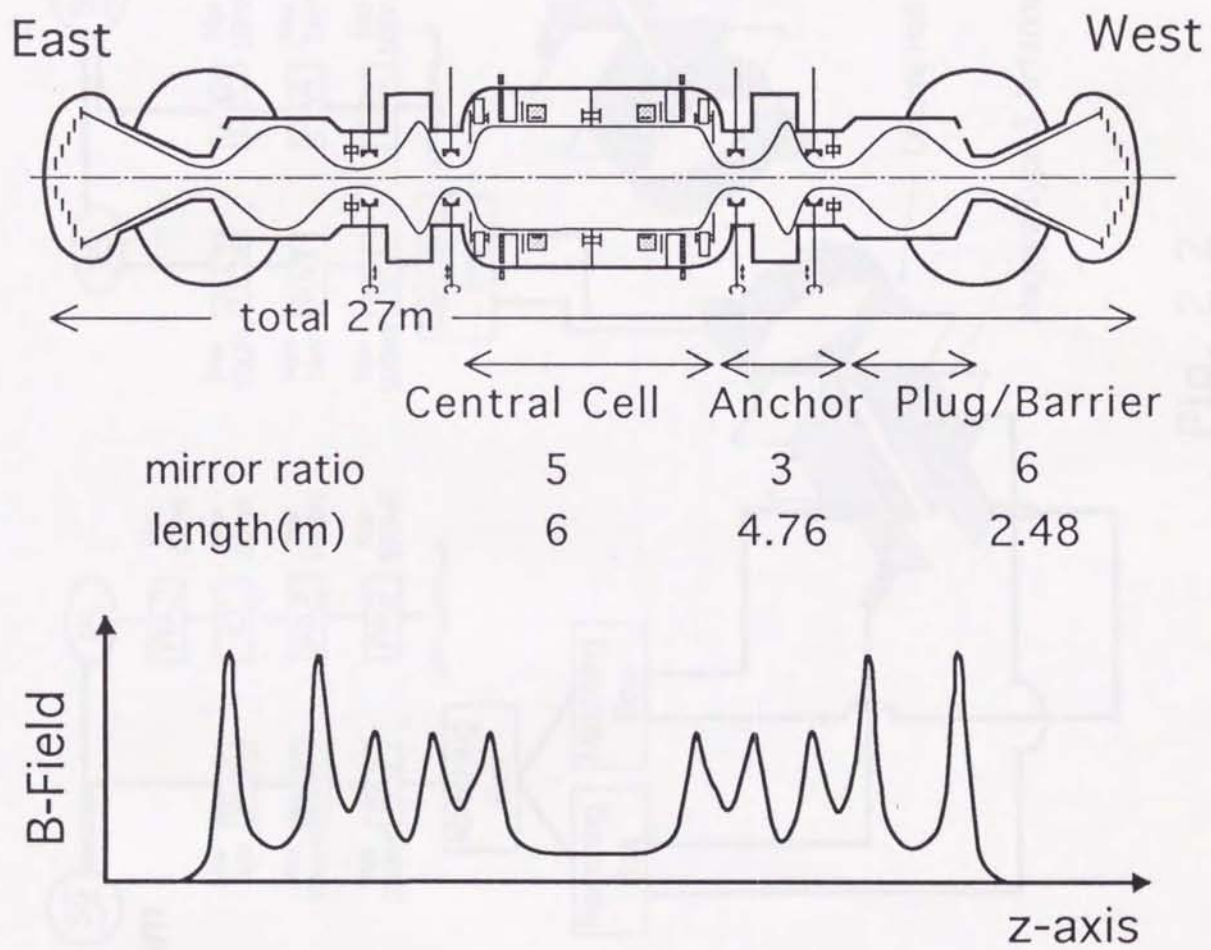


Fig. 2.1

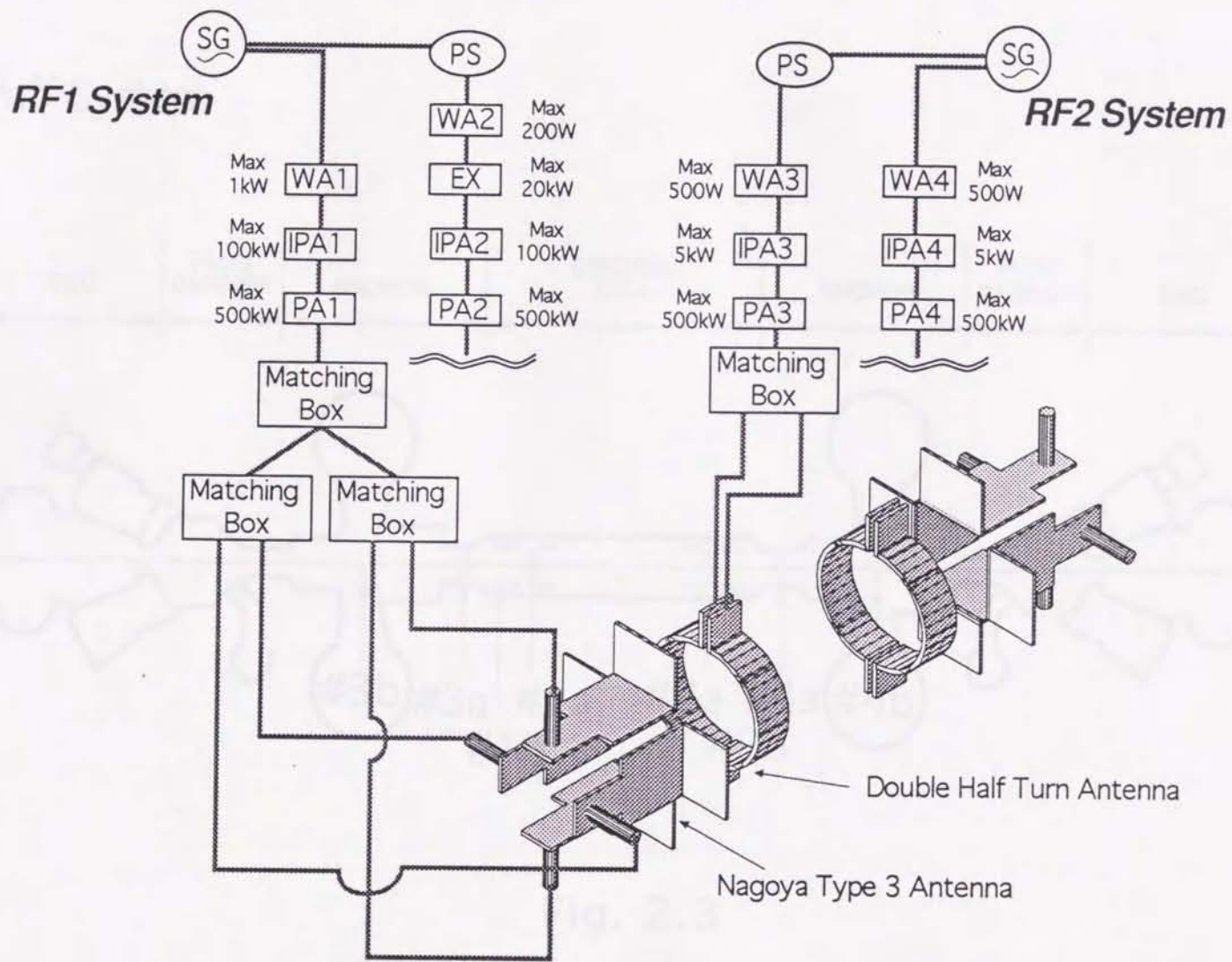


Fig. 2.2

Gas Puff System

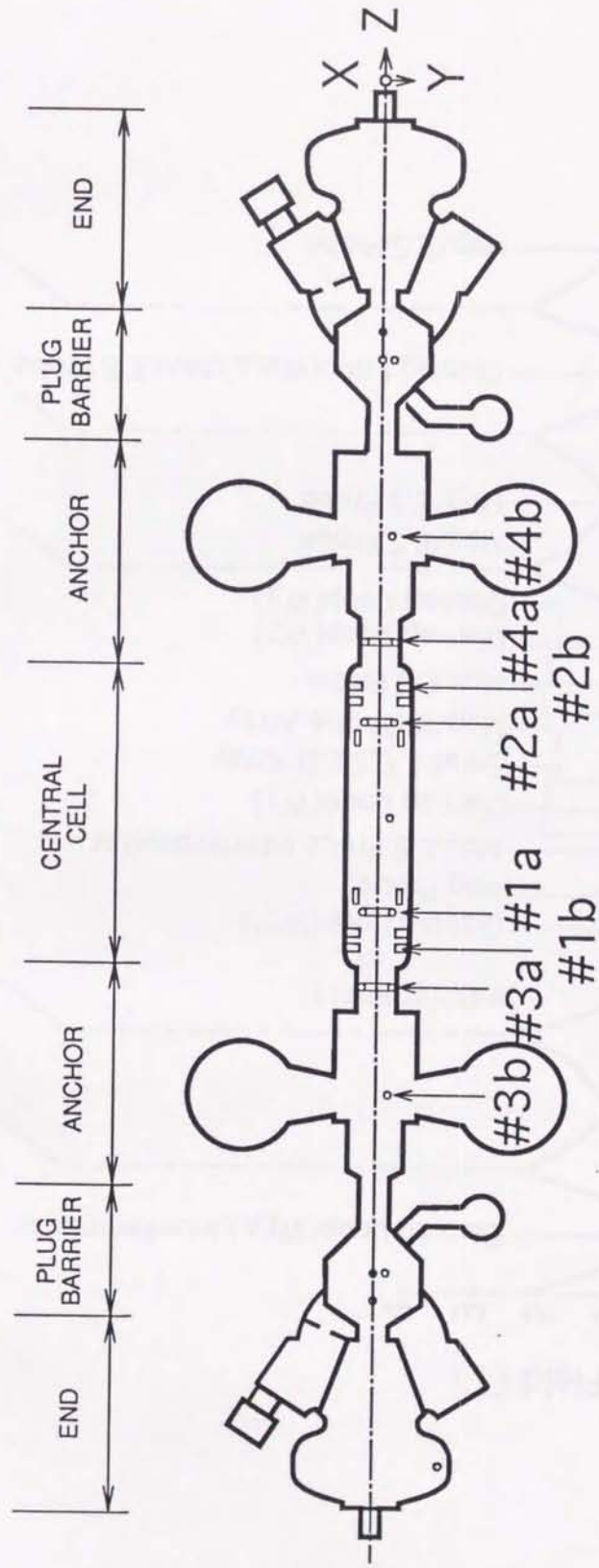


Fig. 2.3

Diagnostics and Heating System

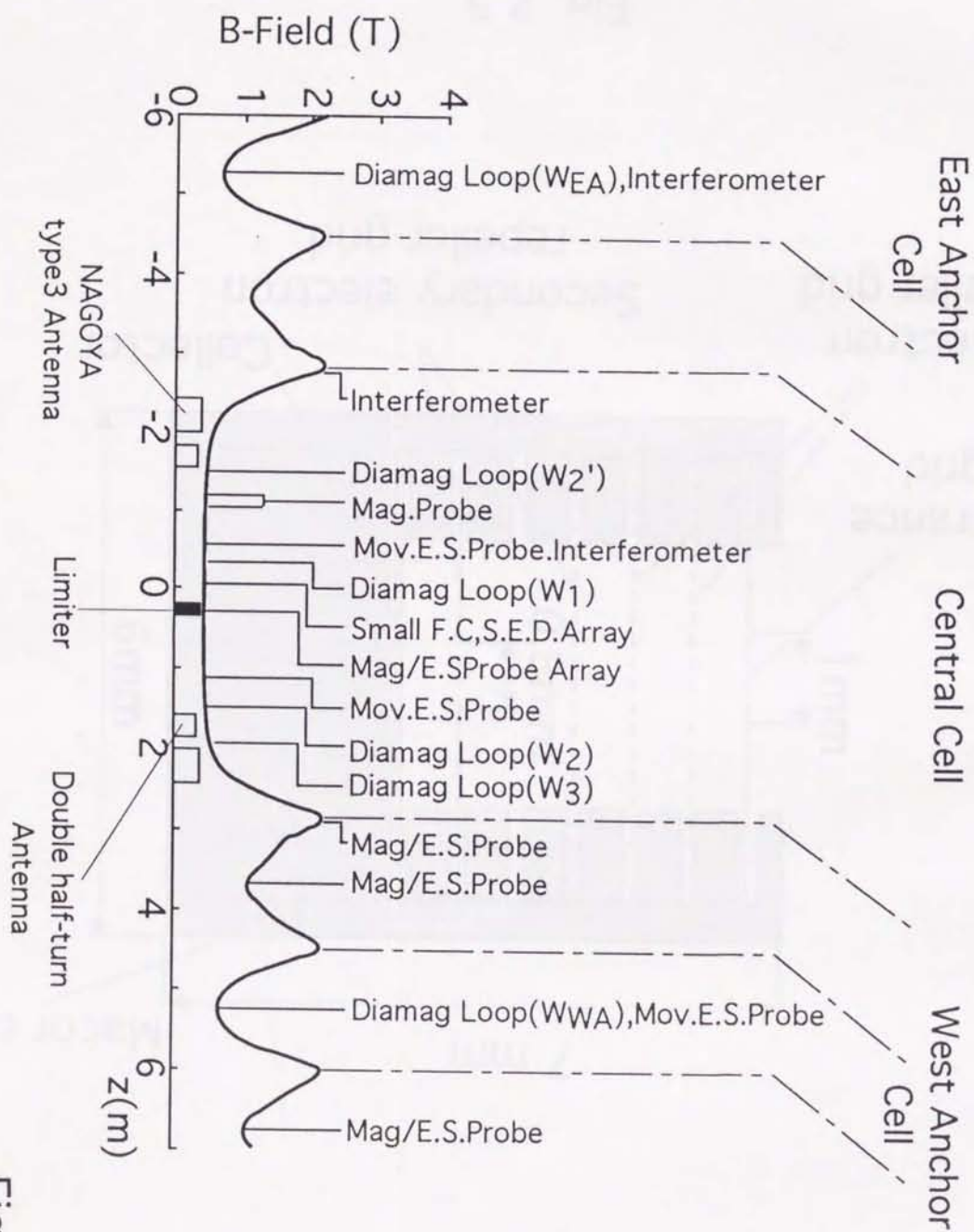


Fig. 2.4

Small Faraday Cup

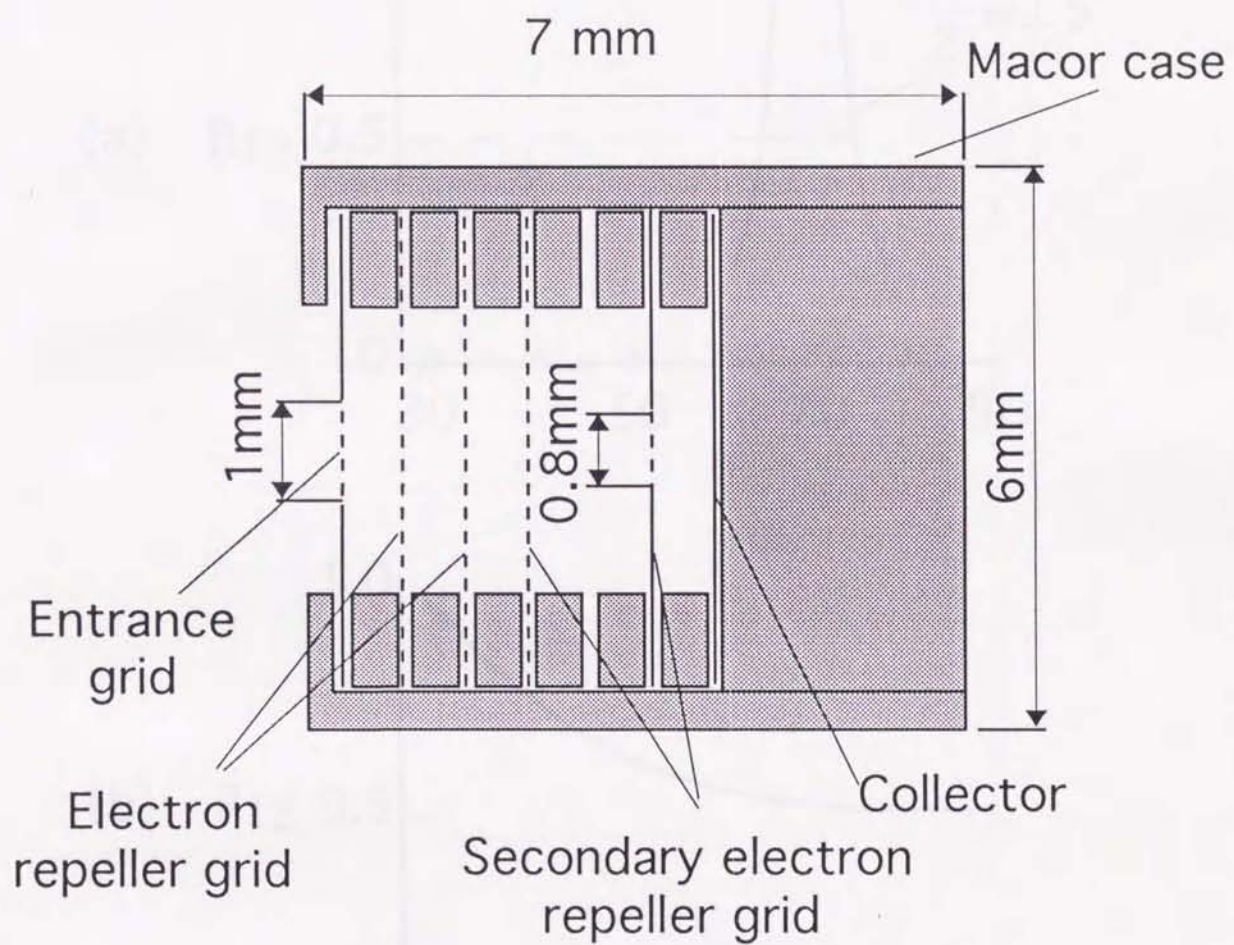


Fig. 2.5

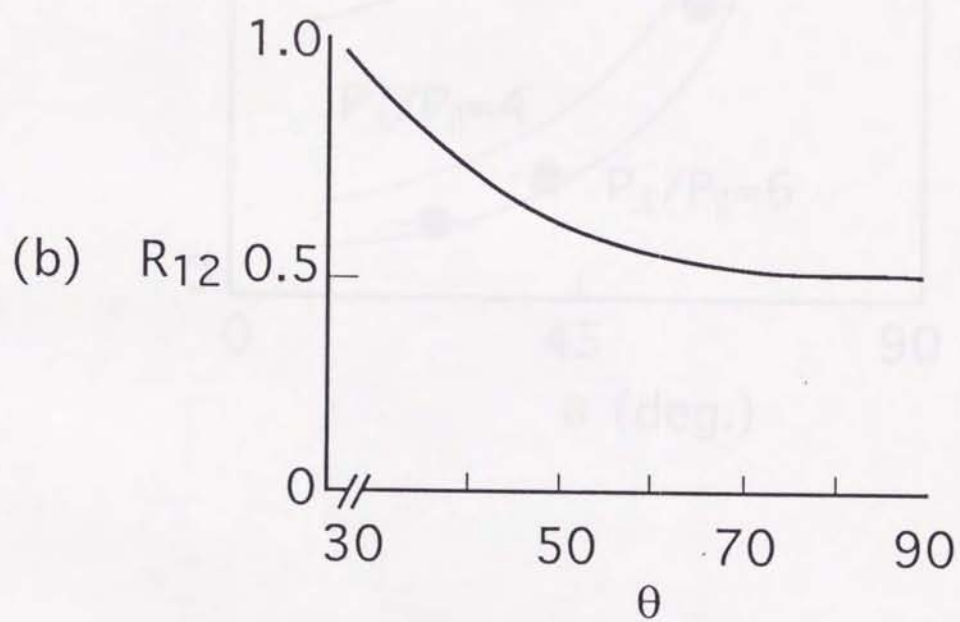
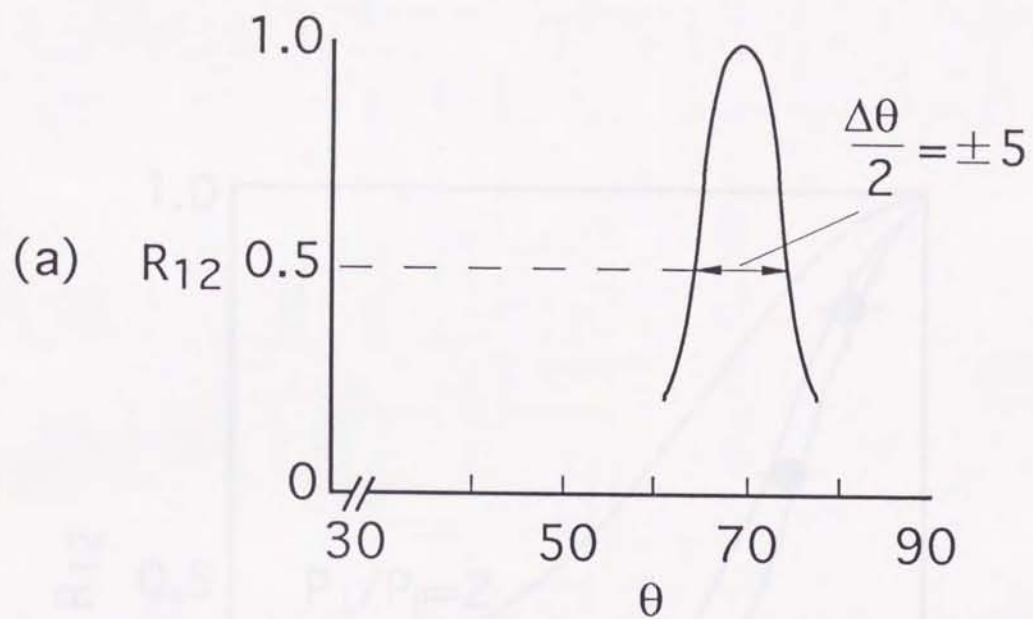


Fig. 2.6

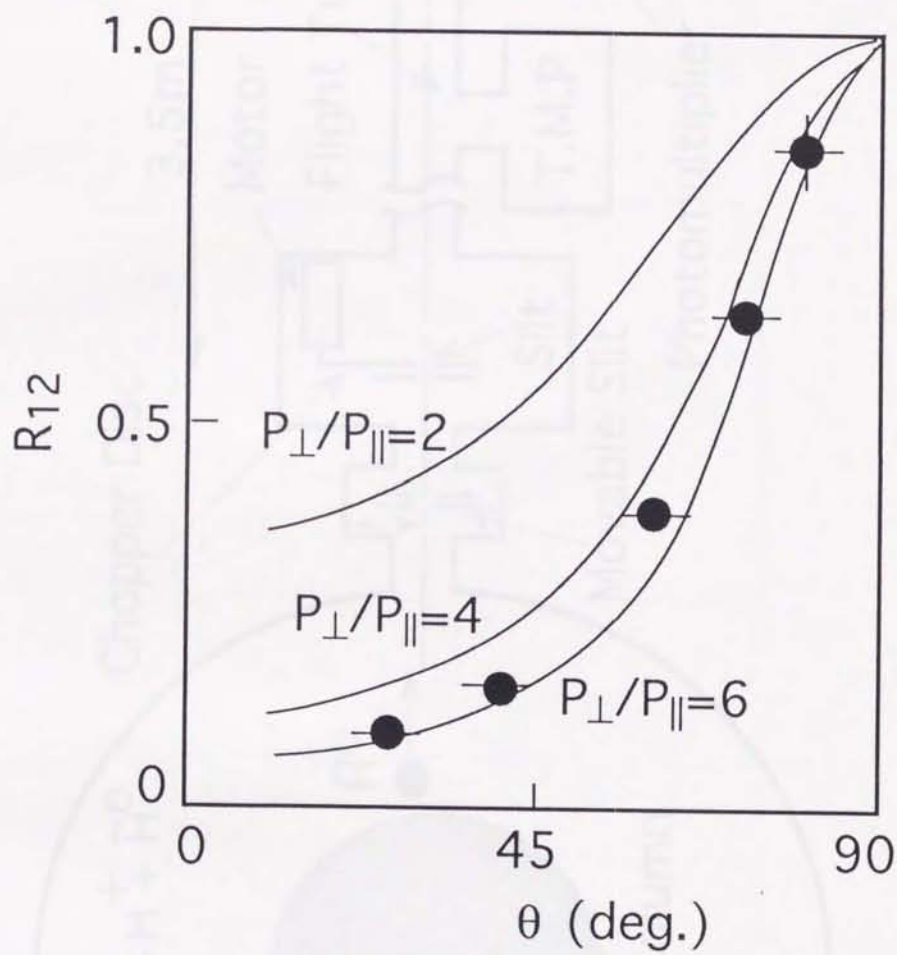


Fig. 2.7

Time of Flight Type Neutral Particle Energy Analyzer

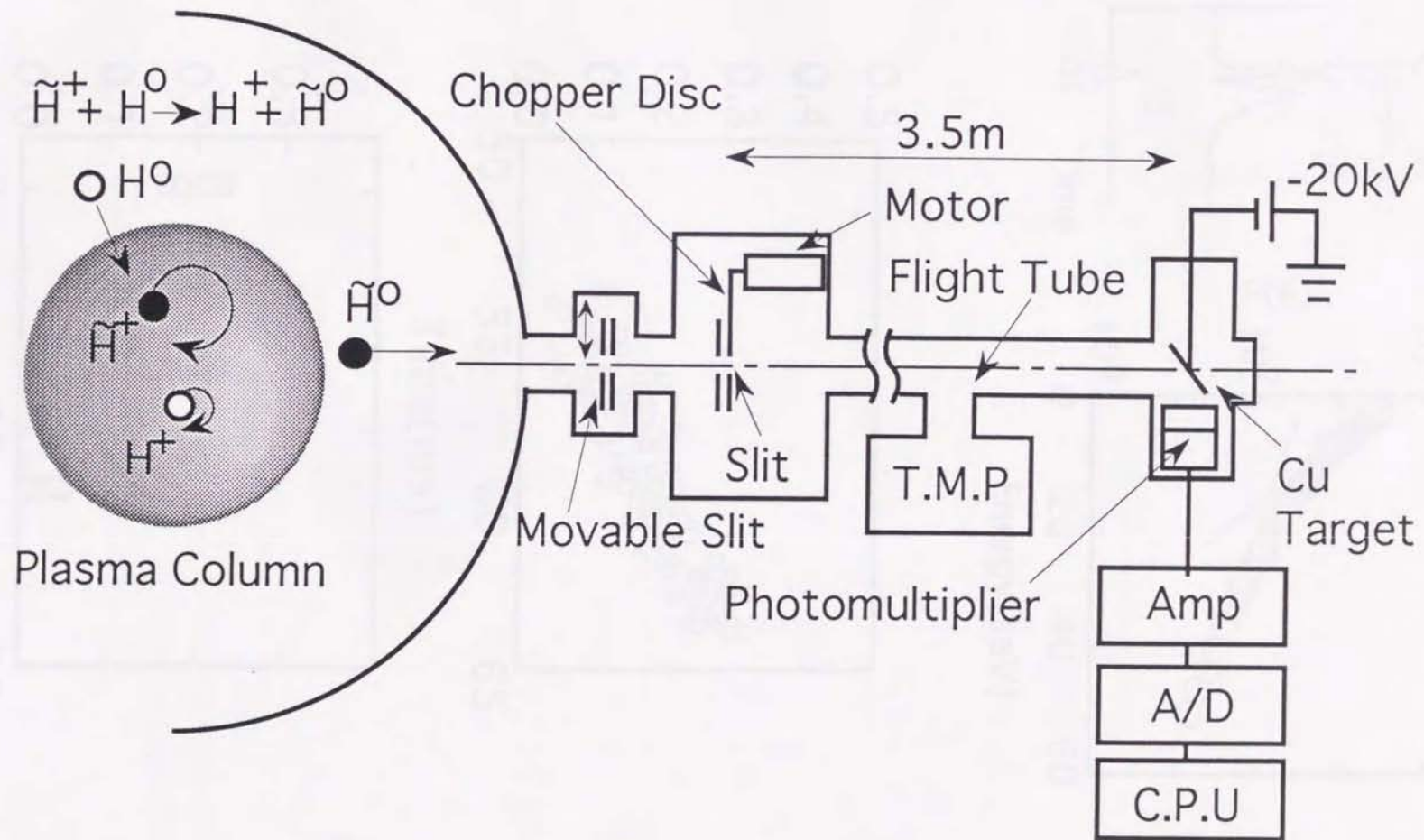


Fig. 2.8

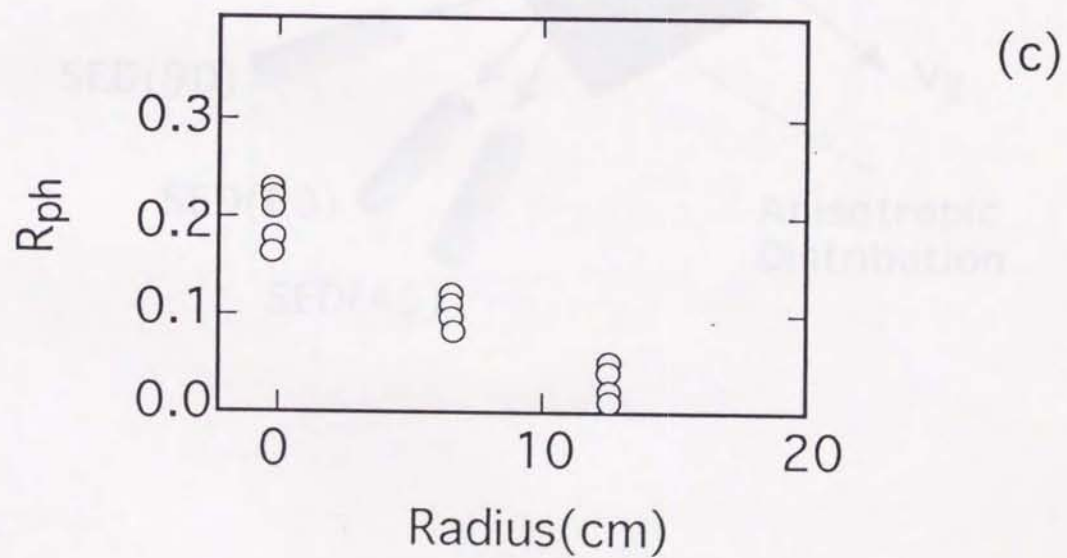
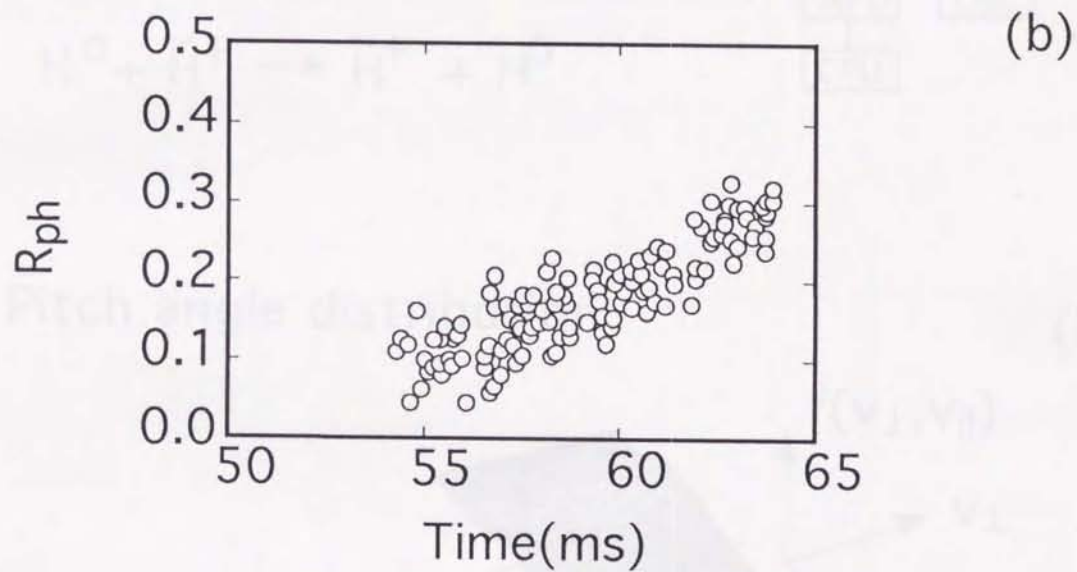
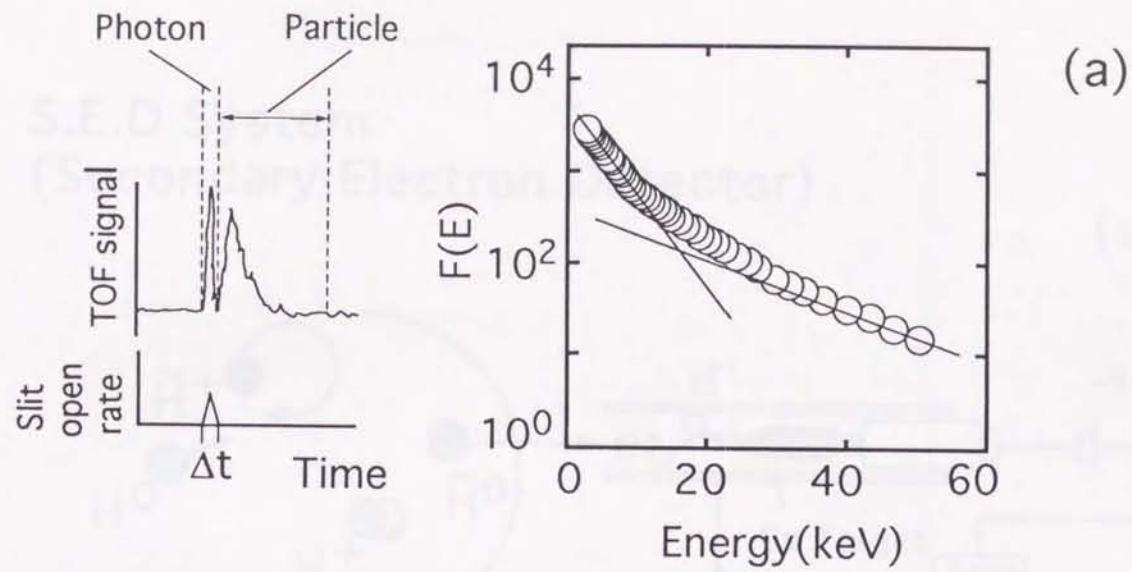
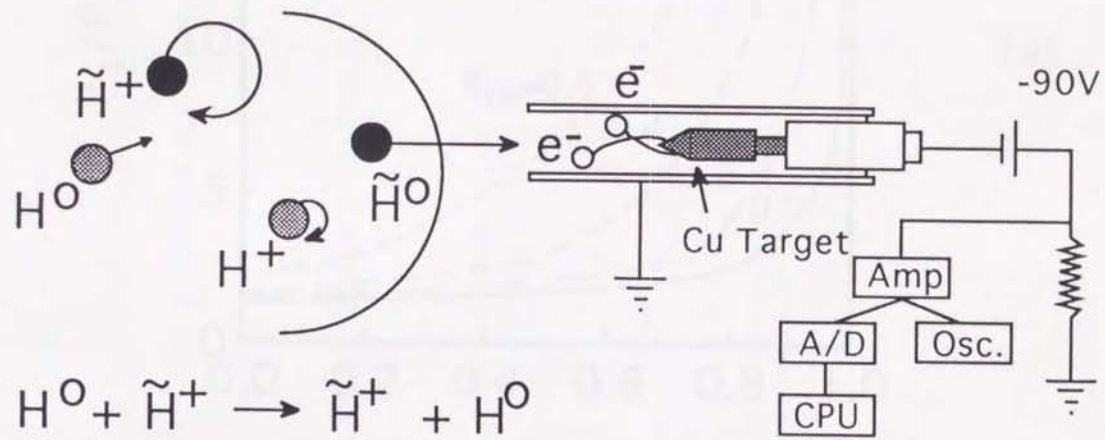


Fig. 2.9

S.E.D System
(Secondary Electron Detector)

(a)



Pitch angle distribution

(b)

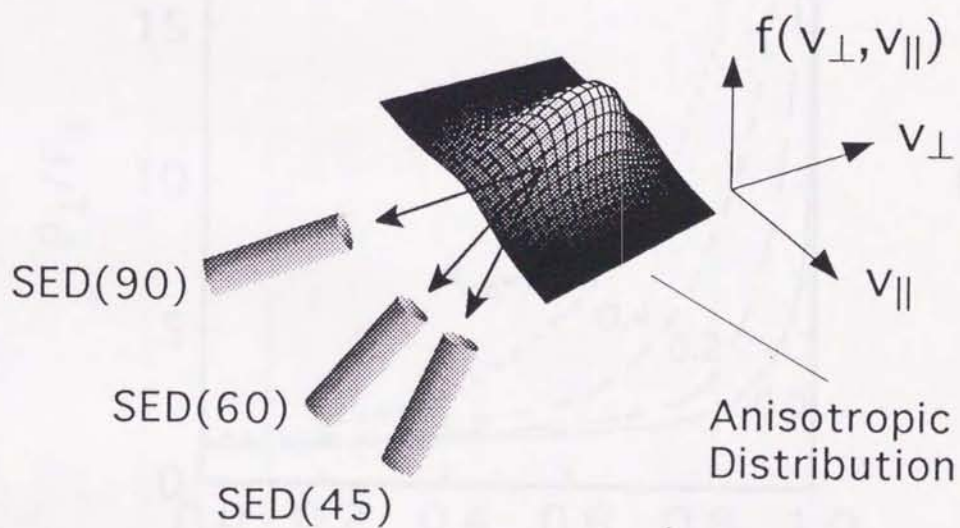
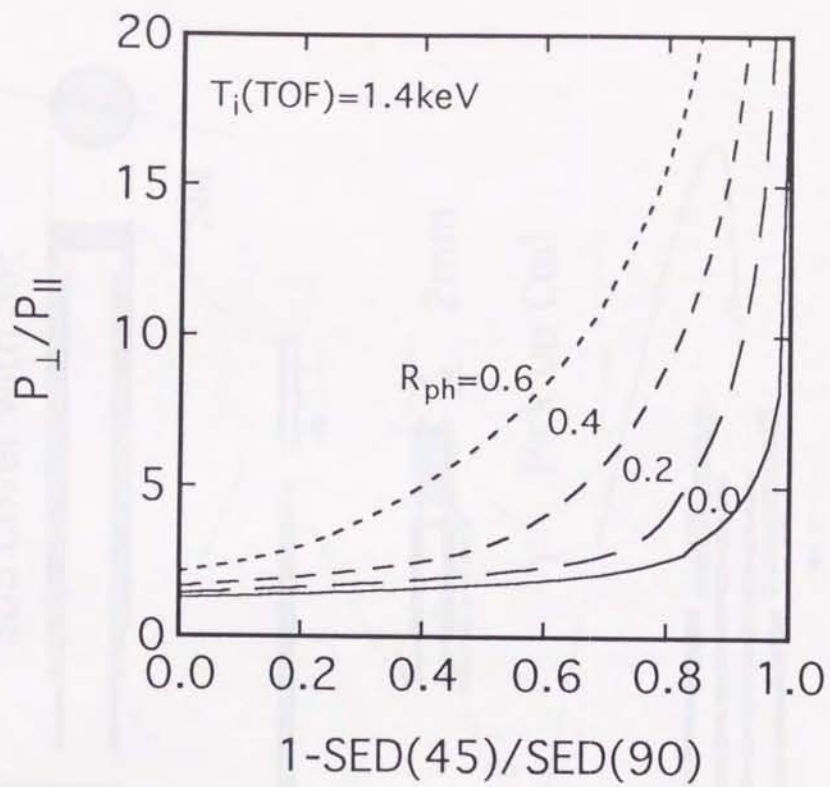
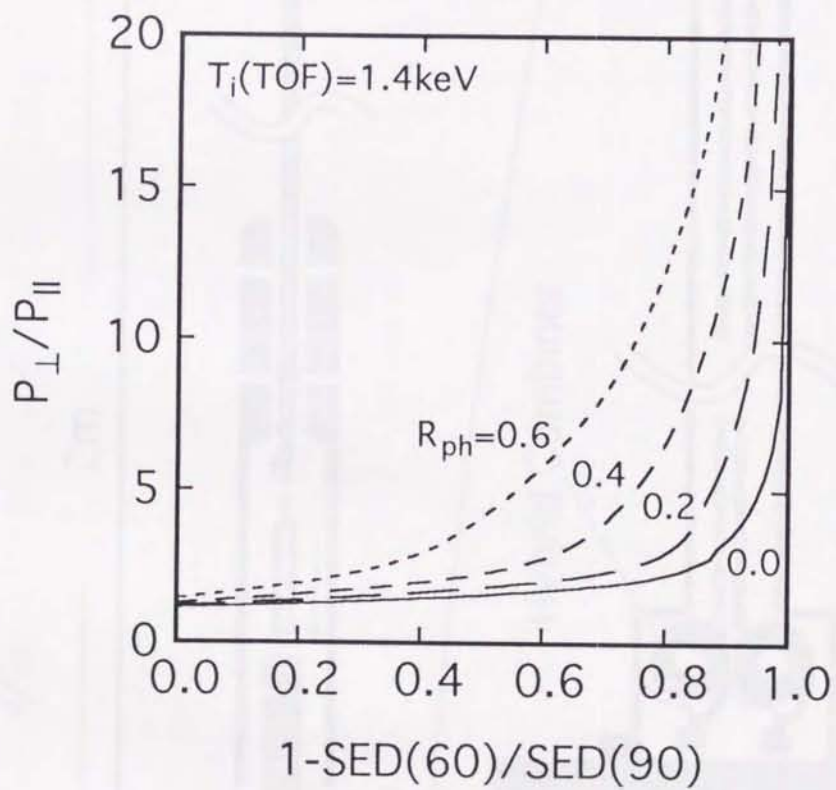


Fig. 2.10

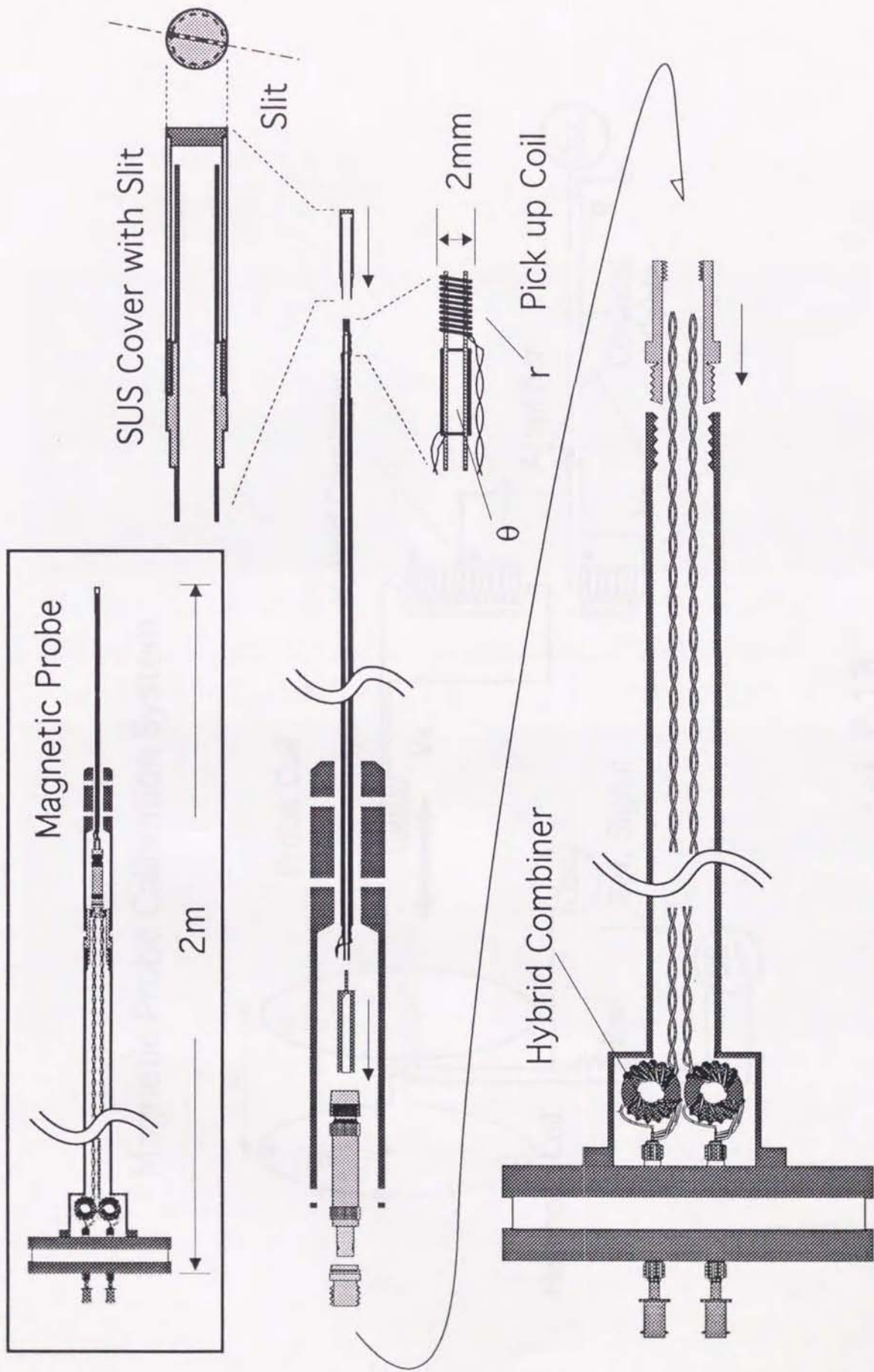


(a)



(b)

Fig. 2.11



All Metal Type Magnetic Probe

Fig. 2.12

Magnetic Probe Calibration System

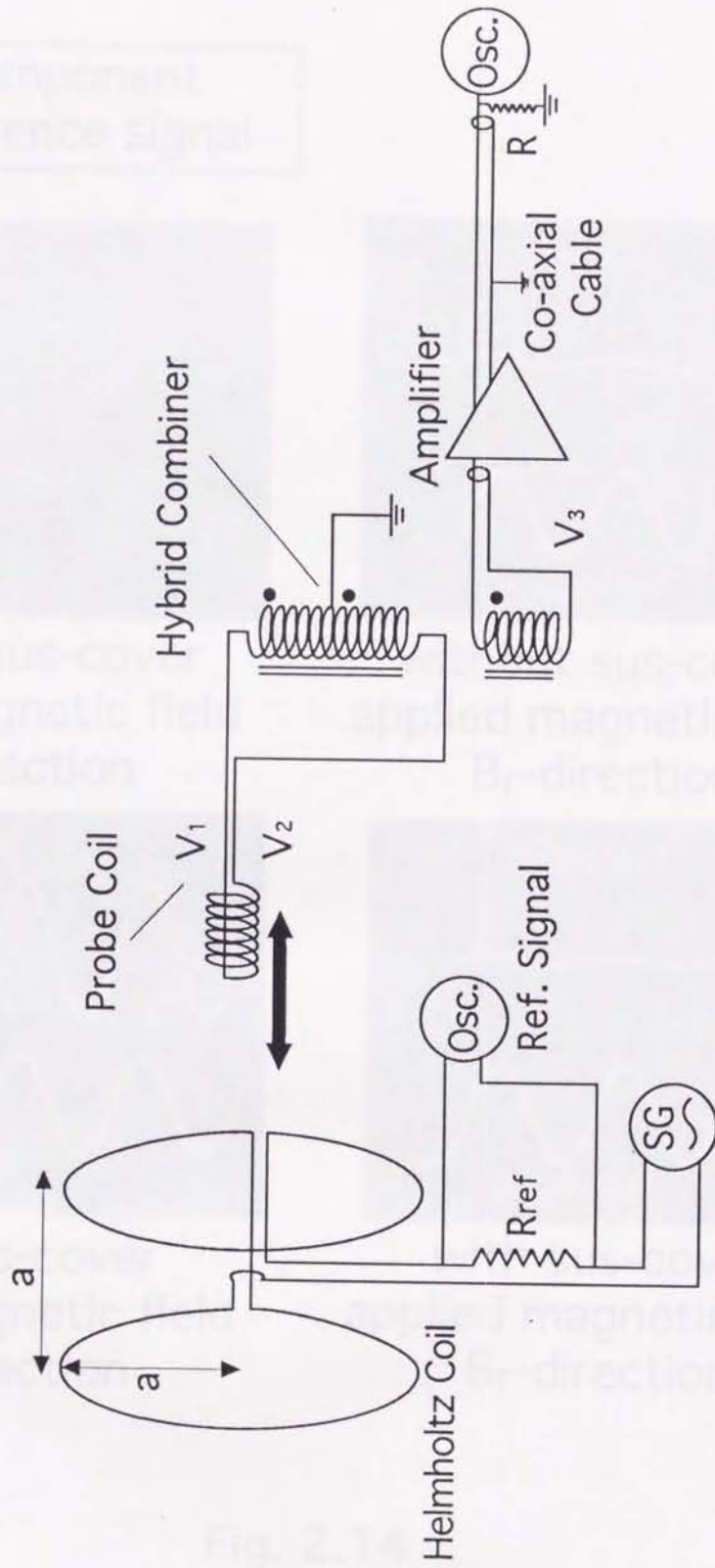
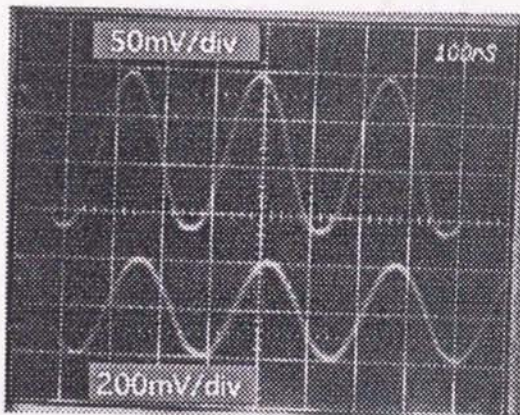
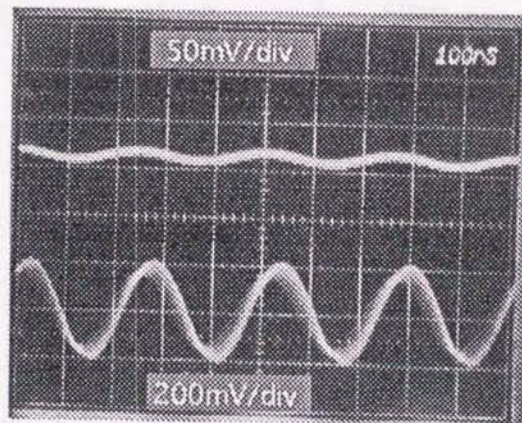


Fig. 2.13

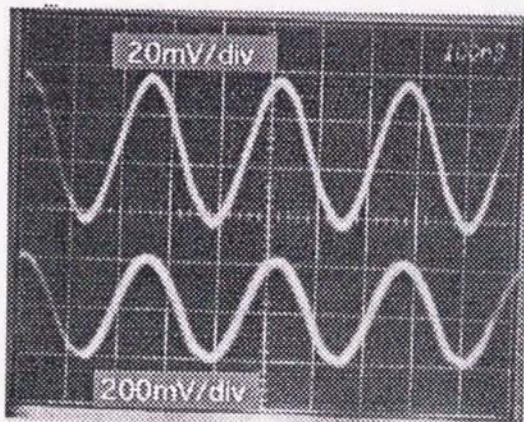
ch1 θ -component
ch2 reference signal



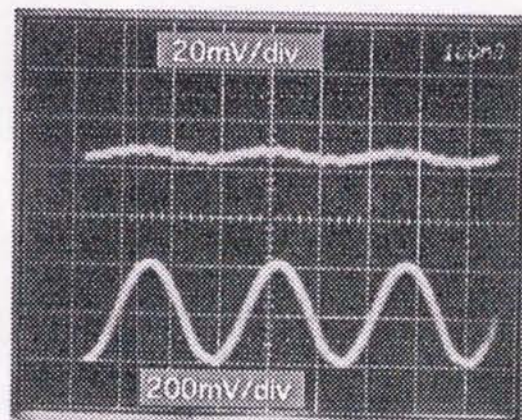
without sus-cover
applied magnetic field
 B_{θ} -direction



without sus-cover
applied magnetic field
 B_r -direction



with sus-cover
applied magnetic field
 B_{θ} -direction



with sus-cover
applied magnetic field
 B_r -direction

Fig. 2.14

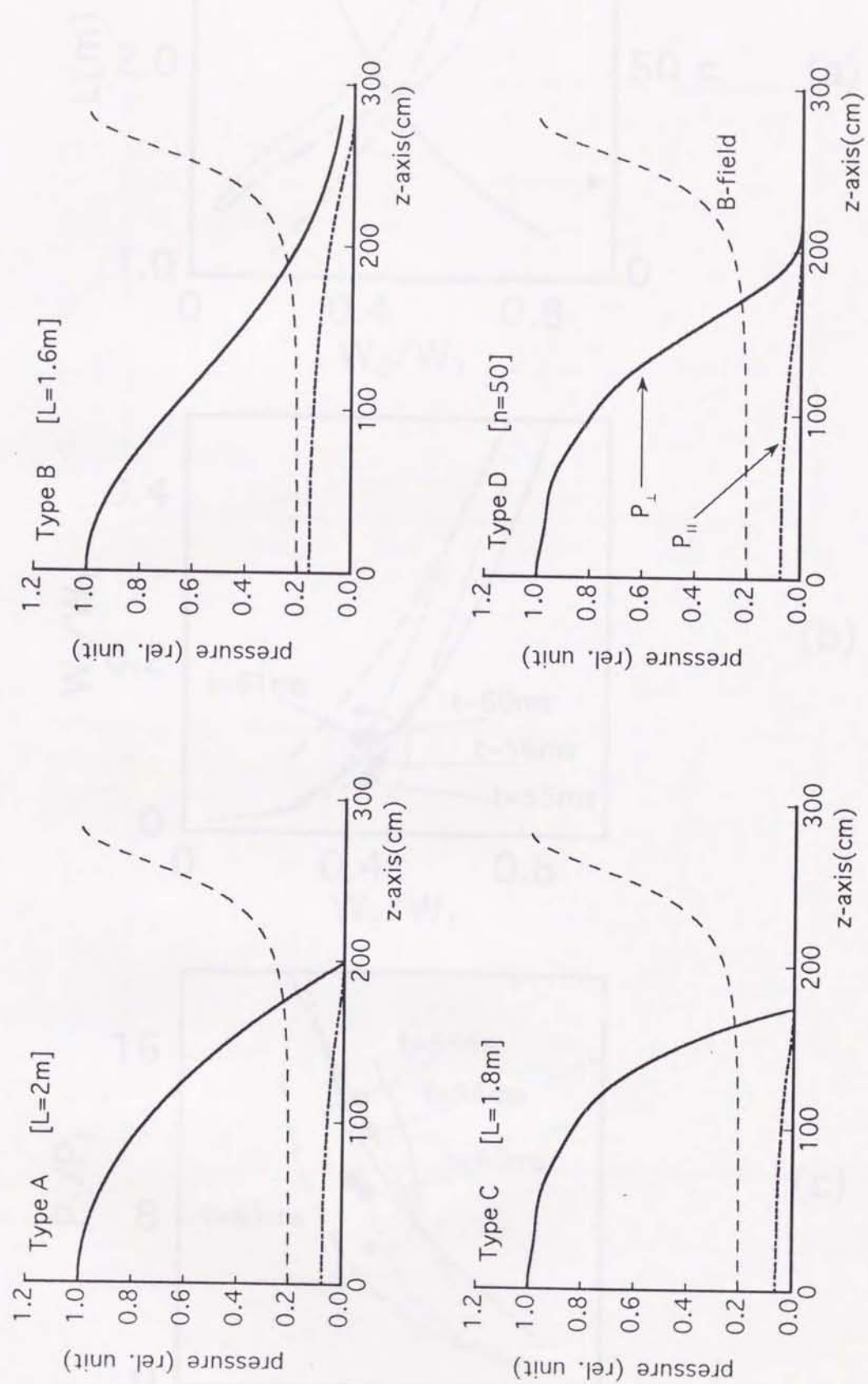


Fig. 3.1

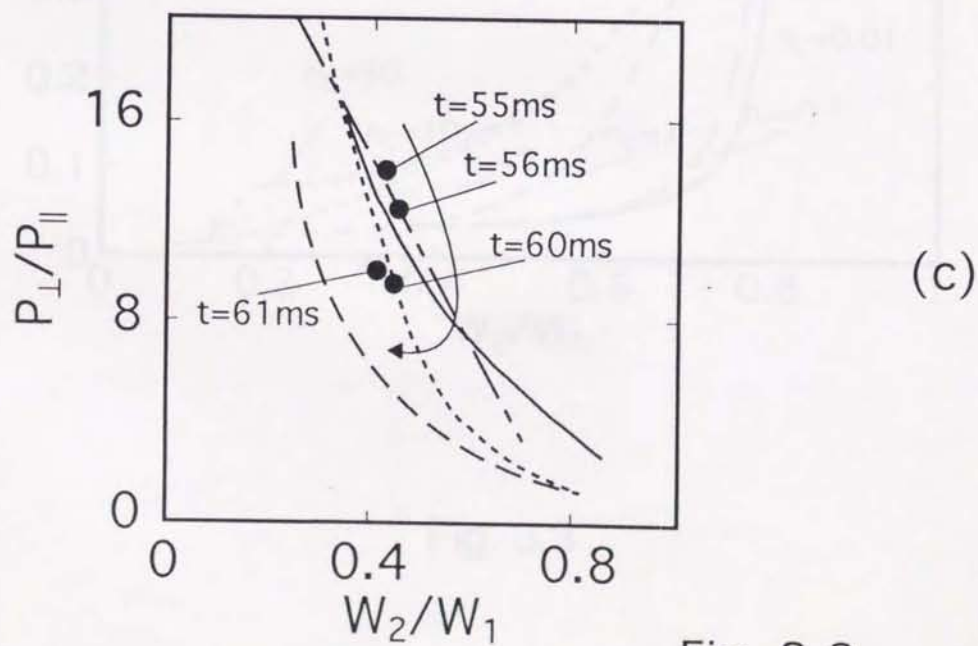
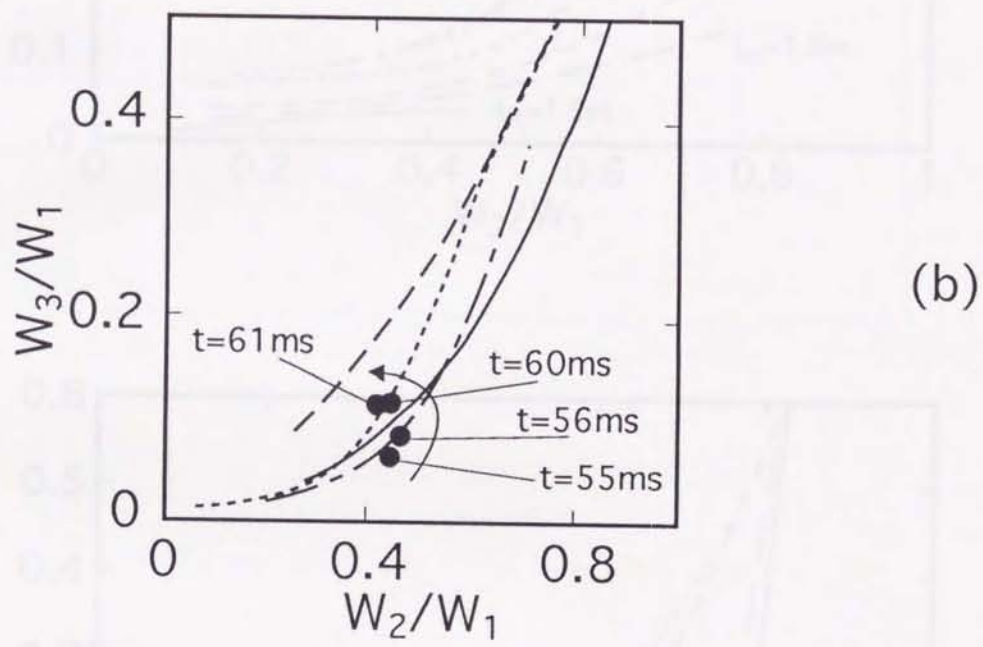
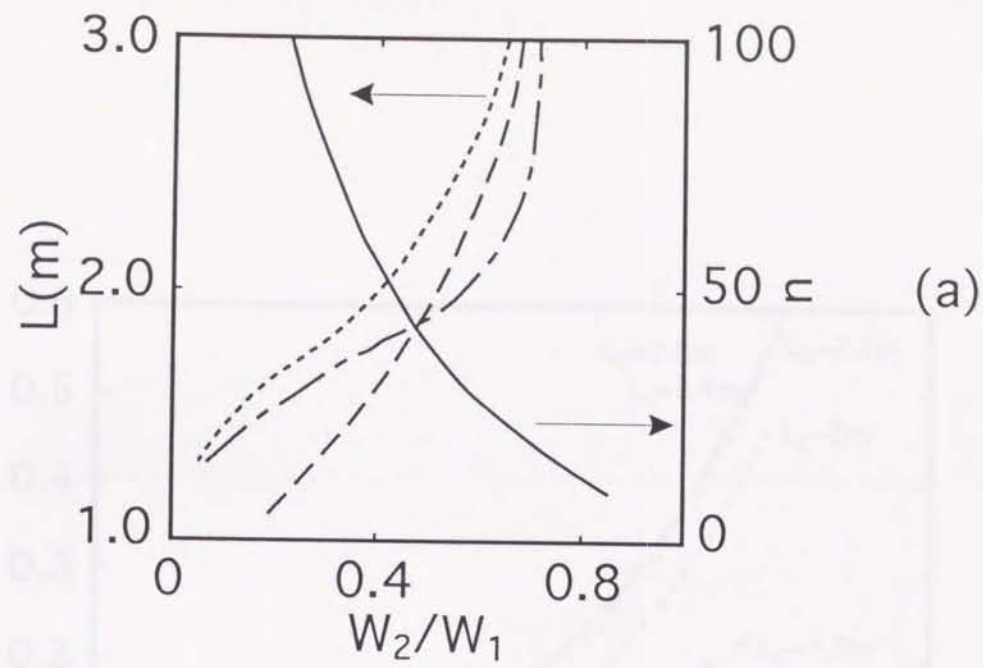
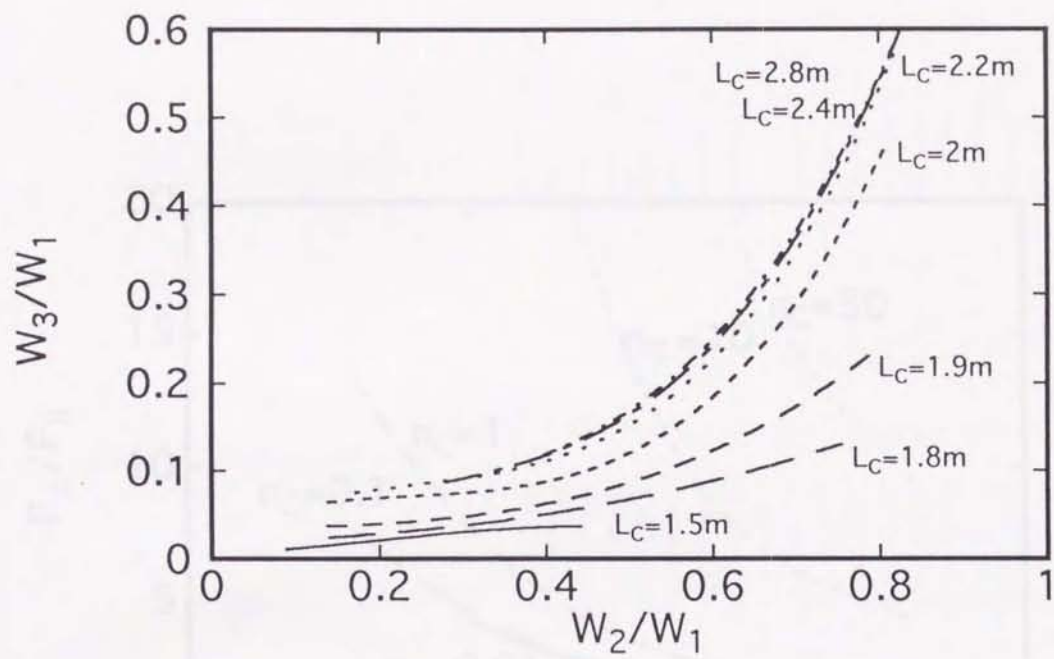
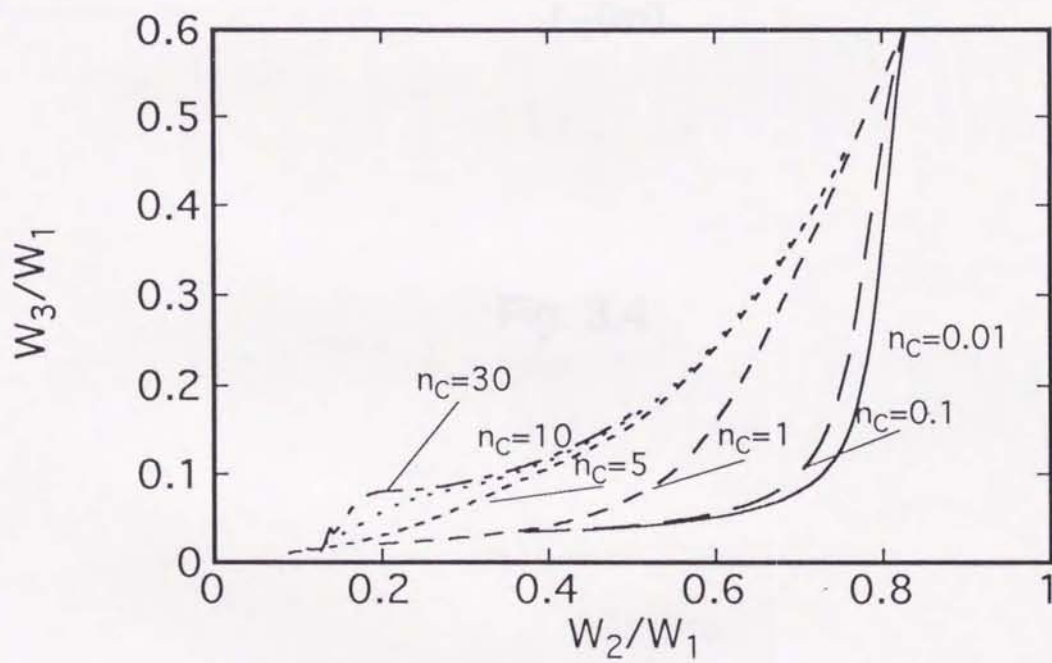


Fig. 3.2



(a)



(b)

Fig. 3.3

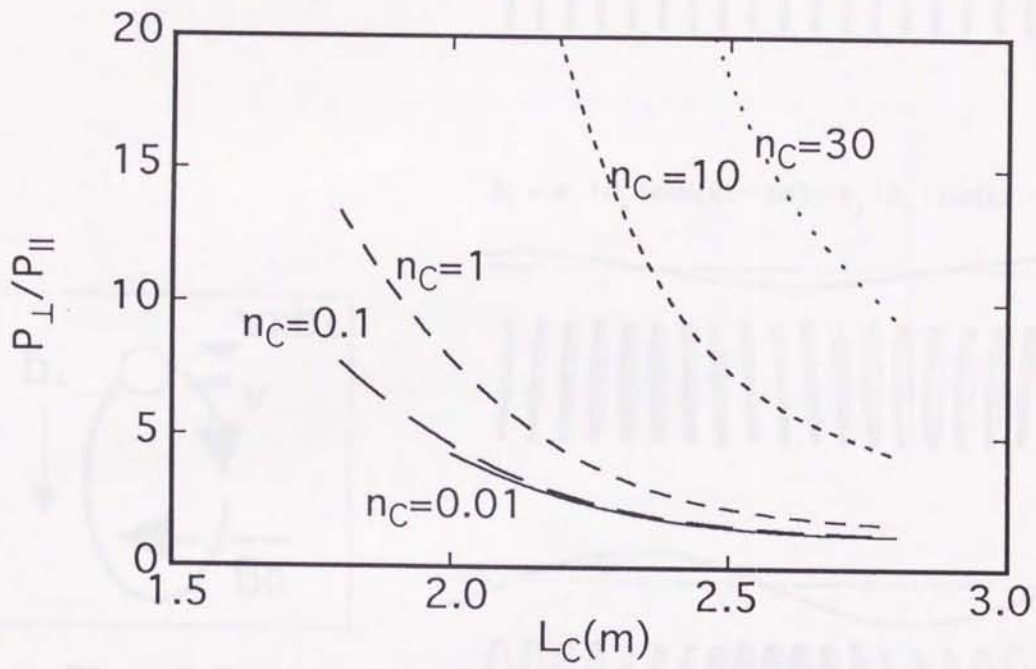


Fig. 3.4

Fig. 4.1

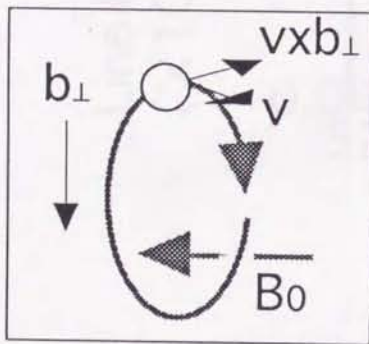


Fig. 4.1a

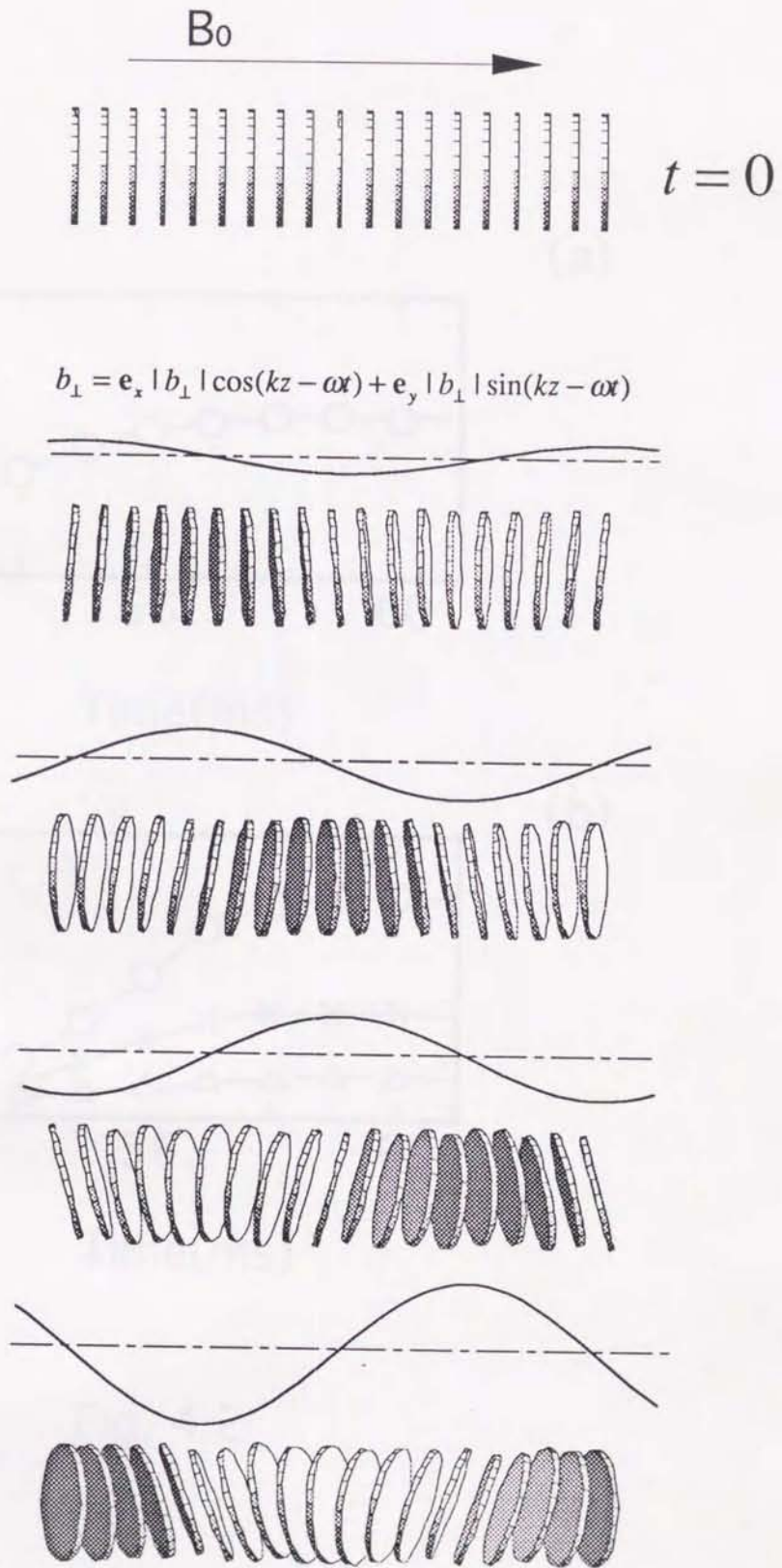


Fig. 4.1

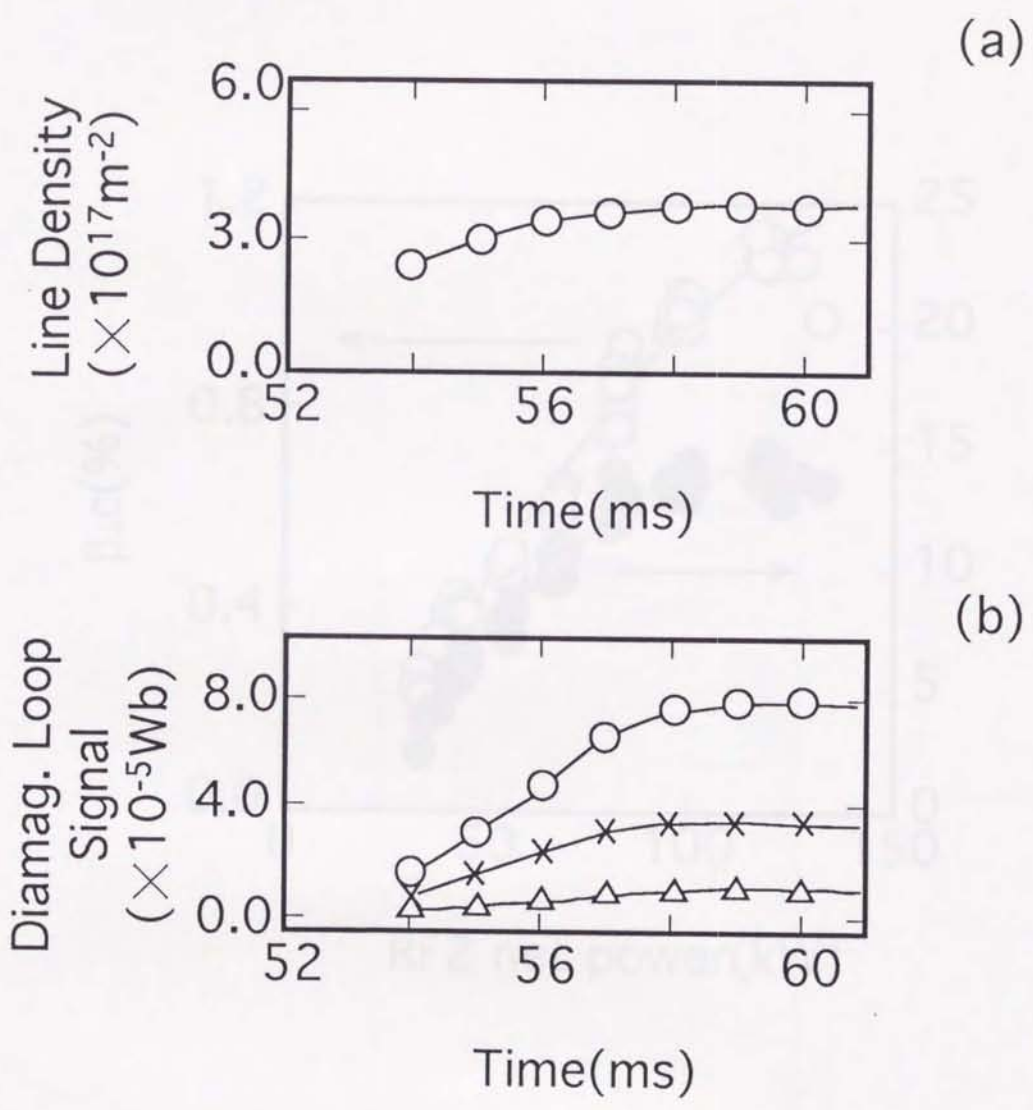


Fig. 4.2

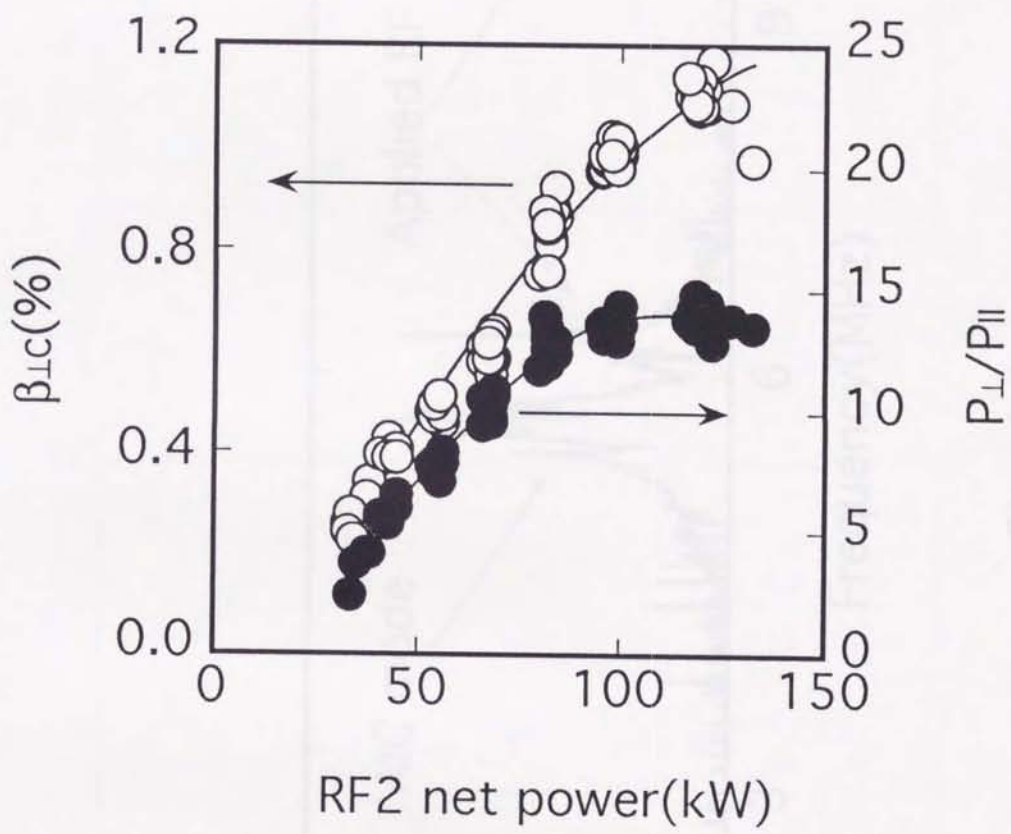


Fig. 4.3

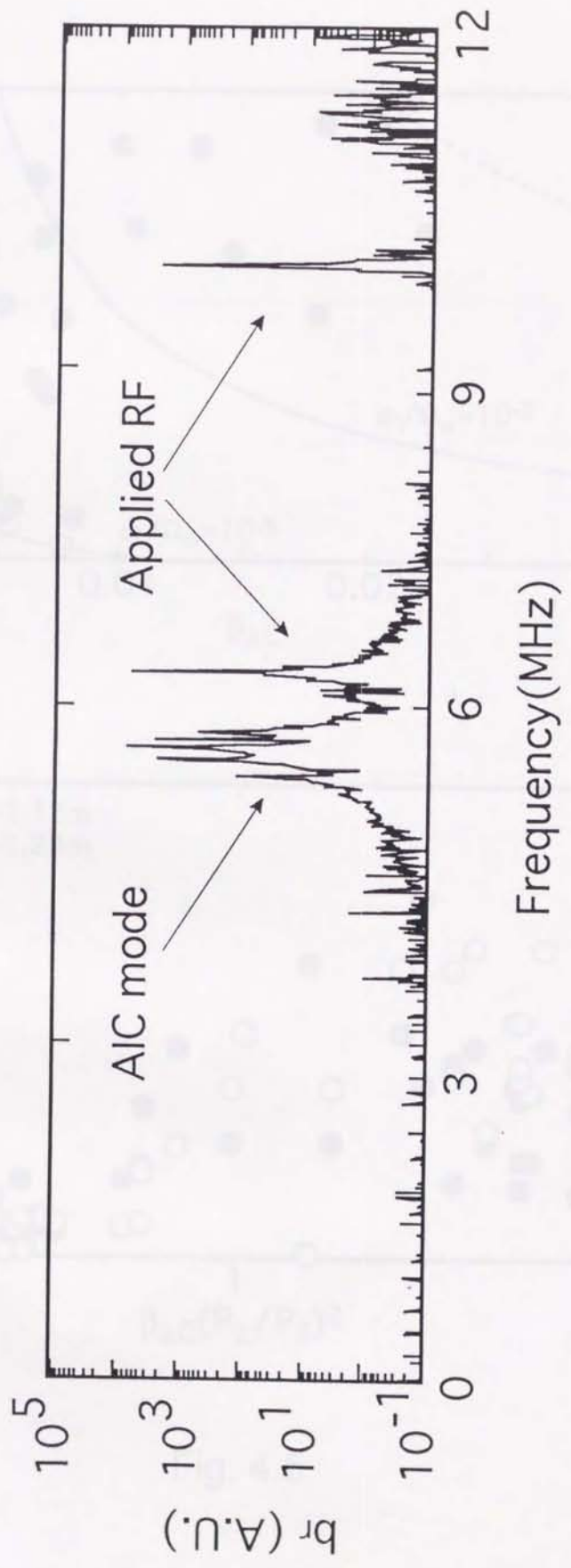


Fig. 4.4

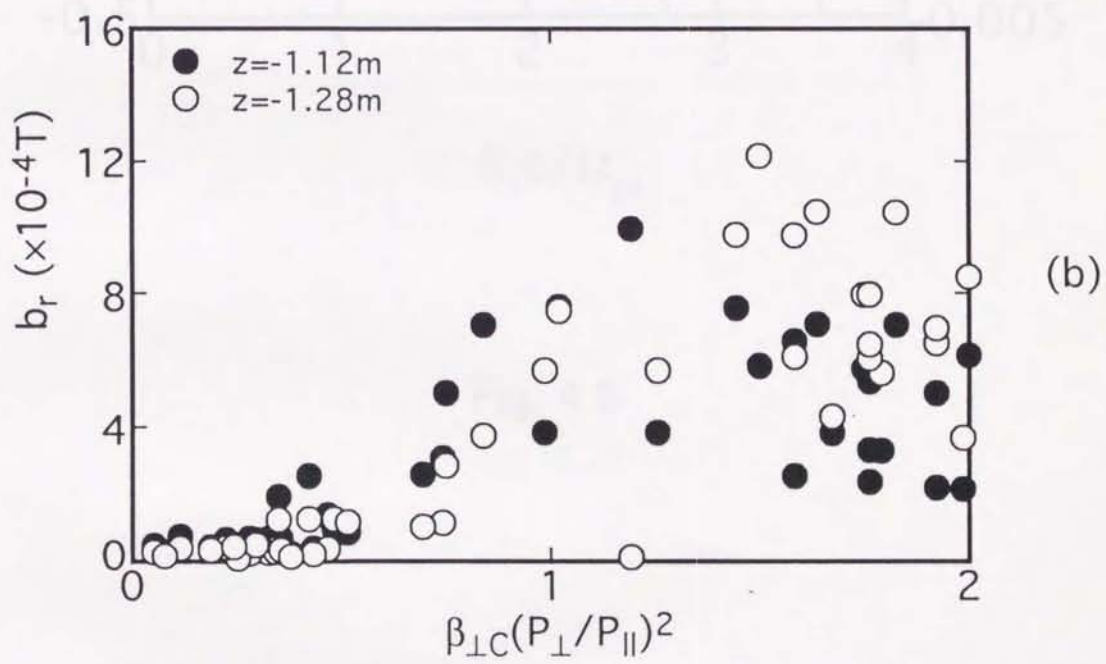
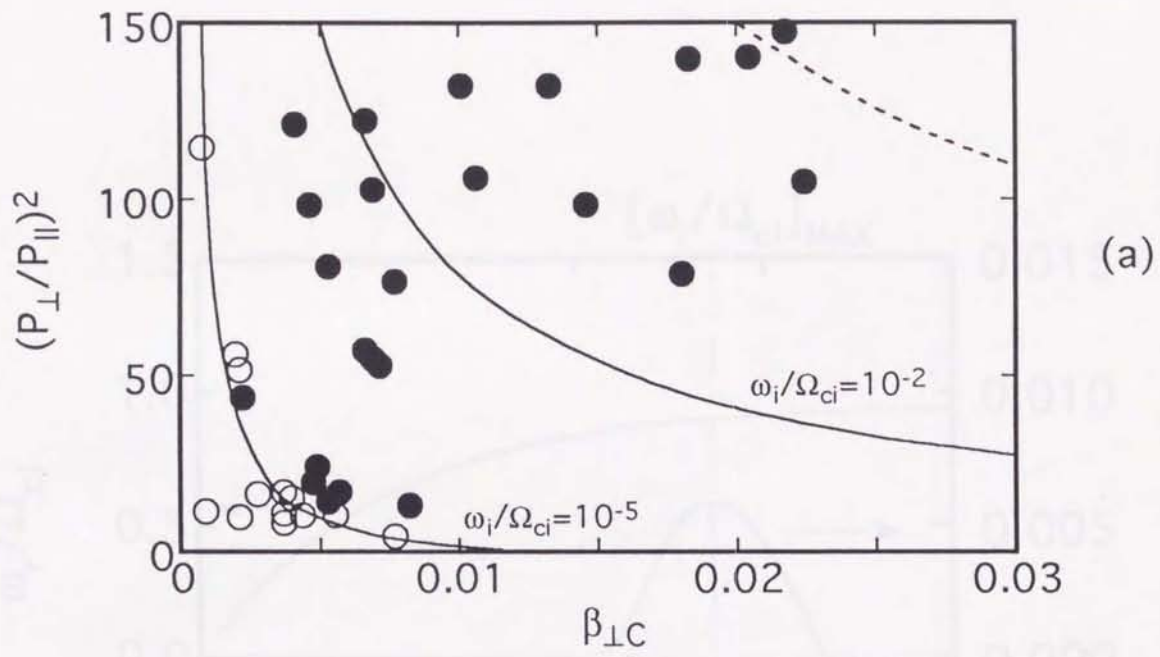


Fig. 4.5

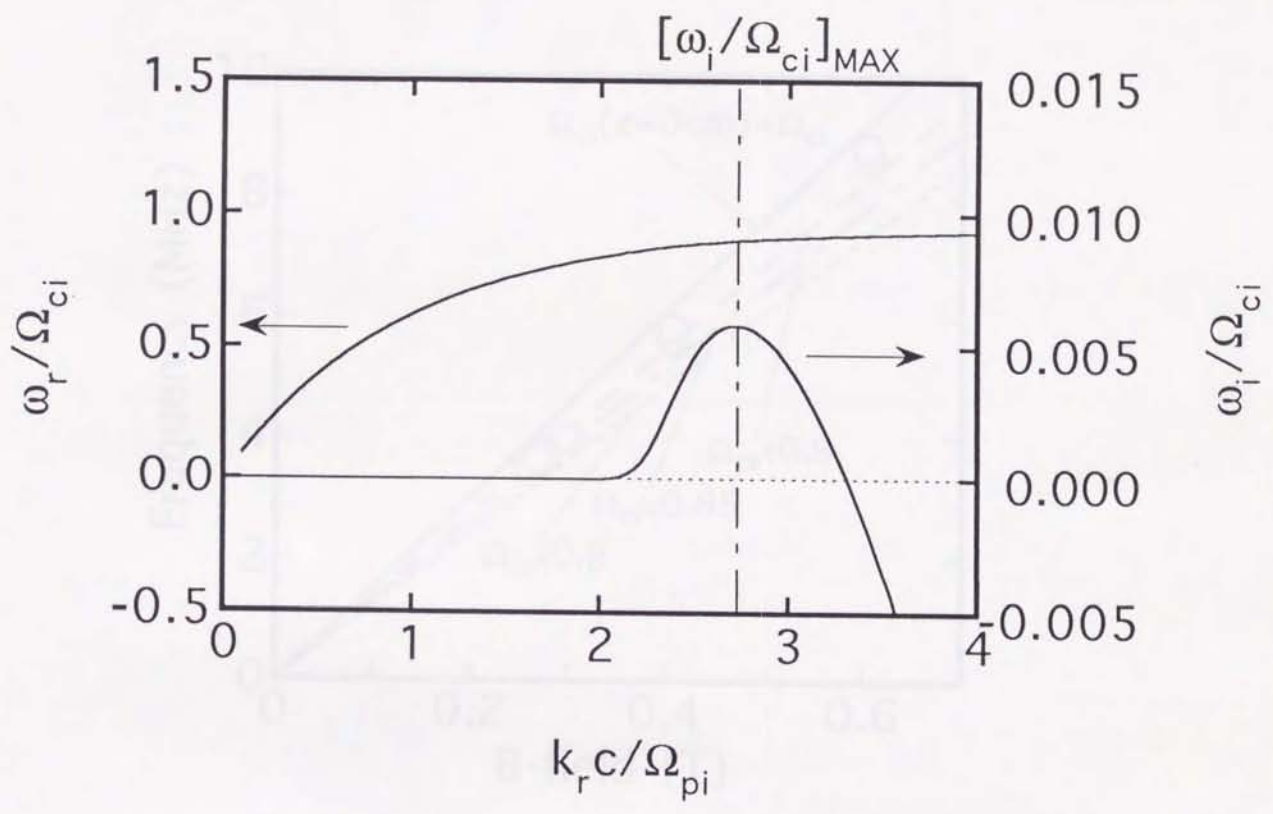


Fig. 4.6

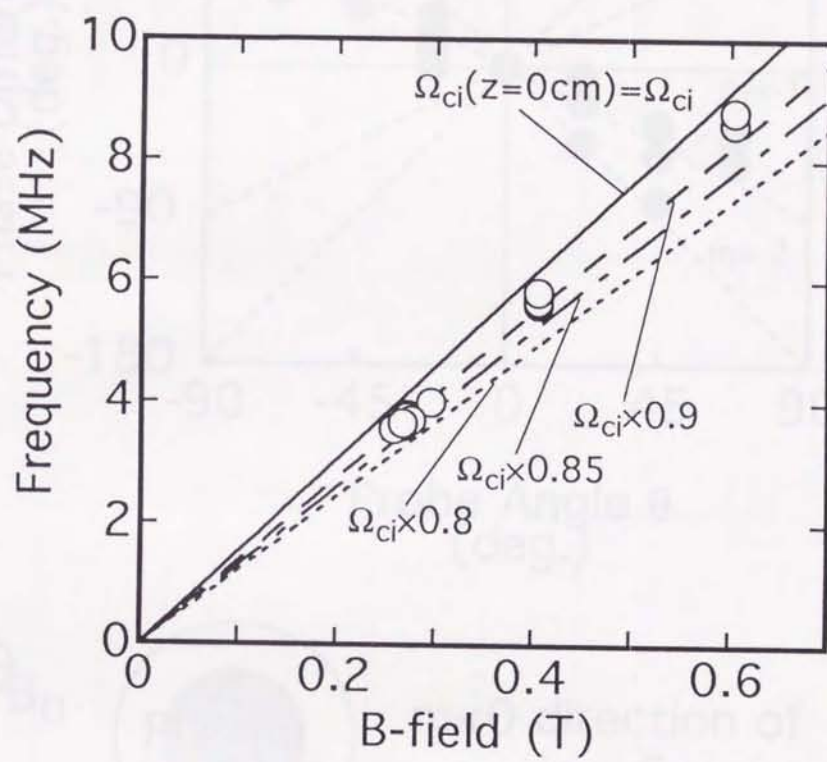


Fig. 4.7

Fig. 4.8

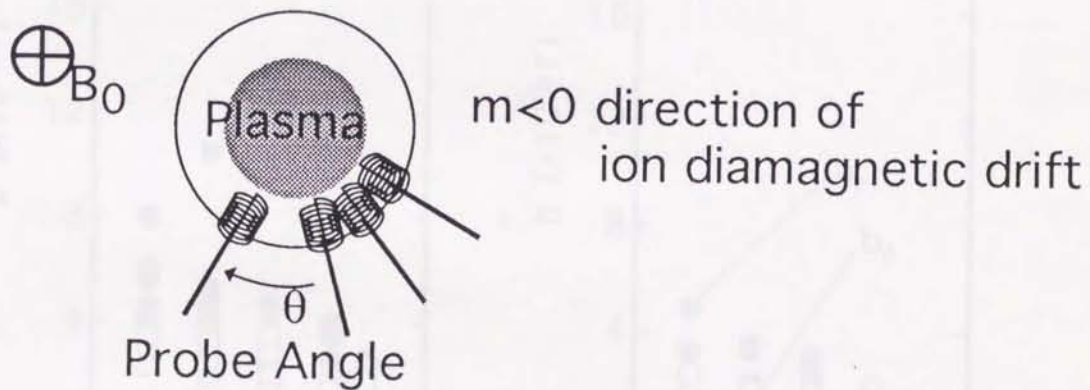
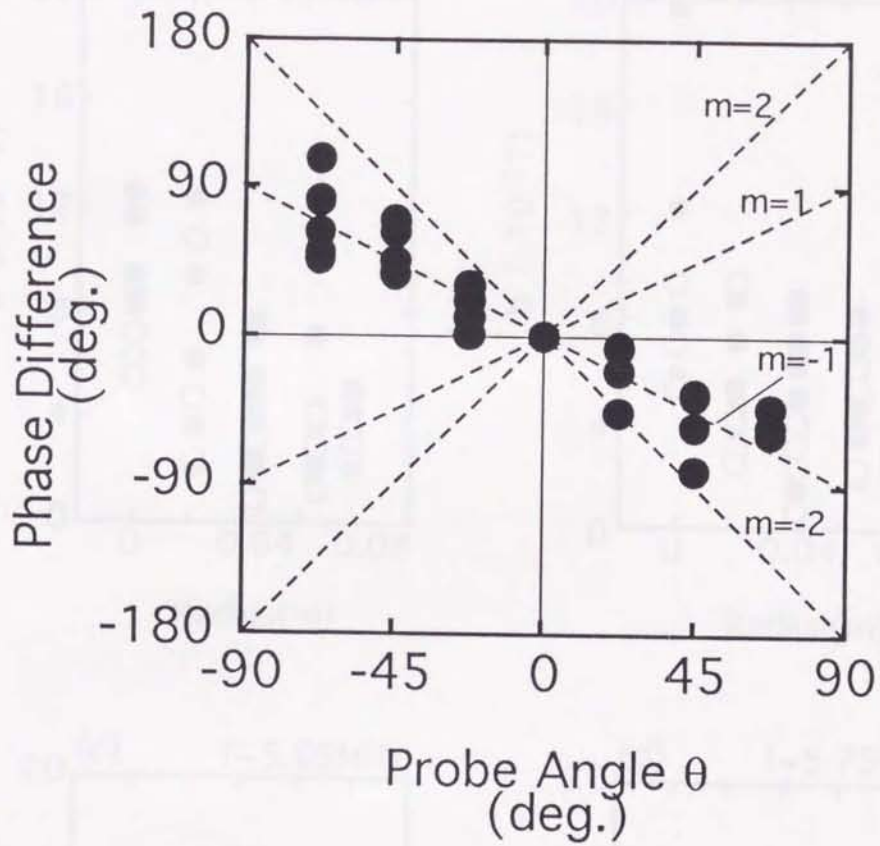


Fig. 4.8

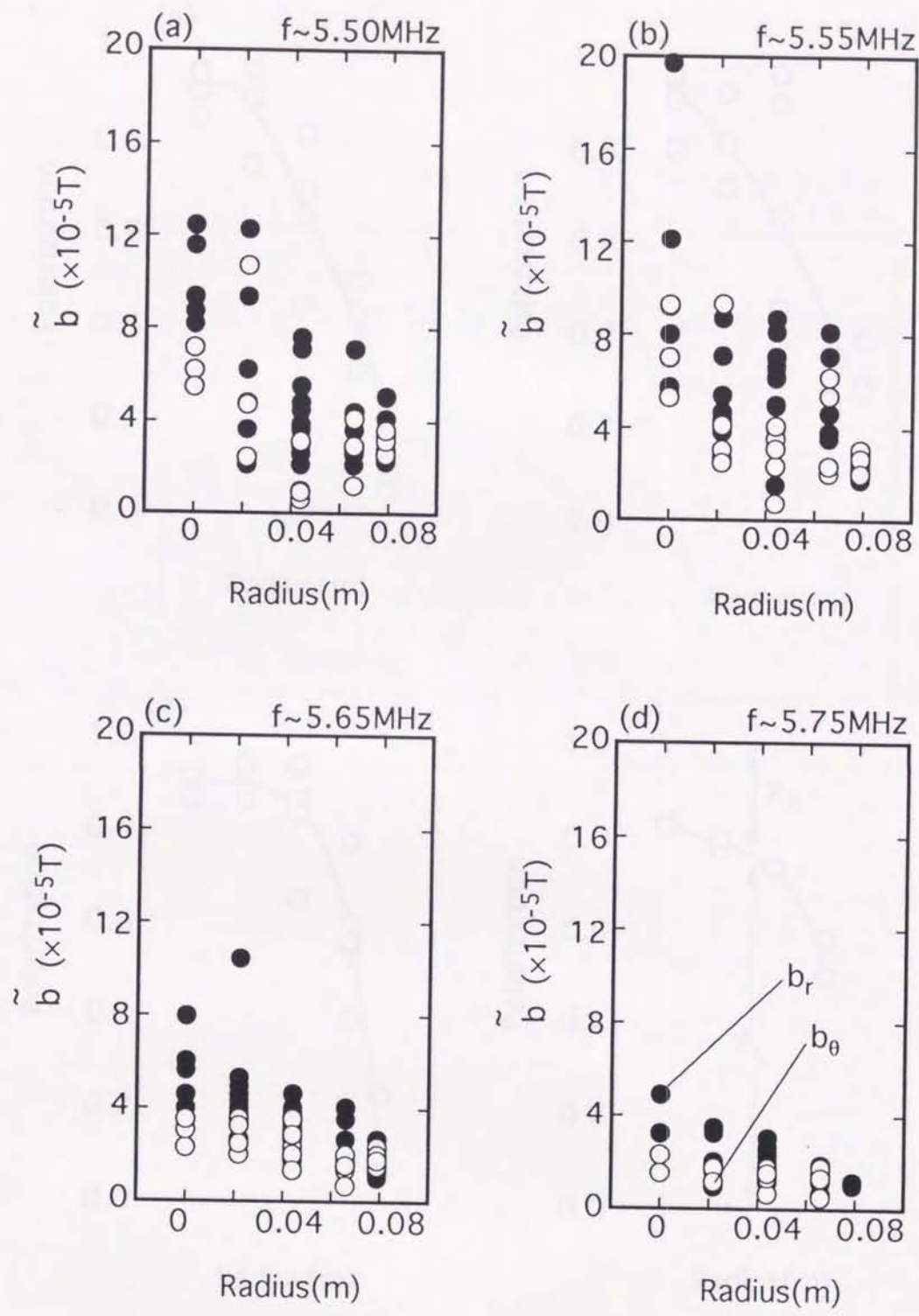


Fig. 4.9

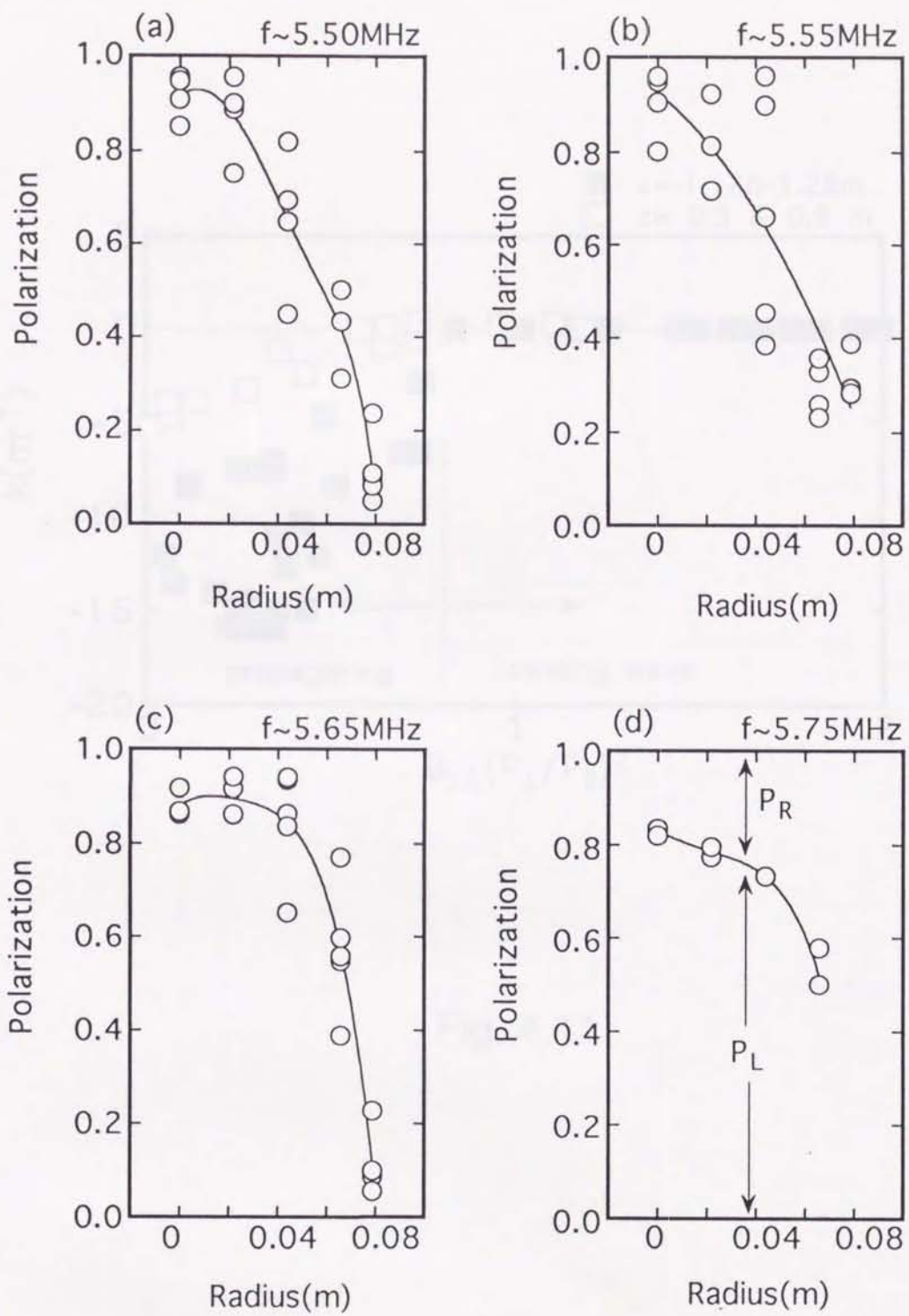


Fig. 4.10

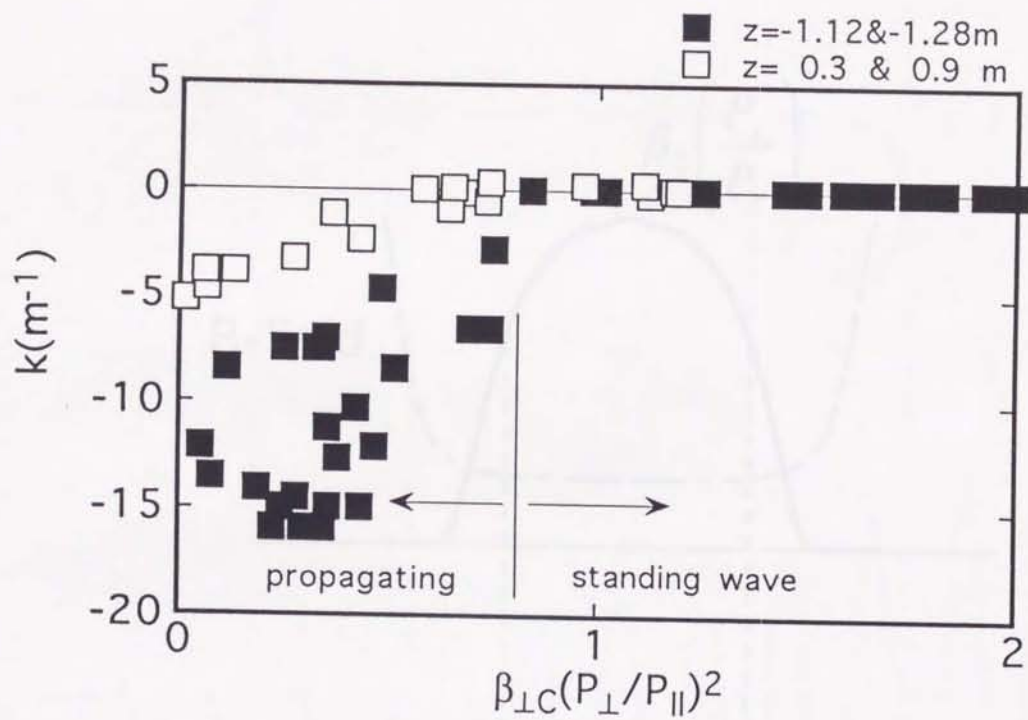


Fig. 4.11

Fig. 4.12

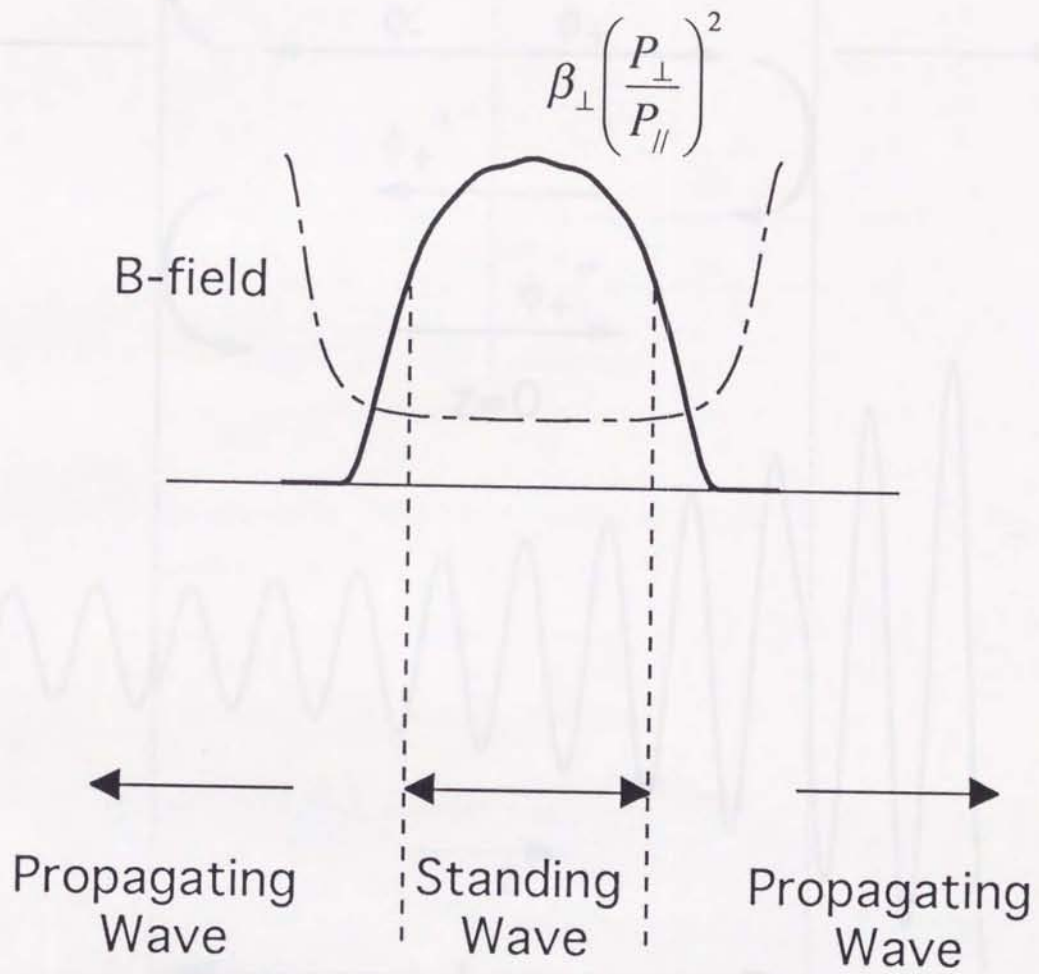
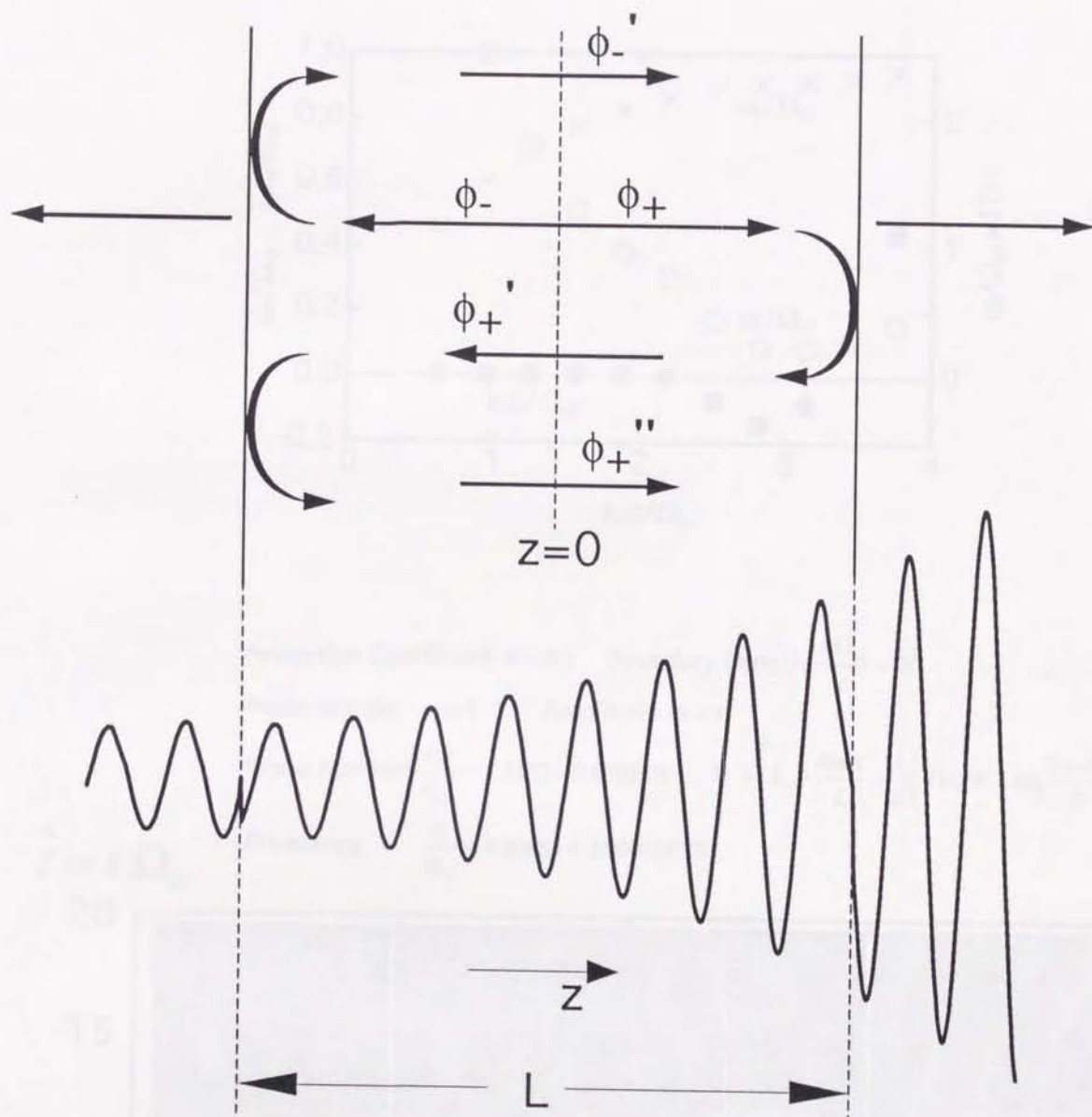


Fig. 4.12

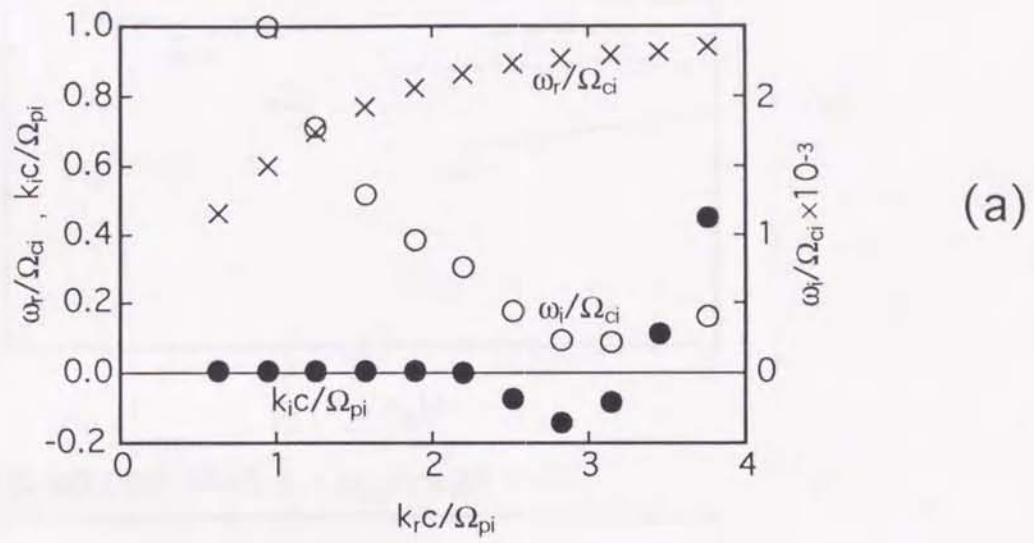
Fig. 4.13



Boundary Condition

$$\phi_+ = \phi_-' + \phi_+''$$

Fig. 4.13



Reflection Coefficient $R = 0.5$ Boundary Length $\frac{L\Omega_{pi}}{c} = 20$
 Mode Number $m = 8$ Amplitude $a = 1$
 Wave Number $\frac{k_+ c}{\Omega_{pi}} = 2.5155 - 0.070388i$, $k_- = \left[k_+, -\frac{4m\pi}{L} - \frac{i}{L} \left(2\log R + \log \frac{3+\sqrt{5}}{2} \right) \right]$
 Frequency $\frac{\omega}{\Omega_{ci}} = 0.89063 + 0.00043832i$

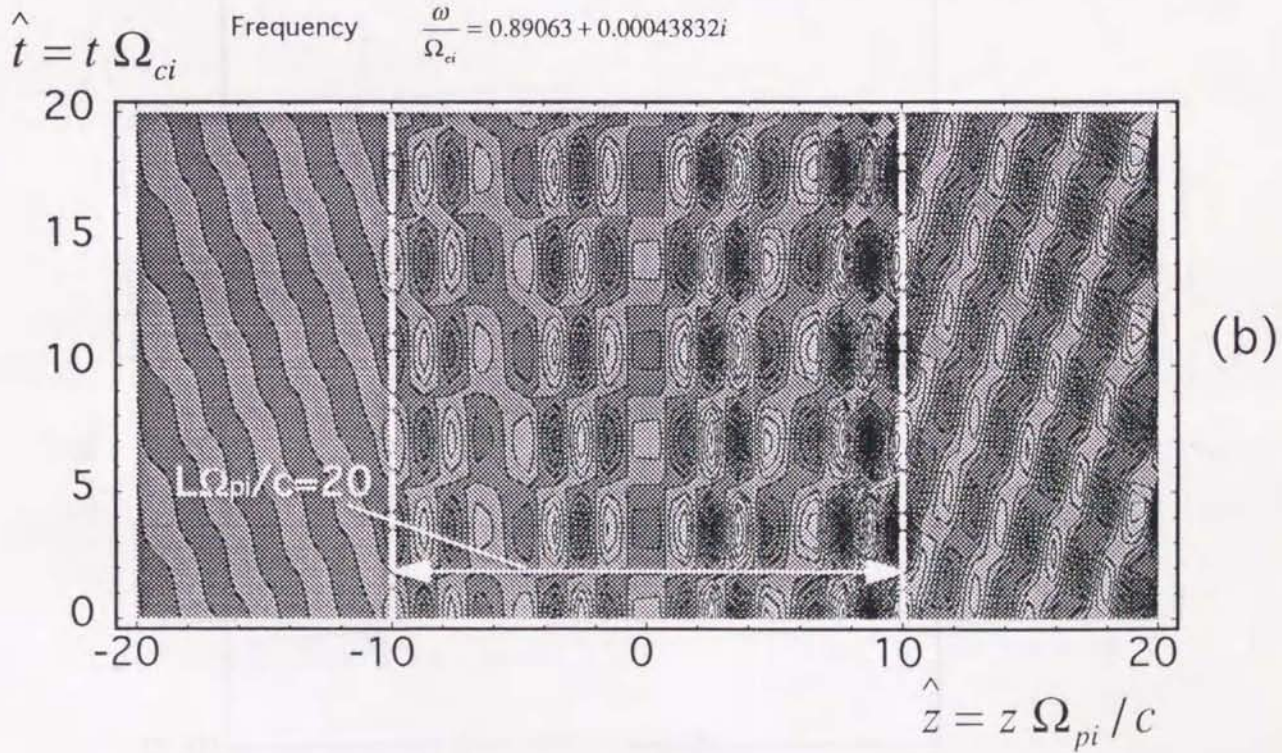


Fig. 4.14

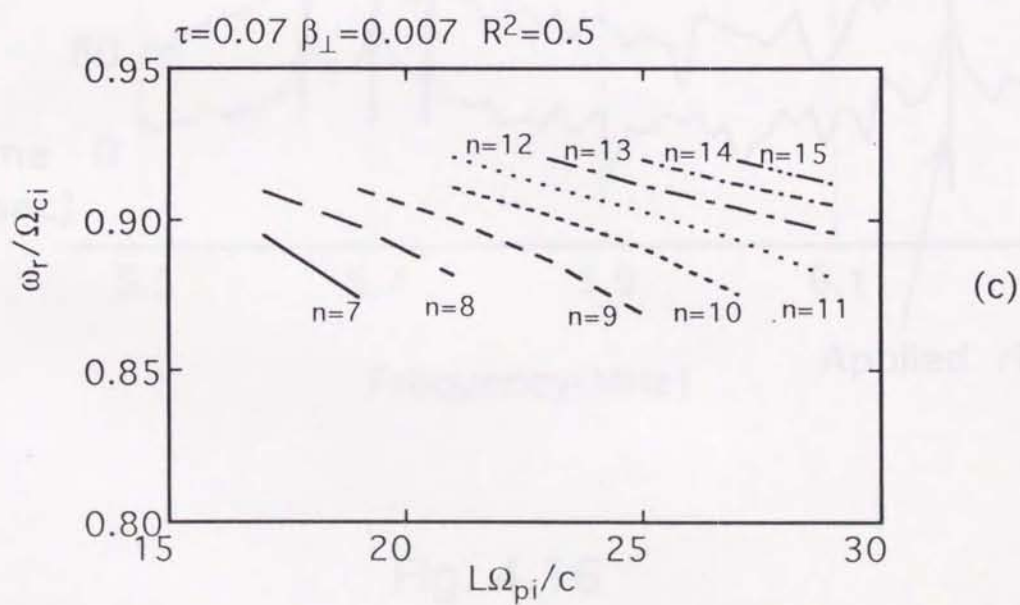
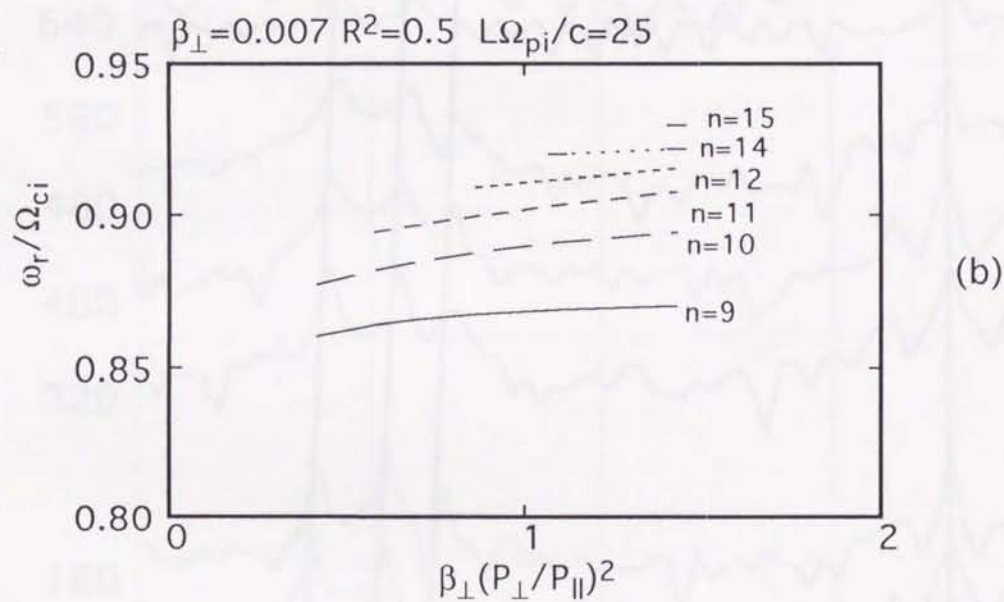
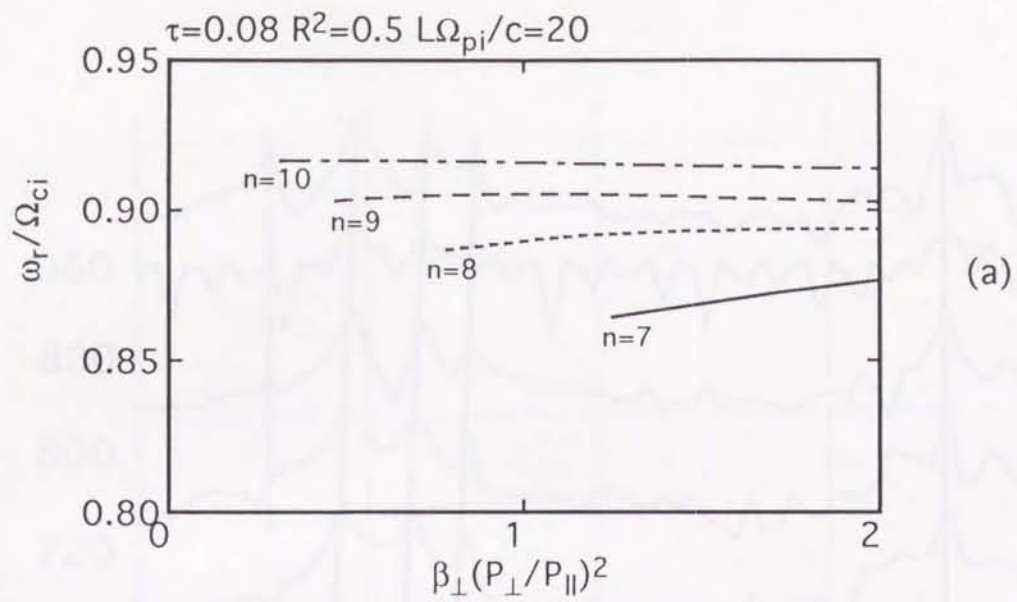


Fig. 4.15

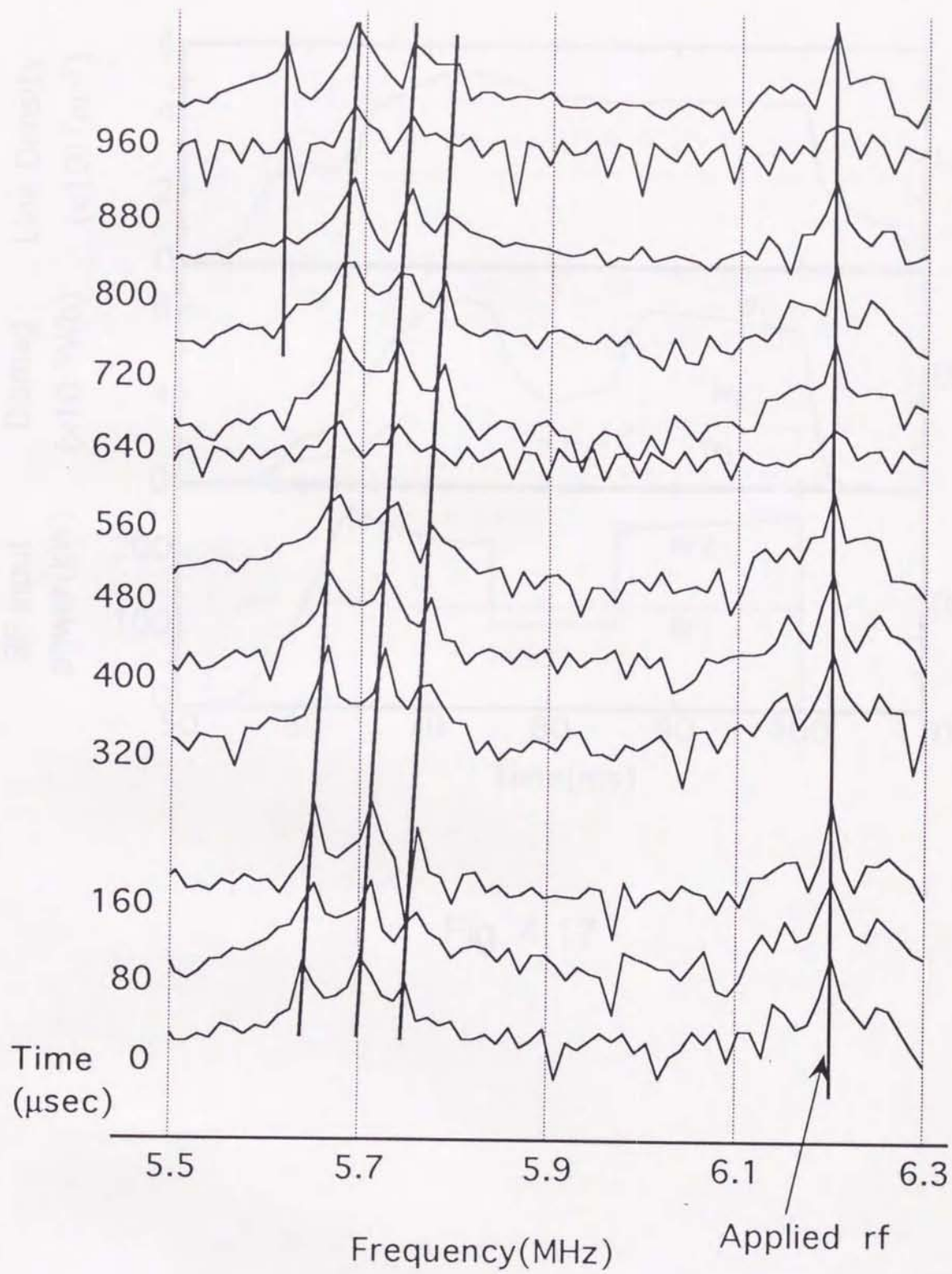


Fig. 4.16

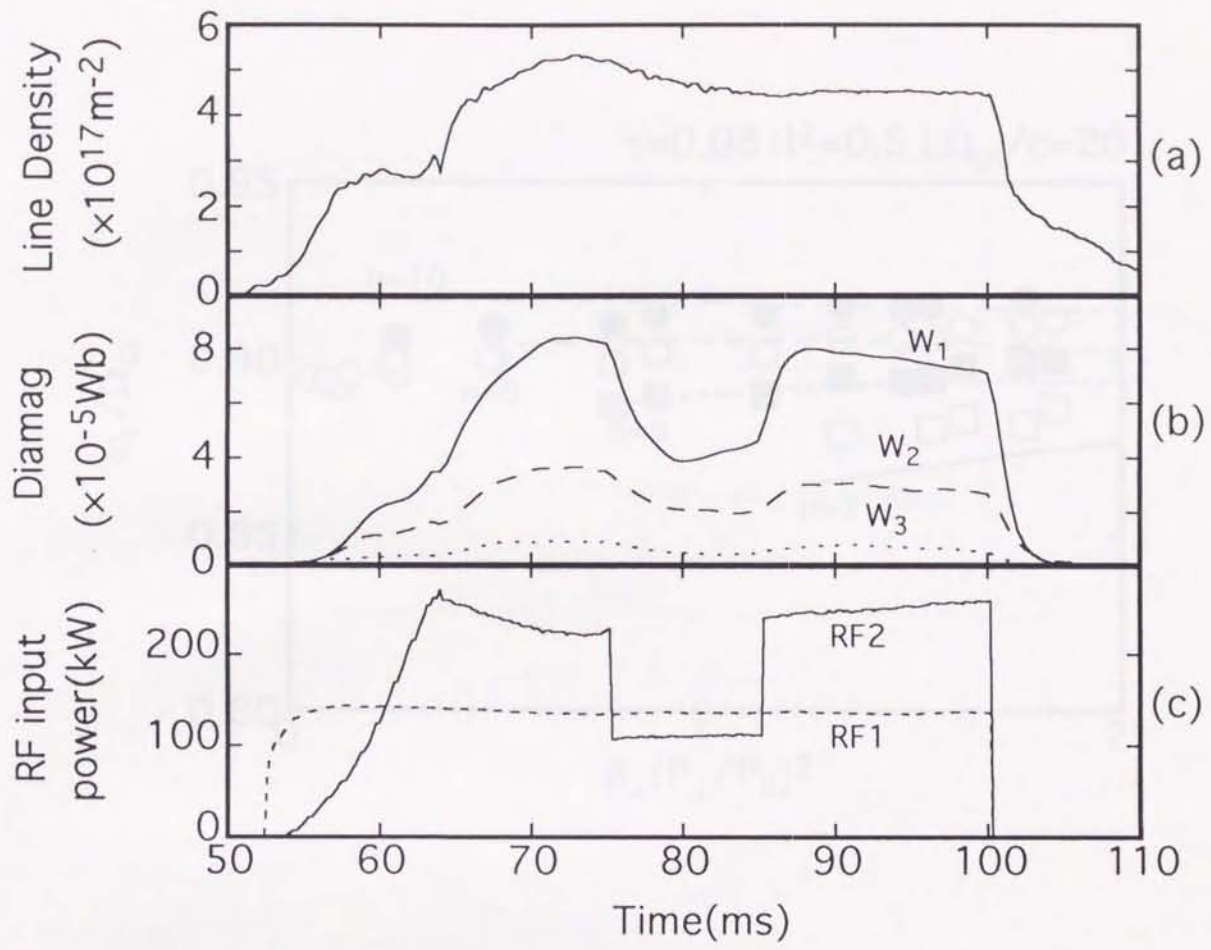


Fig. 4.17

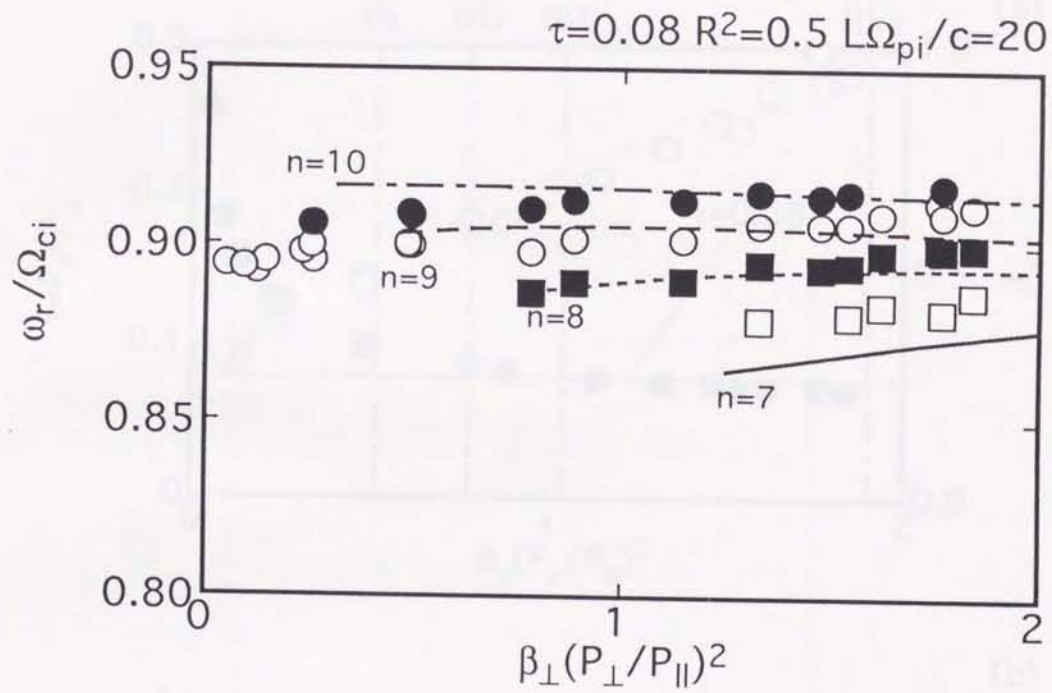


Fig. 4.18

Fig. 4.19

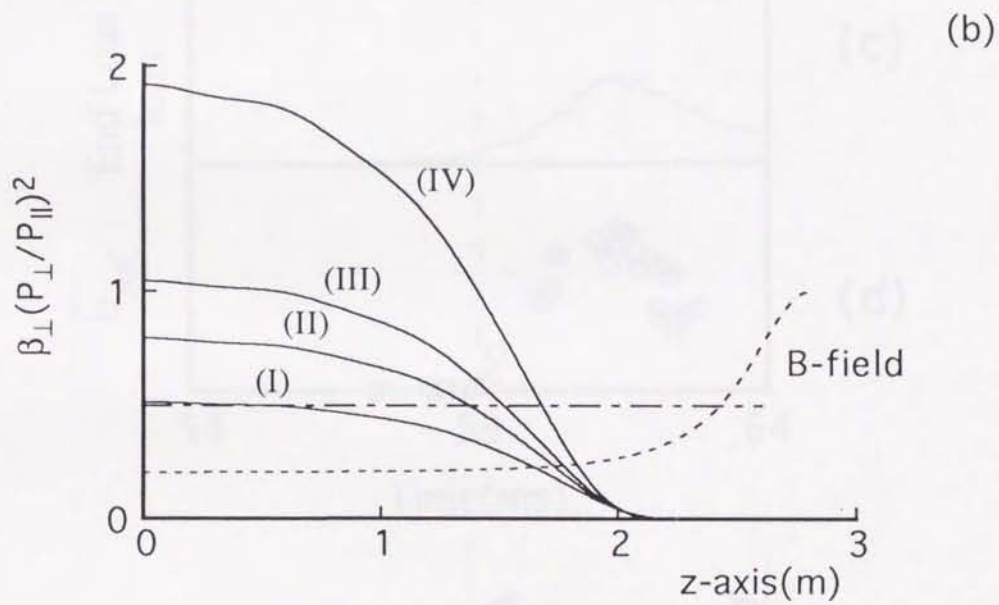
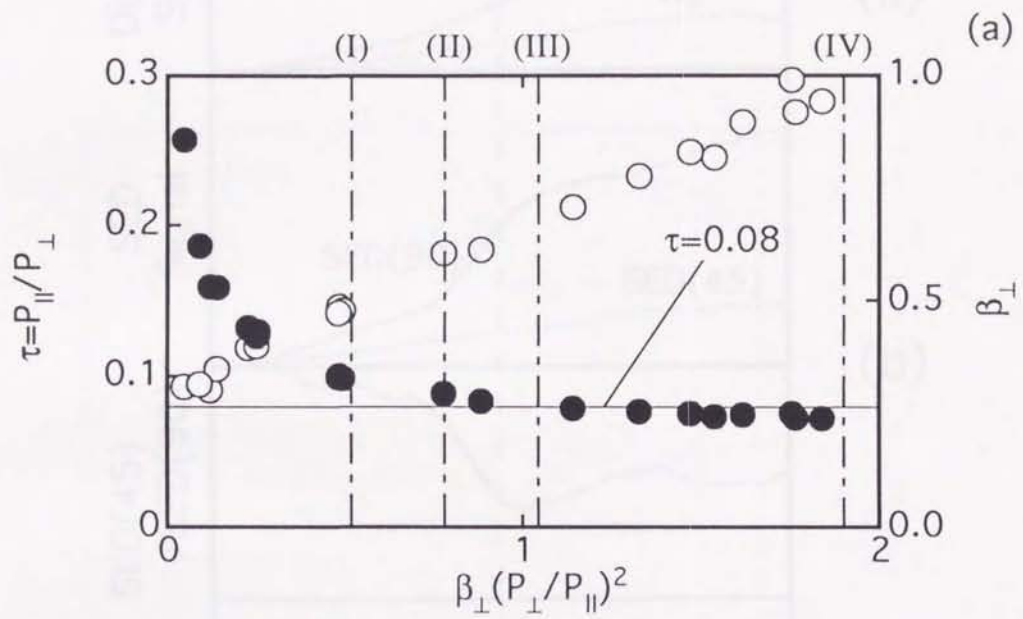


Fig. 4.19

Fig. 4.20

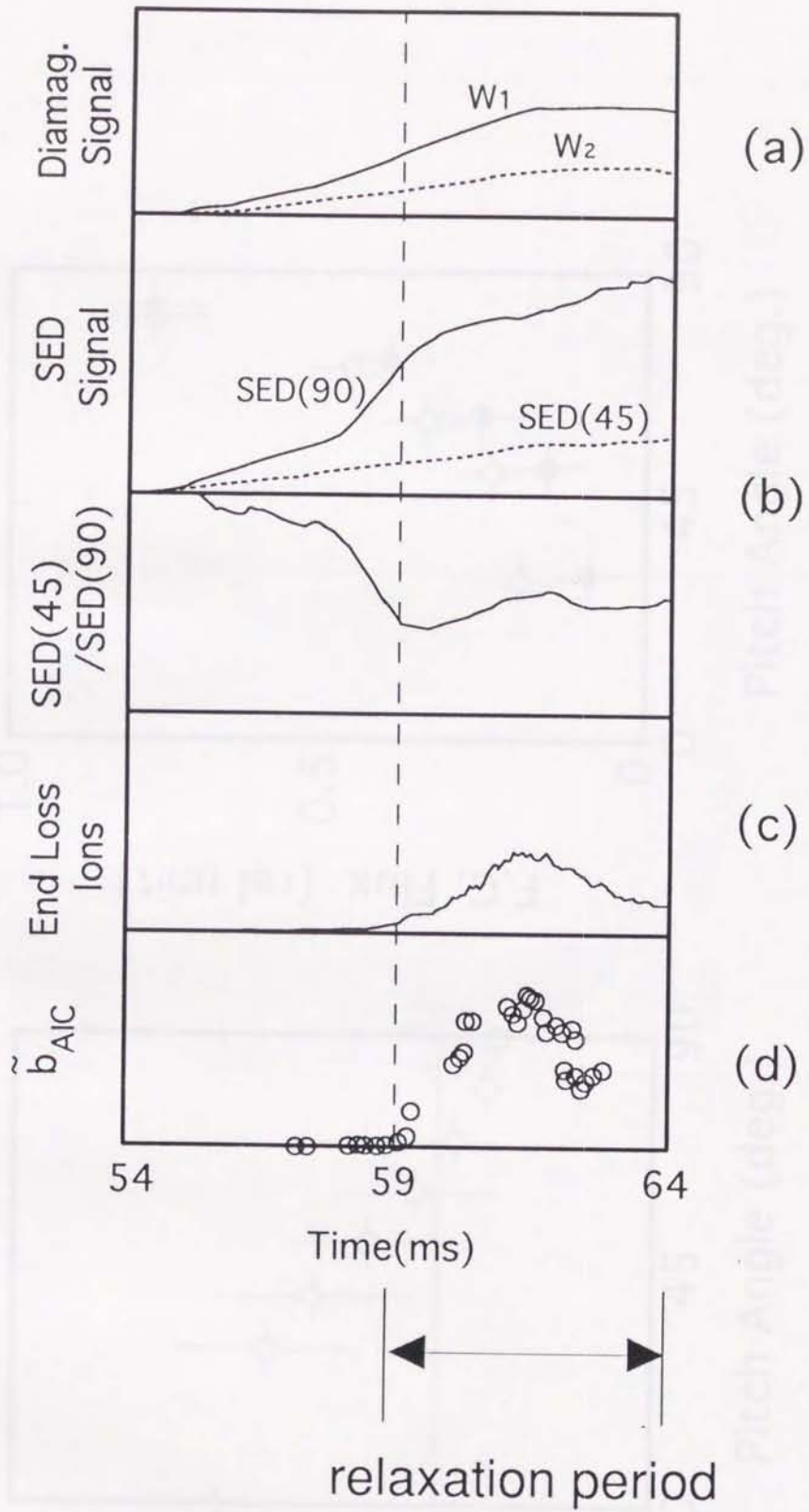


Fig. 4.20

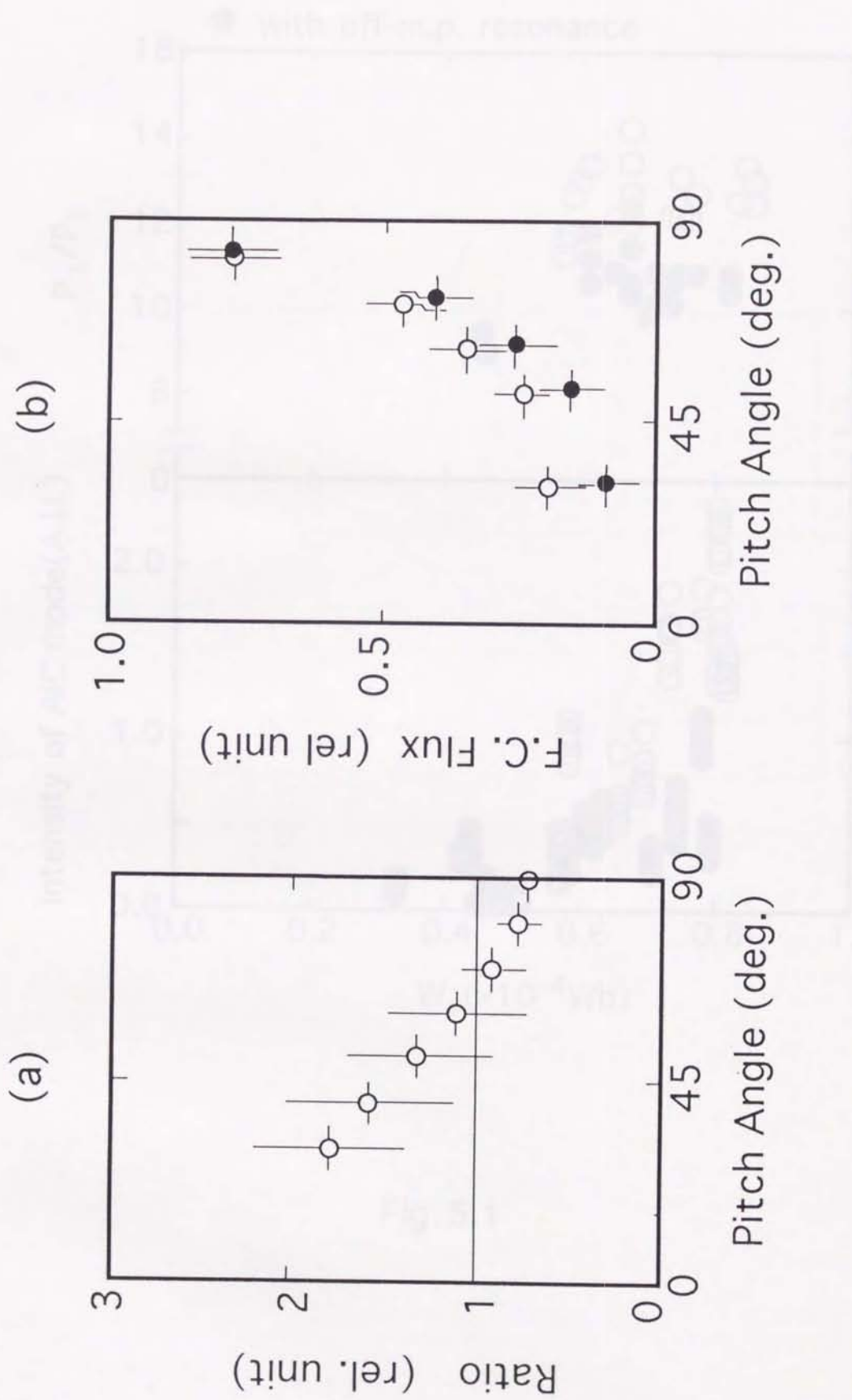


Fig. 4.21

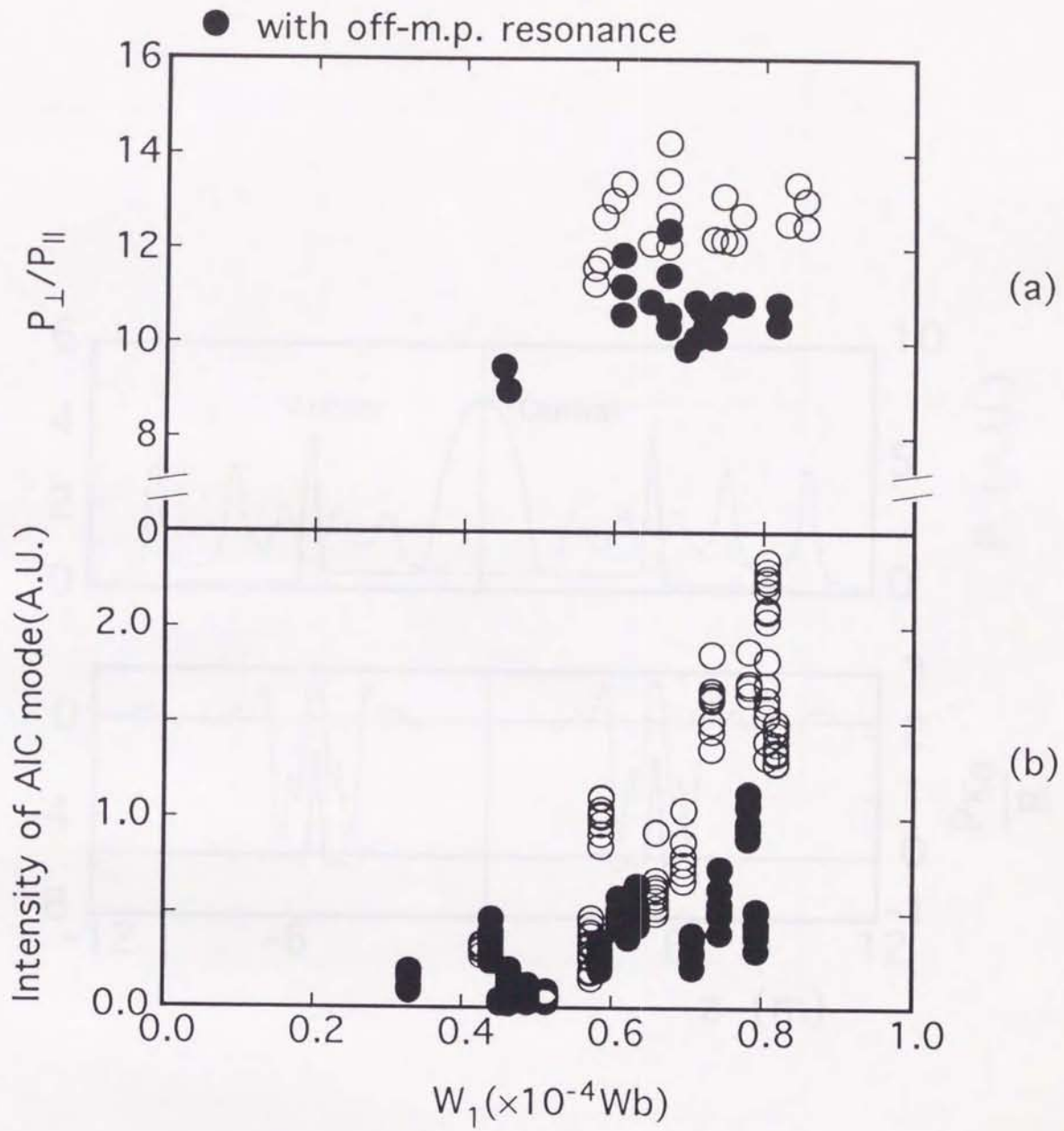


Fig. 5.1

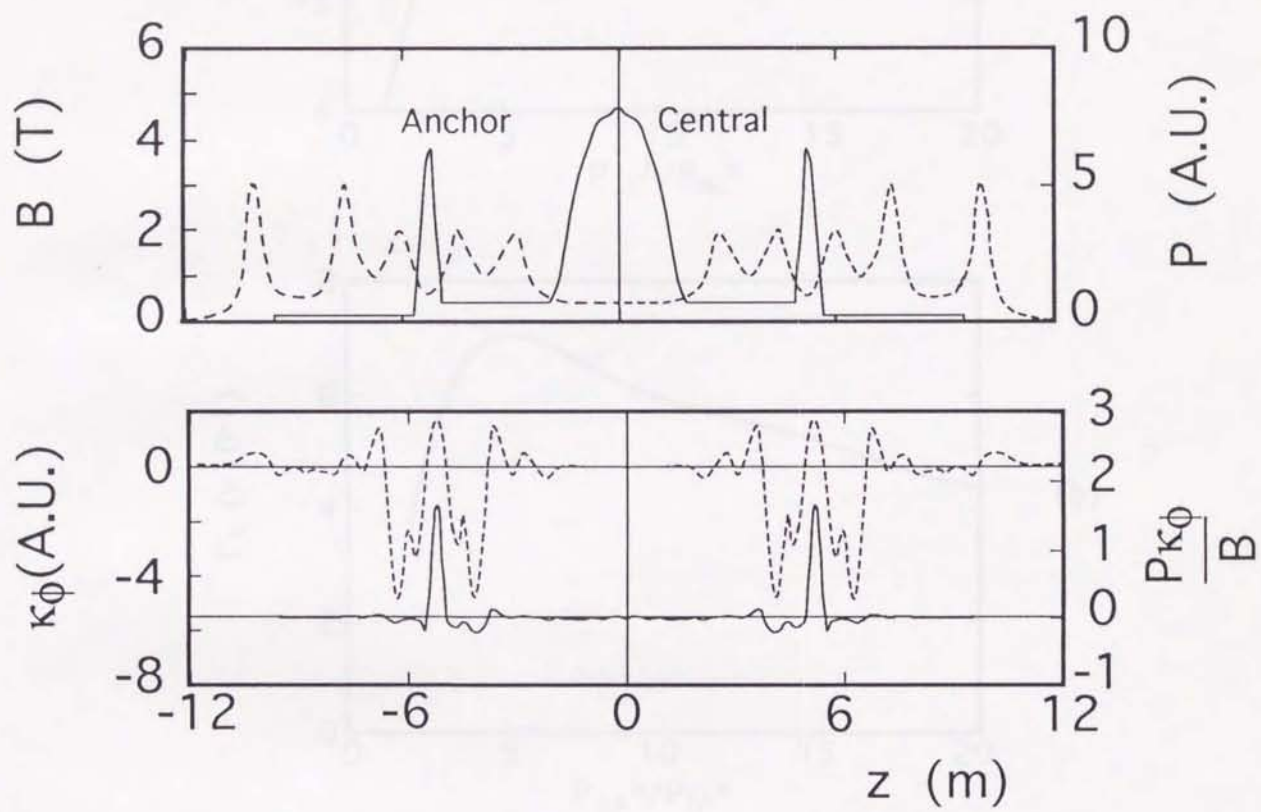


Fig. 5.2

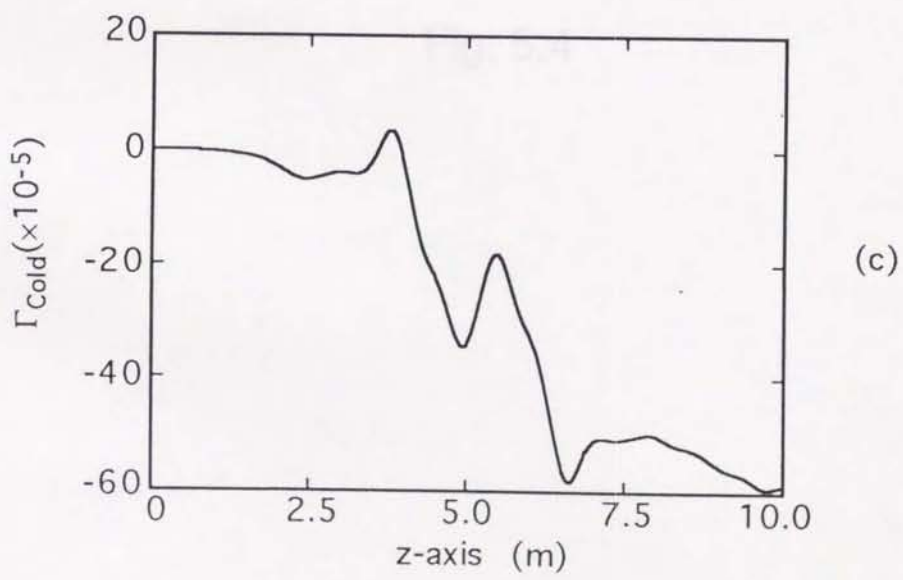
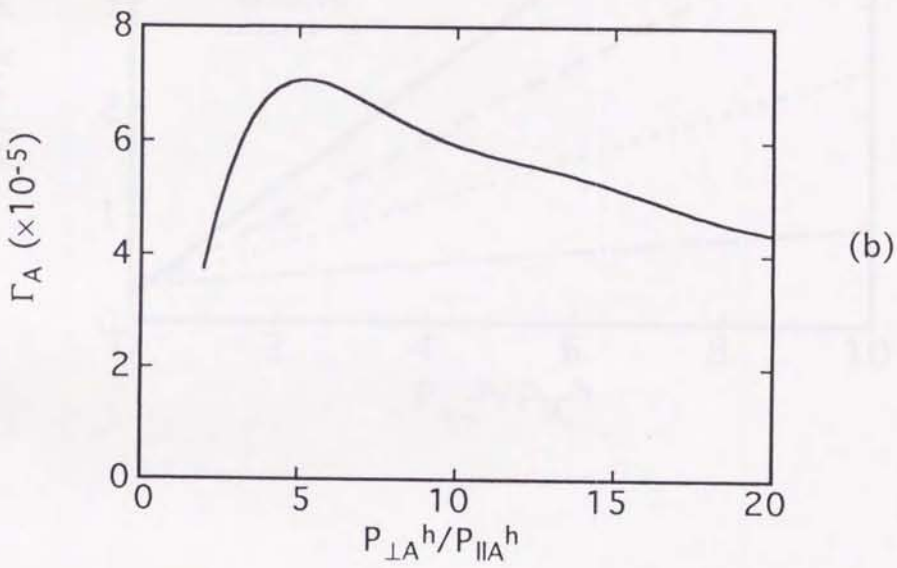
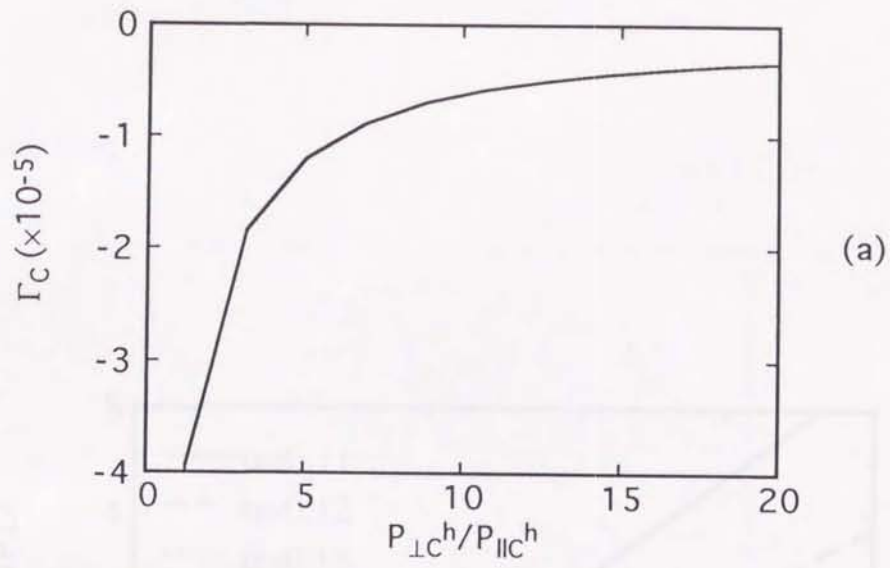


Fig. 5.3

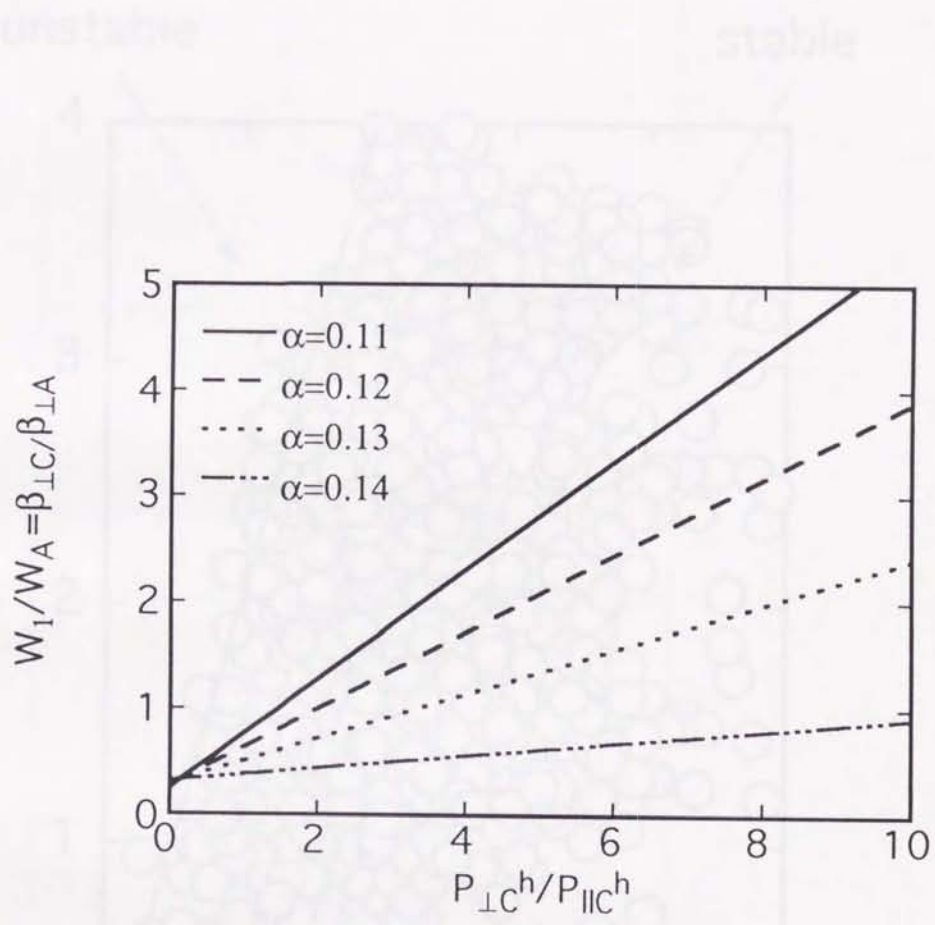


Fig. 5.4

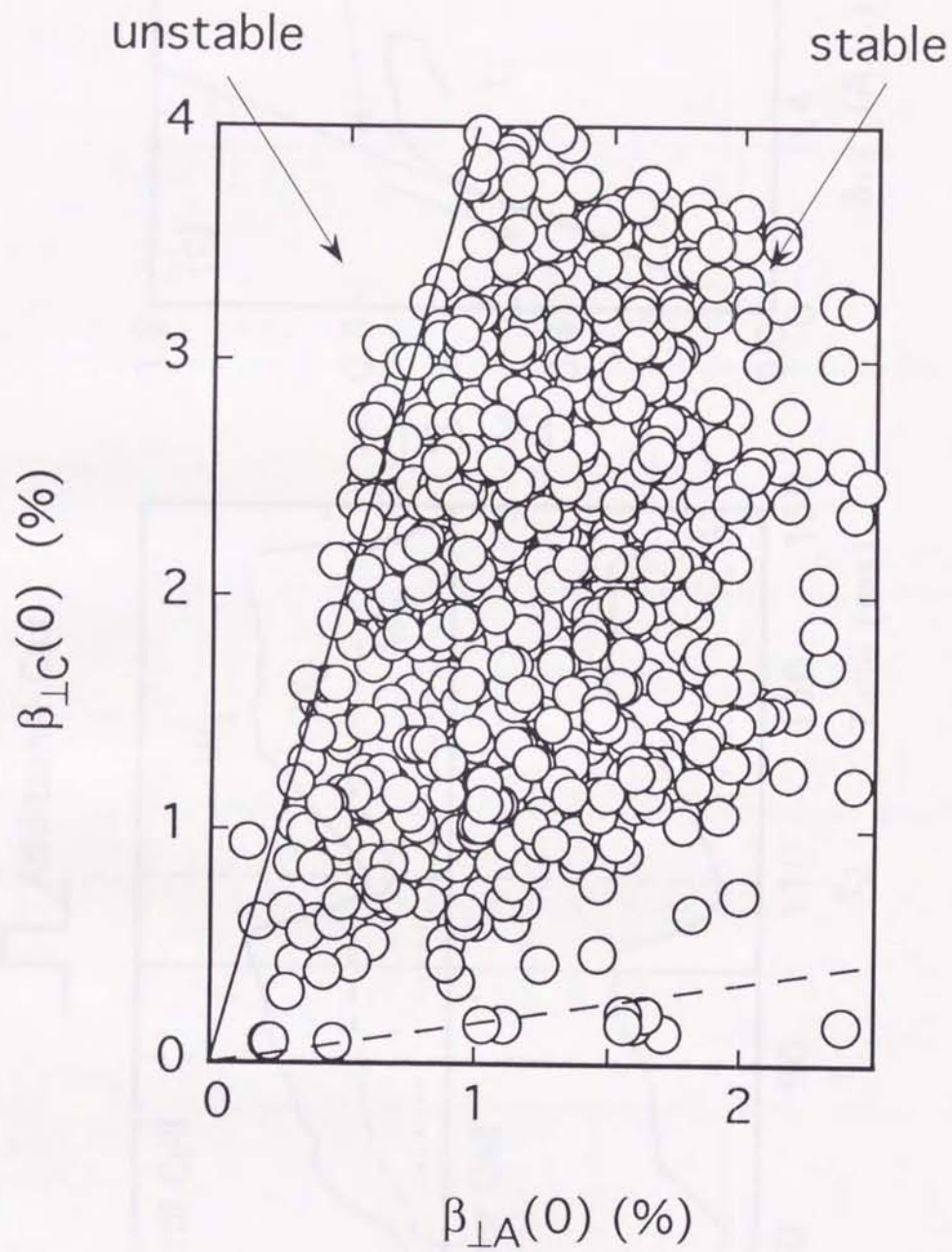


Fig. 5.5

Additional Gas

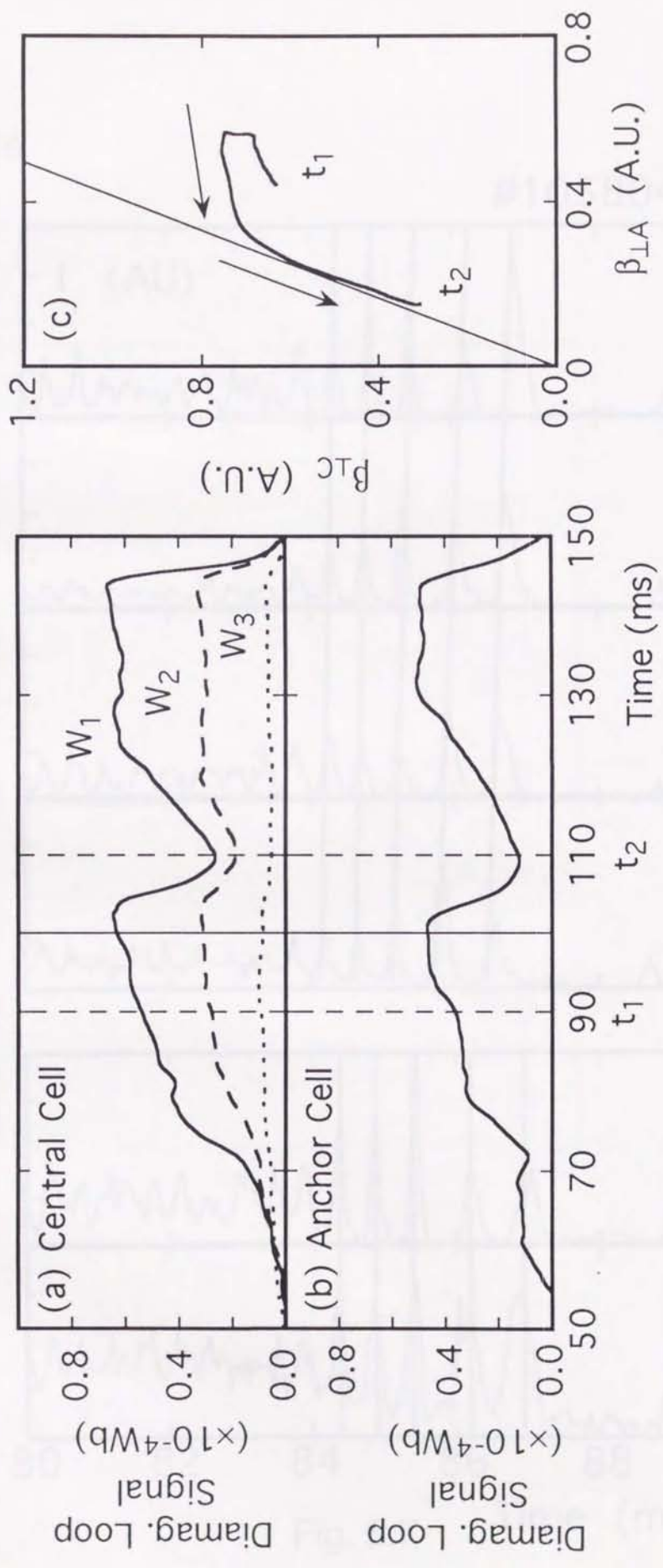



Fig. 5.6

E.S. Probe
Position

#105804

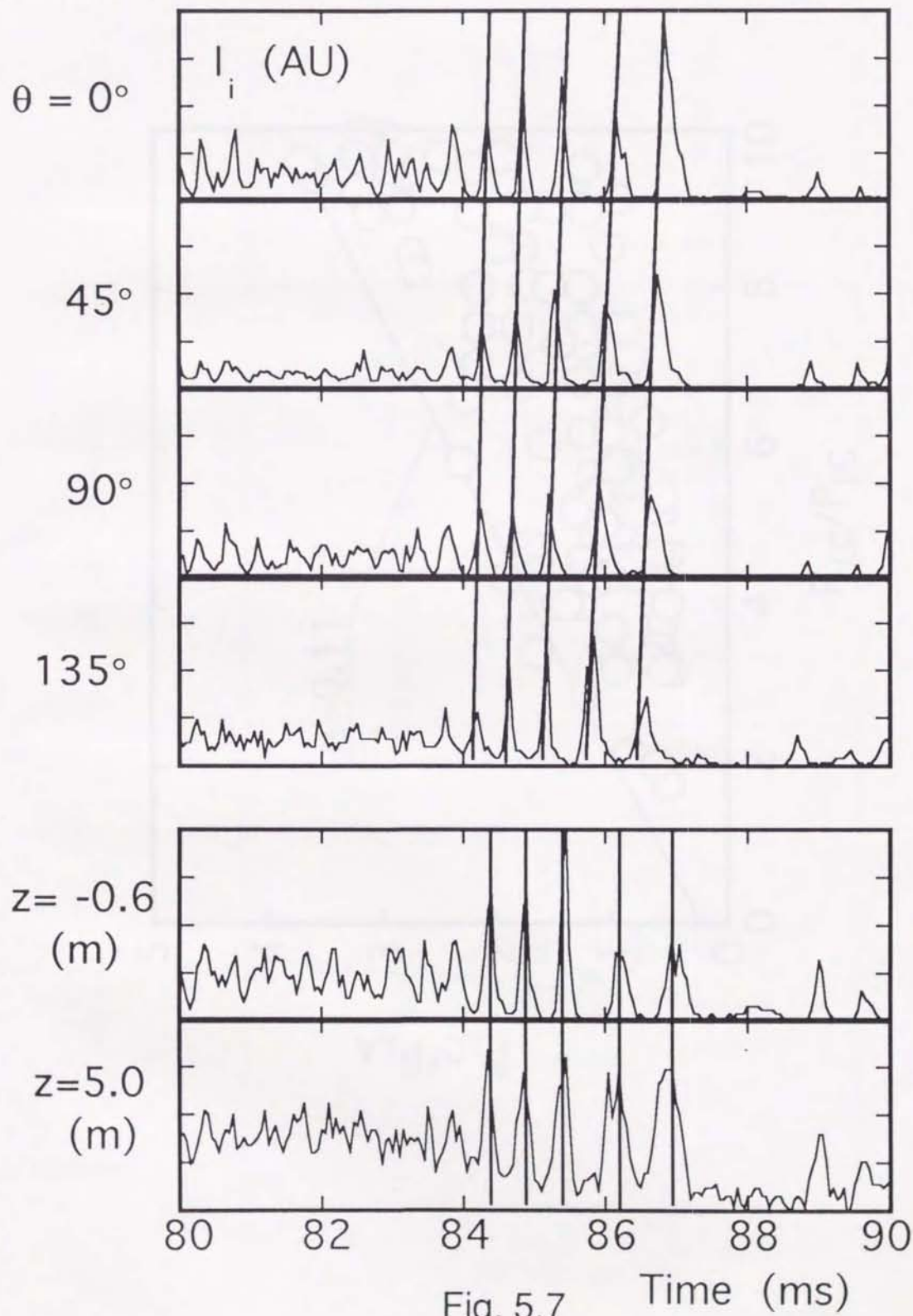


Fig. 5.7

Time (ms)

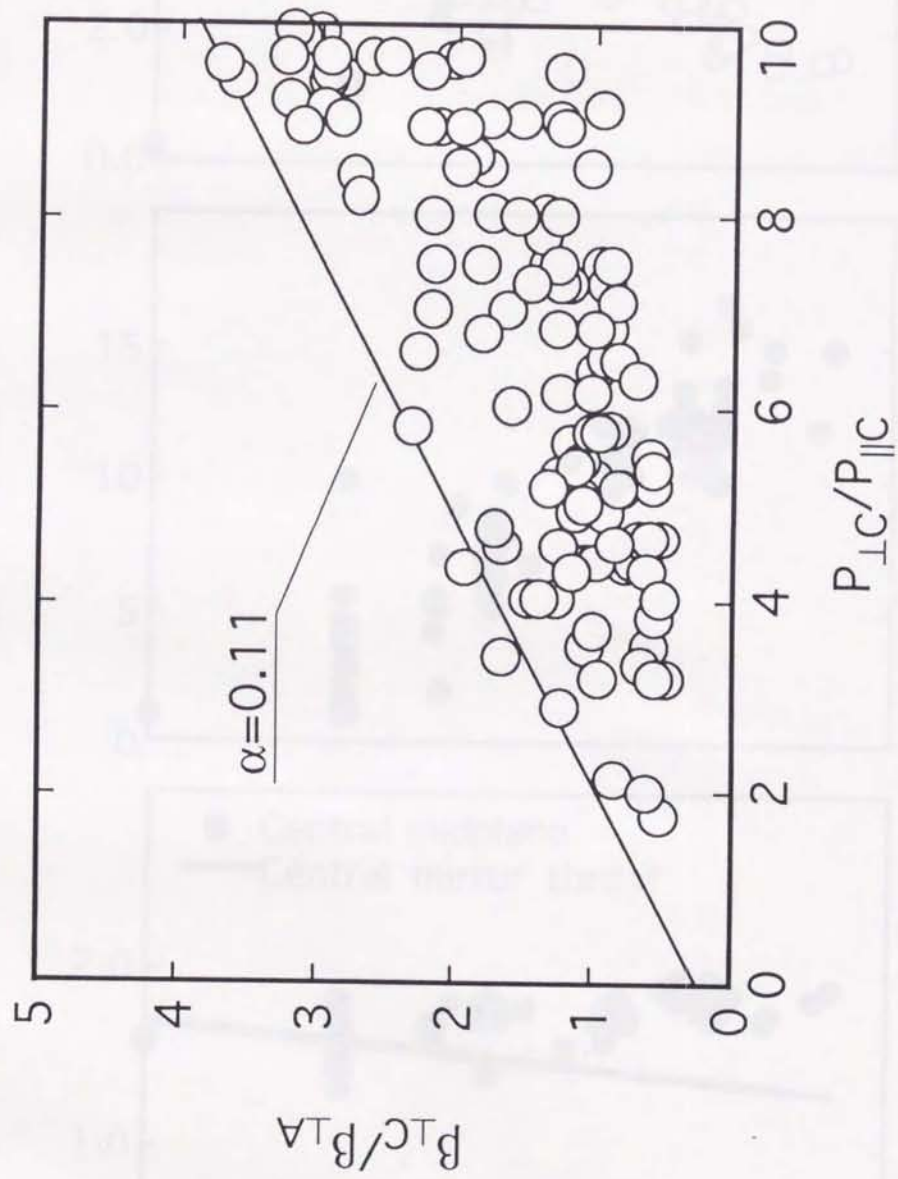


Fig. 5.8

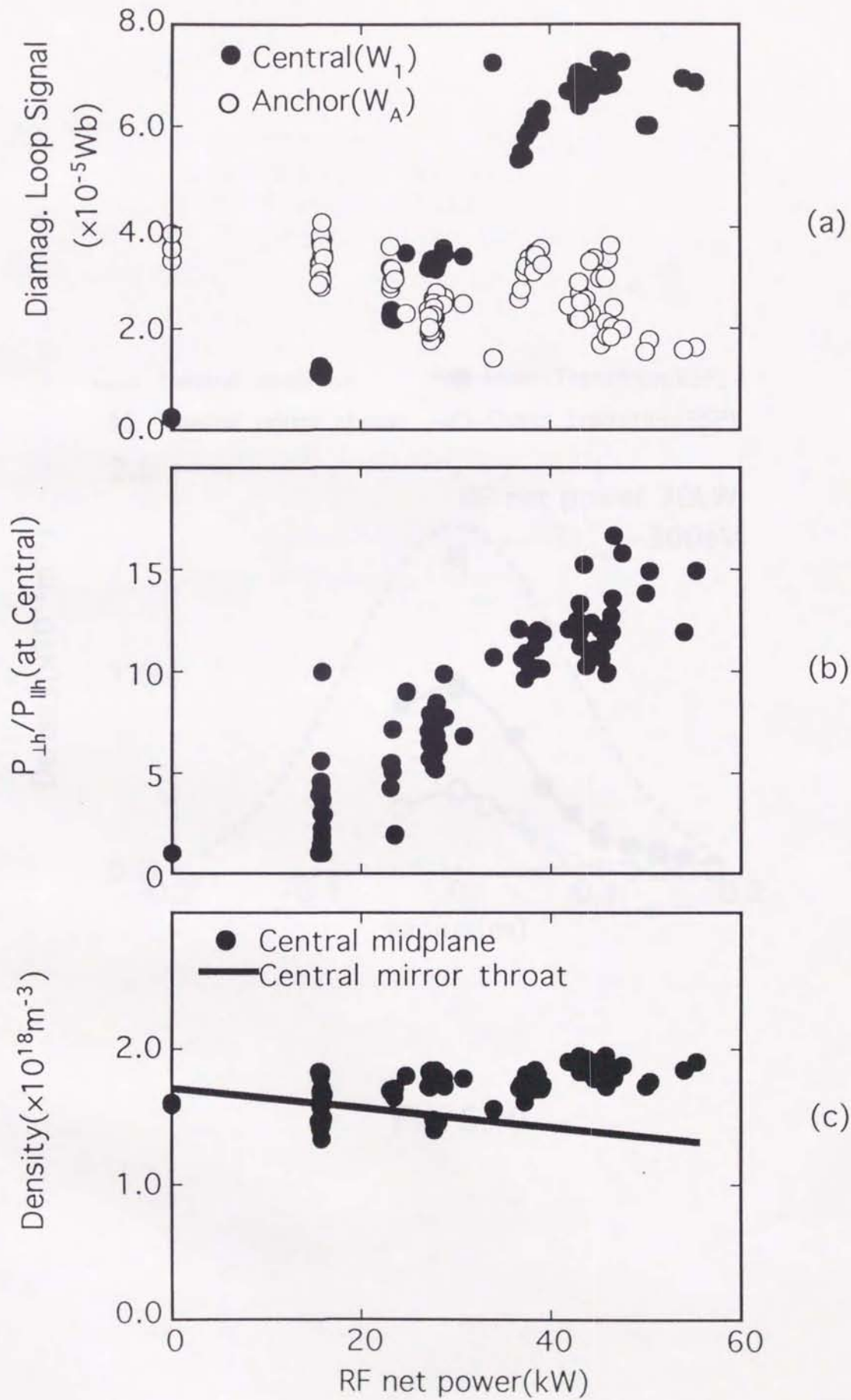


Fig. 5.9

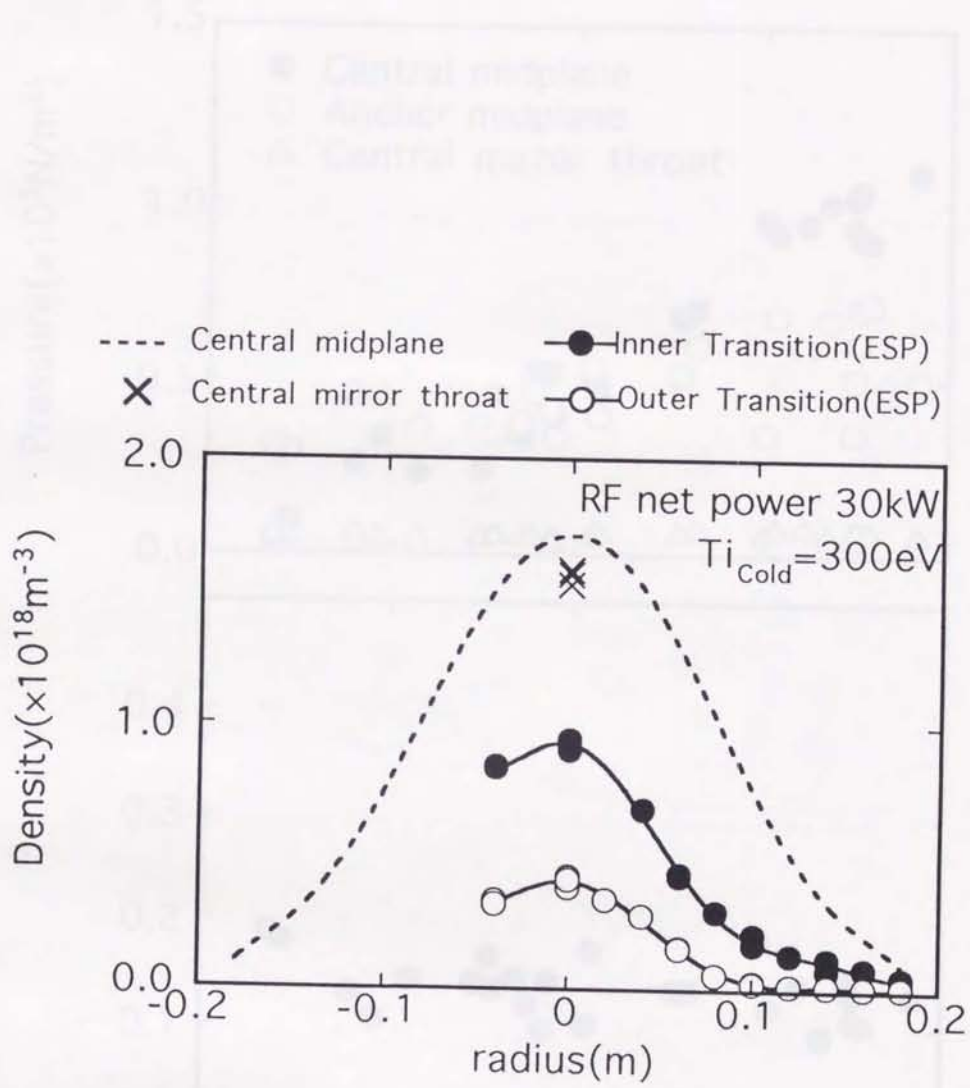


Fig. 5.10

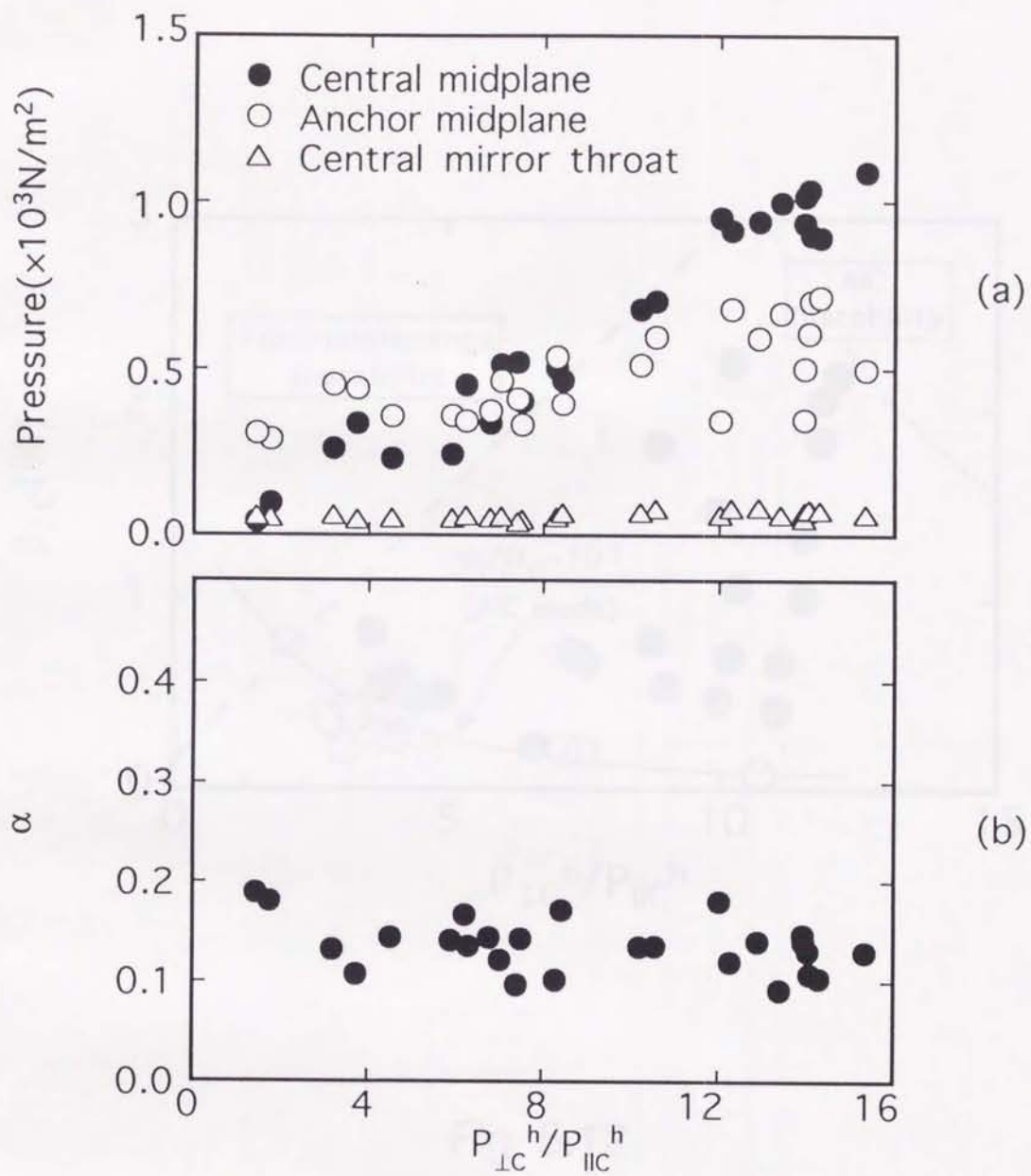


Fig. 5.11

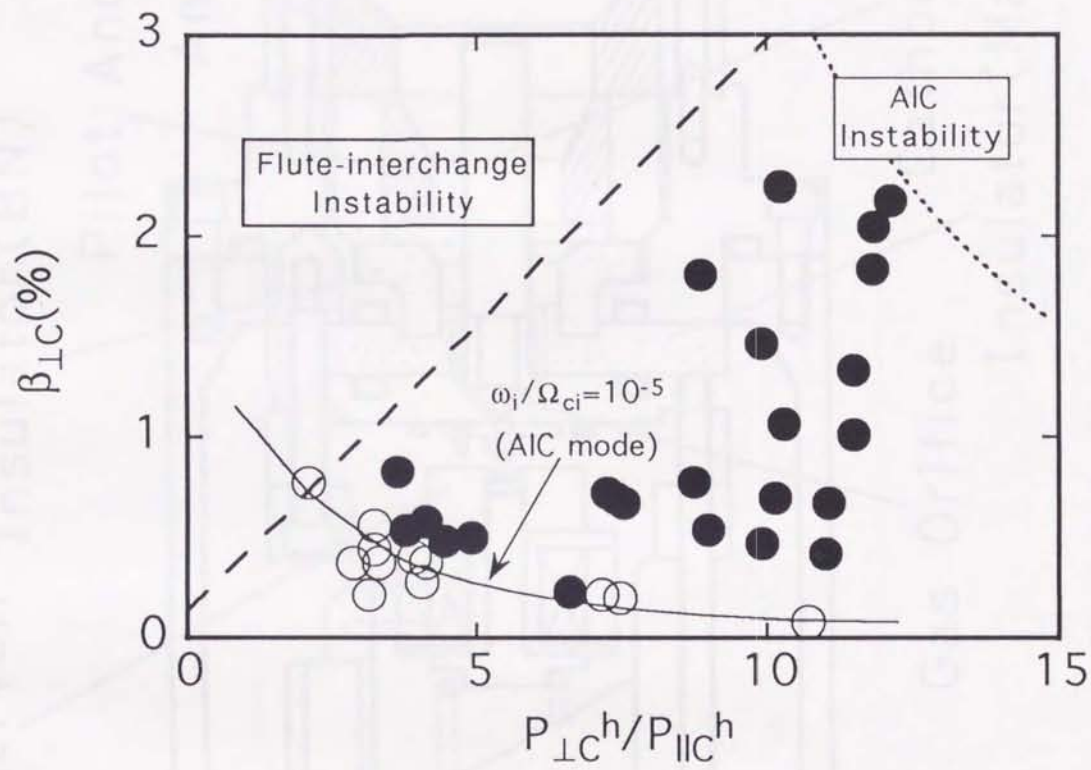


Fig. 5.12

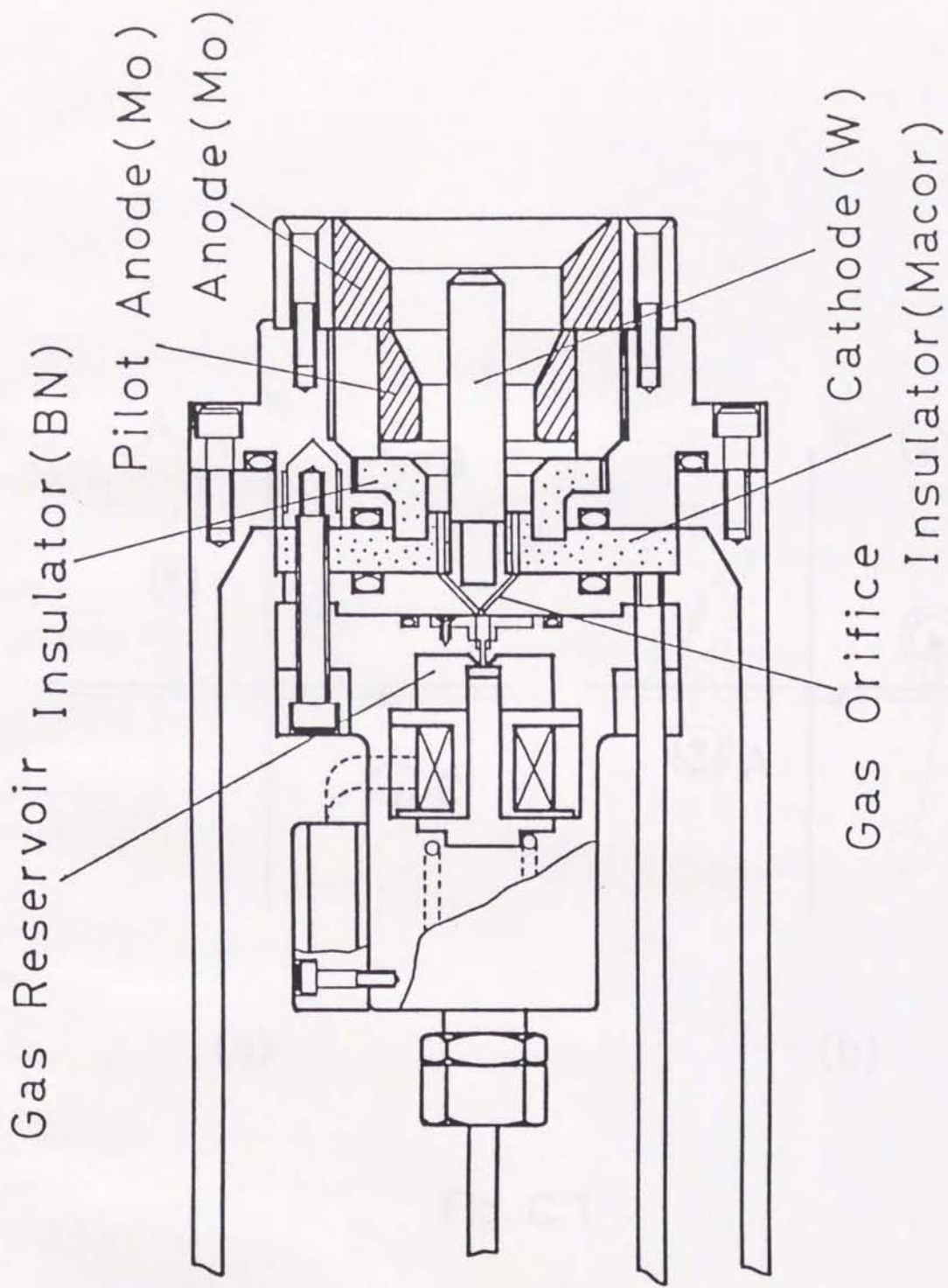
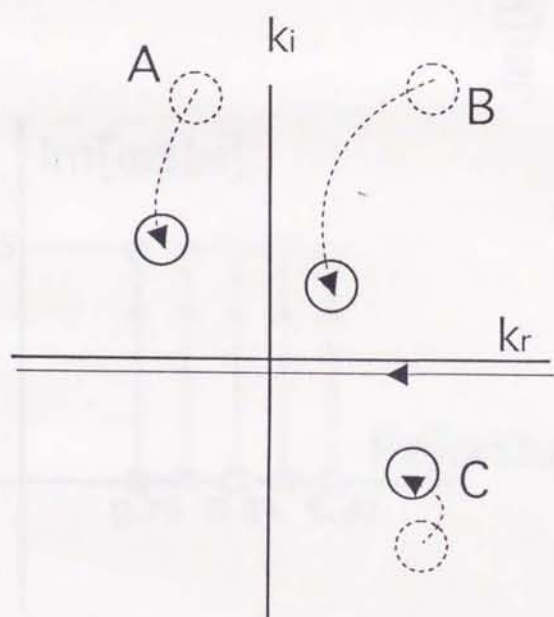
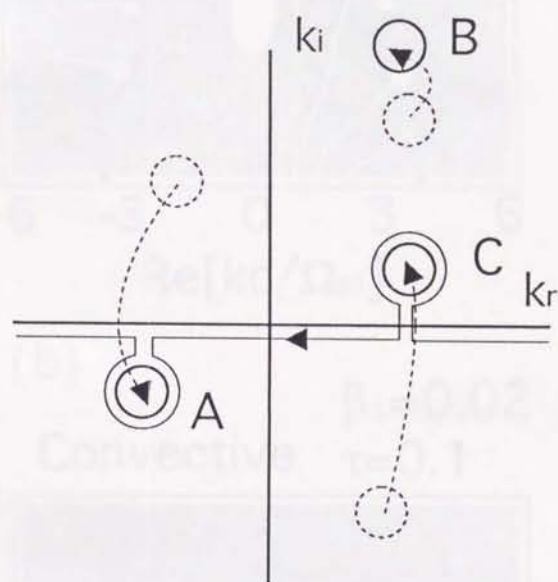


Fig. A.1

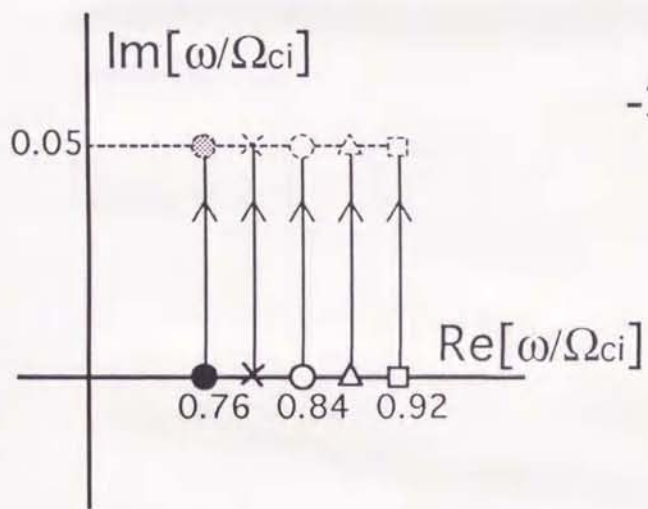


(a)



(b)

Fig. C.1



$\varphi=0.001$
 $\omega/\Omega_{ci}=(0.88,0.02)$

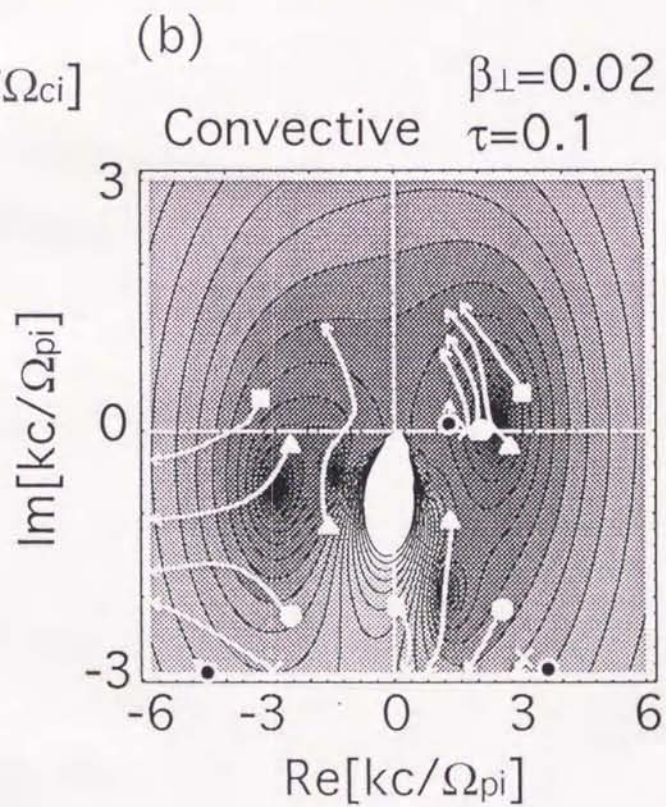
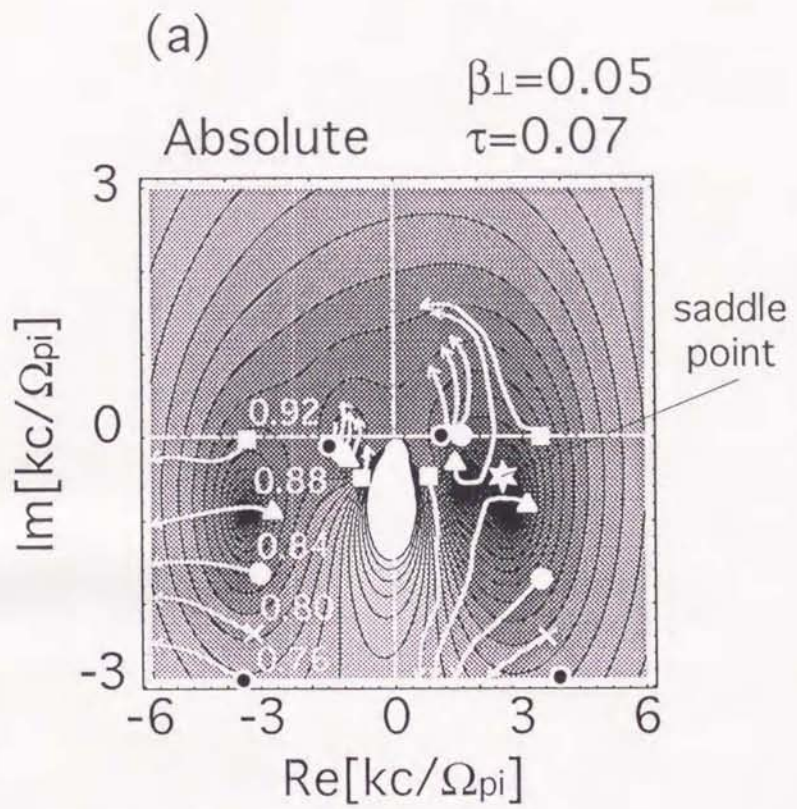
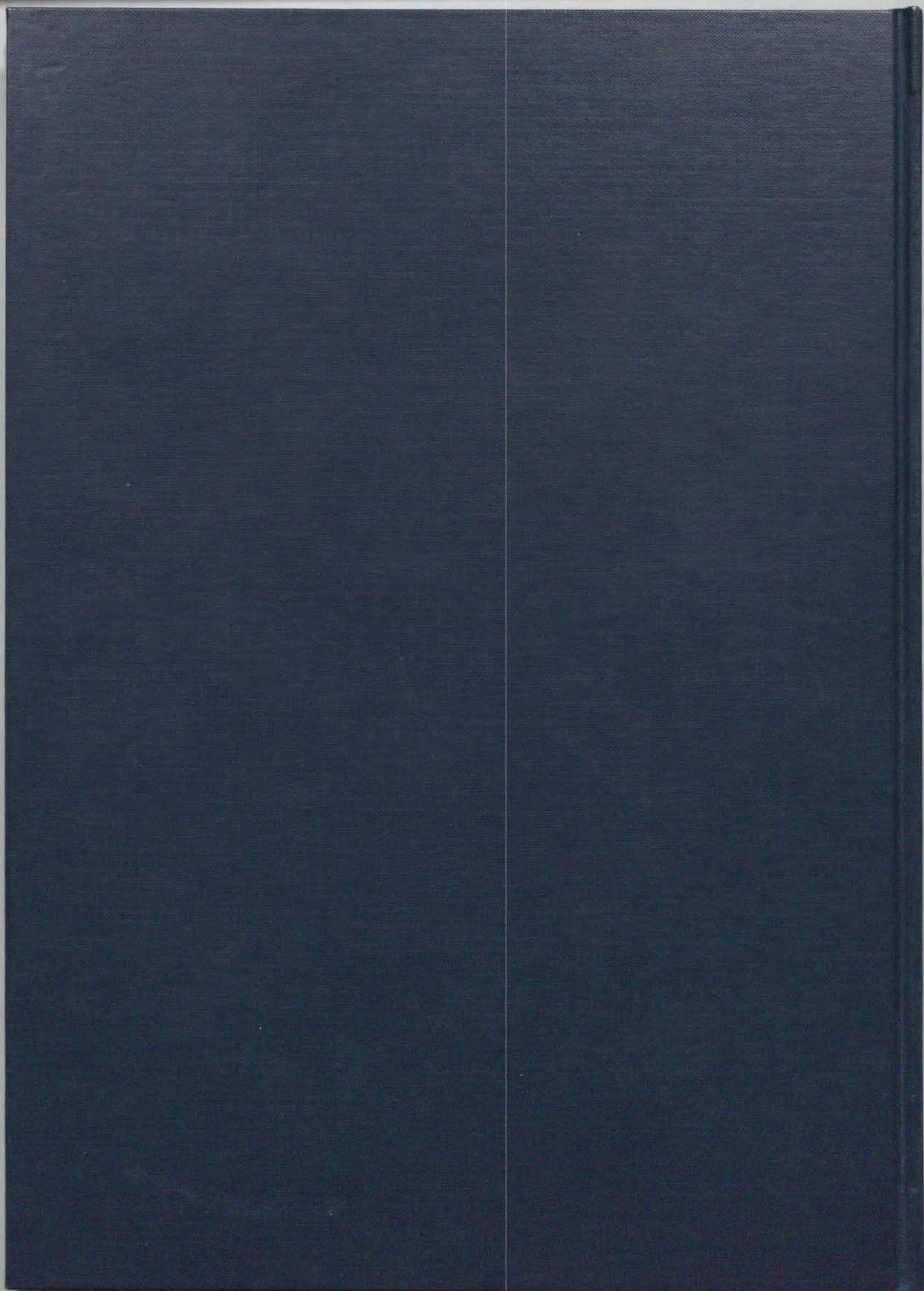


Fig. C.2



1 2 3 4 5 6 7 8
Inches
1 2 3 4 5 6 7 8
cm

Kodak Color Control Patches

© Kodak, 2007 TM: Kodak

Blue	Cyan	Green	Yellow	Red	Magenta	White	3/Color	Black

Kodak Gray Scale

C **Y** **M**

© Kodak, 2007 TM: Kodak

A 1 2 3 4 5 6 **M** 8 9 10 11 12 13 14 15 **B** 17 18 19

